KARAGANDA TECHNICAL UNIVERSITY NAME OF ABYLKAS SAGINOV
NON-COMMERCIAL JOINT-STOCK COMPANY

UDC 622.272:551 Manuscript Copyring

GYLYM SAPINOV KAIRATOVICH

A study on the real-time spatial localization of seismic events in underground mines

8D07202 – Mining engineering

Doctoral (PhD) dissertation

Scientific advisor
PhD A.Zh. Imashev

International Scientific advisor
PhD D. R. Makhmudov
(Tashkent, Uzbekistan)

The Republic of Kazakhstan
Karaganda
2025

Table of Contents

Abstract

This study examines the significant effects of anthropogenic seismic activity in underground mining on safety, productivity, and operational expenses. The precise identification of microseismic and rockburst source areas is essential for preventing unexpected occurrences like rockbursts. The existing constraints in forecasting the timing of these occurrences need an emphasis on likely locales. The study seeks to address this constraint by creating an approach that monitors and adjusts to alterations in ground conditions, offering a real-time solution for the selection of suitable velocity models in seismic monitoring systems. This approach aims to enhance the reliability of source location computations by accounting for the dynamic velocity model in underground mining environments, hence improving worker safety and mining productivity. The research acknowledges the changing properties of rock masses and voids during mining, emphasizing the insufficiency of a constant velocity model in source localization methods. This study utilized data produced from laboratory studies that simulated the continuously changing environment of underground mines. Analysis indicates that, because to the heterogeneity and ongoing fluctuations in the mining environment, seismic wave velocity cannot be regarded as a constant in source localization methods. Real-time prediction of seismic wave velocities markedly improves the precision of seismic event source localization. Dynamic numerical modeling in FLAC3D, utilizing laboratory data, was utilized to comprehend wave propagation and the underlying physics of the issue. Machine-learning techniques, such as Linear Regression models utilizing laboratory data and Deep Artificial Neural Networks for enhanced accuracy, were employed to forecast seismic wave velocities under diverse scenarios.

Acronyms and definitions

AE	Acoustic emission
ANN	Artificial neural networks
ASTM	American Society for Testing and Materials
CNN	Convolutional neural networks
DL	Deep learning
DT	Decision tree
FLAC	Fast Lagrangian Analysis of Continua
GAN	Generative adversarial networks
HDT	Hit definition time
HLT	Hit lockout time
MAE	Mean absolute error
ML	Machine learning
MS	Microseismicity
PDT	Peak definition time
ReLU	Rectified linear unit
RMR	Rock mass rating
RQD	Rock quality designation
SCA	Static cracking agent
UCS	Uniaxial compressive strength

1. INTRODUCTION

1.1. Background

Seismicity is the natural occurrence of earthquake activity or the produced vibrations of the earth resulting from anthropogenic activities. This study examines seismicity in underground mining resulting from anthropogenic activity. A seismic event is defined as the abrupt release of energy from the rock mass or crust, generating a series of seismic waves that propagate through the rock mass or crust. In mining, seismic activity that results in damage to an excavation, machinery, or personnel injury is termed a rockburst. Phenomena like rockburst and seismicity can significantly affect mine operations regarding safety, productivity, and operational expenses. Nonetheless, despite advancements in technology, forecasting the timing of rockbursts remains contentious and subject to debate within the mining sector and rock engineering. [3] assert that predicting the timing of rockbursts is challenging, and the sole approach to address this issue is to identify potential rockburst zones by numerical modeling and empirical knowledge. Recent technology advancements have rendered microseismic monitoring systems highly prevalent, particularly in the mining sector, especially for deep underground mining endeavors. The microseismic monitoring system facilitates the observation of mining-induced seismicity to assess probable seismic hazard sources. This tool is crucial for managing seismic risk regarding the exposure of infrastructure and personnel to its effects. The microseismic monitoring system is essential for comprehending the rockburst mechanism, as it can detect and identify mine seismic zones. The precision and forecasting of event source locations in the microseismic monitoring system are contingent upon the input velocity. Regularly updating input velocity models in seismic monitoring systems is time-consuming and may lead to inconsistent source locations during the intervals between updates.Contemporary technologies are unable to accurately determine the site or predict the timing of a rockburst. Given that underground mine seismicity greatly impacts workers safety and mine production, identifying potential solutions for precise seismic event source localization is essential for alleviating rockburst consequences.

The subterranean mining environment is difficult to regulate, whereas the laboratory provides an ideal controlled setting for simulating and examining seismicity. This study employs discrete physical modeling. Instead of depending on a single block that undergoes alterations to accommodate the fluctuating ground conditions in mining locations (a labor-intensive method), we employed individual blocks. Each block denoted a distinct phase in the mining process concerning time, structure, and geometry. This chapter outlines the imperative to enhance existing velocity models in seismic monitoring systems, delineates the research topic, articulates the study aims, underscores the significance of the findings for industry and science, and gives the thesis framework.

1.2. Problem definition

Recent research has revealed that wave velocities in rock masses during deep mining are variable, contrary to the common assumption in seismic monitoring systems' source location algorithms. Rock masses in mining areas are perpetually deteriorated due to mining activities. Stresses caused by blasting and excavation cause fracturing of the rock bulk. Water's presence expedites weathering and erosion processes. Consequently, the application of 3D velocity models utilizing 3D ray tracing in heterogeneous medium, which can account for voids resulting from mining operations, is currently under active investigation [72]. This method shown enhancements in the precision of seismic event source localization. Seismic wave velocity alterations result not only from the formation of voids but also from various other factors contributing to rock mass degradation, such as stress-induced fracturing and the dynamic characteristics of the voids, including their size, shape, and content (i.e., type of backfilling or absence thereof). In contemporary accounting practices for voids in seismic wave velocities, the velocities in seismic monitoring systems are frequently revised utilizing development bursts or weight drops. Due to the continuously changing conditions of the rock mass in mining, real-time velocity variations must be anticipated and incorporated into the seismic monitoring systems' source location calculation algorithm. The event sources situated in perpetually fluctuating ground conditions between velocity updates will lack reliability. Furthermore, while regular velocity upgrades may enhance the circumstances, their implementation is both arduous and expensive.

1.3. Research objectives

The main objective of the project is to develop novel techniques for monitoring variations in velocity resulting from the constant deterioration of ground conditions caused by mining operations in subterranean environments. The objective is to forecast the optimal velocity model in real-time for application in seismic source localization computations within seismic monitoring systems.

The specific research aims are to:

1) Simulate varying rock mass characteristics in mining sites utilizing rock samples with diverse parameters, including perforations, open voids, and fluctuations in backfill and fracture conditions.

2) Simulate the impacts of mining-induced fracturing by deliberately fracturing rock blocks with both filled and unfilled gaps to analyze the influence of fractures and rock mass quality on seismic wave velocity.

3) Comprehend the sensitivity of seismic wave velocity to diverse circumstances inside the subterranean mining context. Perform dynamic 3D numerical modeling using FLAC3D to simulate and assess velocity variations inside the rock mass under different situations.

4) Utilize machine learning (ML) to ascertain seismic wave velocity under diverse underground mining settings for the real-time identification of seismic event source sites.

1.4. Scope of the research

The research is aimed at investigating underground mining conditions in a controlled laboratory environment backed with numerical modelling to understand the effect of continuously changing mining environment on seismic wave velocity and its impact on the accuracy of seismic source locations. Since the rockburst is site-specific, it depends on the strength of the rock mass, in situ stress state, mining method, the shape of the opening, and geology. This fact complicates the creation of a general solution for the purpose of accurate estimation of rockburst source location. Therefore, the outcome of the study should be considered as a procedure for accurate seismic event source location in any type of underground mine. It can be achieved by correlating rock mass quality and velocity as in [4]. To understand a rather complex problem, dynamic numerical modelling of seismic events, together with laboratory tests, gave a strong basis for the development of the 3D velocity model to improve the accuracy of seismic source location. Input parameters for the modelling were provided through laboratory tests that mimicked the continuously changing mining environment. The study did not account confining stresses. This aspect is planned for future study.

1.5. Significance of the research

Rockbursts in deep underground mines necessitate significant attention and presently represent a major difficulty in rock engineering and mining science (Wagner 2019). Significant judgments regarding seismicity are determined through the observation of seismic activities.

The importance of the research findings to the mining sector and scientific community is as follows:

- Precise seismic source coordinates
- Substantial enhancement of mine safety
- Decrease in downtimes attributable to rockbursts o Augmented mine productivity
- Precise monitoring of cave propagation in block caving mining and accurate observation of fracture growth and propagation in hydraulic fracturing

Predicting stress changes based on rock mass response will enhance understanding in the field of rock research.

The precise identification of areas with elevated seismic risks is essential for efficient seismic monitoring systems. This would facilitate the prevention of fatalities and production delays by ensuring the safe evacuation of equipment and personnel prior to a rockburst and enabling secure re-entry following seismic events.

1.6. Approach

To accomplish the research objective, the subsequent tasks must be executed:

1. Simulating the mining environment in the laboratory

a. Replicate the varying conditions of the rock mass in the mining environment:

▪ Preparation of uniform cubic rock/concrete specimens from granite and concrete of varying dimensions and borehole diameters, symbolizing the progressive maturation of the mine over time, where larger sample sizes indicate greater mine development and larger hole diameters reflect an escalating extraction ratio over time.

▪ Infilling voids in rock/concrete specimens with various compositions: void, 0% cement (100% dry sand), 0% cement (water-saturated sand), 5% cement, 10% cement, 15% cement, and 20% cement cured for durations ranging from 8 hours to 28 days.

▪ The fragmentation of the blocks to record stress-induced damage resulting from mining.

- A static cracking agent is utilized in boreholes to fracture blocks, allowing for the observation of fracturing and backfill effects on seismic wave velocity.

- The cracks will be correlated with corresponding degrees of fracturing in the quality of rock blocks (rock mass quality).

b. Measurement of wave velocity in rock blocks under the various conditions outlined above utilizing the SAEU3H AE system. Wave velocities will be ascertained for each rock condition specified in item 1a above.

c. Identification of numerical modeling input parameters and validation of concrete block properties.

▪ Mechanical characteristics of granite and concrete blocks

▪ Temporal features of mechanical backfill (uncemented and cemented sand fill)

2. Utilization of 3D dynamic numerical modeling via FLAC3D to comprehend the physics of event source location issues and to corroborate laboratory testing outcomes.

3. Utilization of Machine Learning methodologies for real-time prediction of seismic wave velocity based on specific ground conditions, intended for integration into seismic monitoring system algorithms for source localization.

1.7. Thesis Outline

This dissertation is structured into seven chapters. This document first examines mining-induced seismicity, followed by a detailed exploration of each chapter's specific research objective as outlined below:

Chapter 1 – Introduction: This chapter offers context for the issue, emphasizes the importance of enhancing the precision of mining-induced rockburst prediction techniques, and outlines the significance, objectives, methodology, and scope of the research.

• Chapter 2 - Review of Literature:

This chapter examines the contemporary advancements in rockburst prediction and mitigation. This document addresses microseismic monitoring systems and its constraints, along with the influence of the input velocity model on the localization of seismic event sources.

Chapter 3 – Methodology: This chapter delineates the techniques utilized to fulfill the principal objective of precisely determining the seismic source location. These methodologies include laboratory experiments, numerical modeling, and machine learning.

Chapter 4 – Laboratory Experiments on Discrete Physical Models Simulating Mine Environments: This chapter delineates the laboratory configuration, encompassing the materials and apparatus employed to replicate continuous rock mass deterioration in subterranean mines, and presents the findings from laboratory tests utilizing Acoustic Emission (AE) technology. The document delineates the methodology for velocity computation, examines the effects of ongoing rock mass deterioration on seismic wave velocity, elucidates the Rock Mass Rating (RMR) calculation process, and specifies the ultimate database employed for numerical modeling and machine learning.

Chapter 5 – Dynamic Numerical Modeling: This chapter delineates the numerical modeling process, commencing with model building and concluding with the reporting of sensitivity and parametric analysis results.

• Chapter 6 - Machine Learning: This chapter delineates machine learning methodologies utilized for velocity forecasting and event source localization.

• Chapter 7 - Conclusions and Recommendations: This chapter encapsulates the findings and offers recommendations derived from the performed research.

2. LITERATURE REVIEW

2.1. Mining-induced Seismicity

As natural resource output escalates and reserves diminish, underground mines are being excavated to greater depths globally [23]. Additionally, geotechnical engineering projects, including tunnels and subterranean laboratories, are situated in profound formations characterized by complex geology and ground conditions [32, 86]. Elevated in situ stresses combined with intricate geology lead to several hazards, including rockbursts, rock mass caving, and excavation deformations [21, 60, 66, 88, 79]. Rockburst is characterized as a quick and strong seismic occurrence triggered by excavation that results in damage to the excavation[38]. Rockburst is categorized as one of the most perilous geological phenomena in underground mining due to its tremendous intensity and sudden occurrence. It inflicts harm on excavations, machinery, and personnel. Rockbursts can be classified into three categories according to their source mechanisms: strainburst, pillar burst, and fault-slip burst [8, 28]. The predominant kind of rockburst in subterranean mines is strainburst [8]. Strainburst occurs due to tangential stress from excavation, leading to violent and unstable rock failure [37, 8]. Pillar burst refers to the rapid failure of an isolated pillar or a segment thereof, occasionally leading to the fragmentation and ejection of rock debris from the pillar [27]. It transpires when the accumulated elastic strain energy reaches a critical threshold, at which point the released energy exceeds the wasted energy. A substantial quantity of failed rocks is expelled, and the magnitude typically exceeds that of a strainburst [38]. Most rockburst research concentrates on causes, risk assessment, prediction, prevention, and mitigation. Methodologies for studying rockbursts can be categorized into five types: empirical, analytical, experimental, data-driven, and numerical. [49, 11] assert that an effective method for controlling rockbursts has not yet been established, owing to their complexity and the myriad components involved, such as geological conditions, in situ stresses, induced stresses, and mining operations that serve as triggering conditions [24]. Nonetheless, the issue of rockburst can be addressed in two ways. Initially, by mitigating the damage inflicted by seismic activity, and subsequently by regulating the position, timing, and amplitude of the seismic event. In the event of many exhibits and significant seismic occurrences, backup mechanisms failed to avert damage to mines. If the risk of injury is significant and cannot be mitigated just by a support system, then it is necessary to monitor the location, timing, and severity of the event. The strategic approach to rockburst management involves monitoring the location, timing, and amplitude of rockbursts to mitigate their effects. Certain forms of rockbursts are attributed to mining sequence, excavation shape, or a combination of these elements with geological features. The strategic approach involves altering the mining sequence, stoping sequence, and, in some instances, the initial mine design[38]. Recently, a comprehensive strategy that incorporates tele-remote mining, improved ground support, advanced support systems, and reduced exposure for workers and equipment through seismic monitoring has proven to be more beneficial than the isolated implementation of any individual component [73].The likelihood of rockburst occurrence is assessed based on the seismic history of the specific mine and comparable mines. Mining-induced seismicity hazards are categorized into two types: rockburst danger and seismic hazard. The former denotes the likelihood of a seismic event causing harm, whereas the latter signifies the chance of the occurrence of a seismic event. Not all earthquake activity lead to damage. From a geomechanical standpoint, the primary seismic hazards can be categorized as follows:

1. Microseismic Density: Microseismic activity indicates rock mass deterioration that may result in ground collapse. Damage resulting from microseismic density is categorized as a permanent hazard due to its irreversible nature.

2. Seismically Active Faults: The existence and number of active faults indicate the hazard level. Seismically active zones correspond to a short- to medium-term risk.

Major seismic events can be induced by an active fault plane.

b. The presence of two or more active tectonic planes exacerbates the risk of ground hazards.

c. Local rockbursts are induced by gravitational forces and the release of seismic energy, posing possible risks to crew safety, mining excavations, and equipment.

3. Dynamic Stress Loading: significant seismic occurrences, such as rockbursts, cause substantial excavation damage by generating dynamic stress loading. The associated danger is categorized as a short-term hazard [48].

The analysis of rockburst case studies reveals that the adverse impacts of rockbursts are often localized and inconsistent. The extent of damage sustained in an excavation from a rockburst varies by location. The limited nature of rockburst damage arises from complex mechanisms associated with rockburst occurrences and the interplay of multiple contributing elements. Although various elements influencing rockburst damage have been identified, the specific conditions that initiate rockburst events in a complex subsurface ecosystem remain unclear [50, 11].

2.2. Rockburst managing methods

Researchers worldwide have invested significant efforts in understanding rockburst causes, prediction approaches, and preventative methods to mitigate seismic activity in mining operations [90]. An essential element in preventing and alleviating rockburst disasters is the establishment of precise monitoring and early warning systems.

Currently, monitoring and early warning techniques for rockbursts can be classified into two main categories: conventional rock mechanics methods (such as the drill cuttings method and coal-rock mass deformation measurement method) and geophysical methods (including microseismic monitoring, acoustic emission, and electromagnetic radiation monitoring methods) [65].

2.2.1. Microseismic monitoring systems

2.2.1.1. Predictive methods

Geophysical methods, especially the microseismic monitoring system, have become prevalent in deep mines due to their non-invasive characteristics, continuous data collection, and automated monitoring functions. The microseismic monitoring system has demonstrated efficacy in evaluating rockburst dangers by detecting vibration wave signals generated from roof failures or rock mass cracks. The microseismic monitoring system assists in assessing the displacement and fracture condition of the rock mass by monitoring and issuing alerts about potential rockburst threats. The system delineates areas of stress-induced fracture related to mining operations. The microseismic monitoring system is crucial for facilitating a rapid response to anomalous activities, including high-magnitude occurrences. Delivering a prompt and dependable identification of seismic occurrences is a fundamental responsibility of mine seismicity surveillance. The determination of the seismic event source location involves two steps: first, the computation of propagation time, and second, the inverse technique.

At mining sites, numerous derived indices, including energy level, occurrence frequency, primary frequency of vibration waves, and fractal dimension, are routinely employed to assess the current hazard condition. [87] examined the functional correlation between MS energy and rock damage by the application of traditional Benioff strain theory. Consequently, they introduced an innovative criterion for forecasting rockburst occurrences based on the timing of their manifestation. [45] utilized the wavelet packet transform technique to examine the complex waveforms of MS occurrences. Their studies revealed a downward shift phenomenon in the energy distribution of frequency bands, which may act as an early warning indicator for rockburst events. [84] emphasized the anomalous alterations in source parameters of MS tremors, including MS event density, seismic energy density, cumulative volume, energy index, and b-values, as significant indicators for detecting possible rockburst occurrences. [54] examined microseismic events that occurred prior to or during roof collapses and surface detonations, employing Fractal Dimension and b-value methodologies. Their findings demonstrated that these two characteristics aided in identifying precursor signatures for the spatial-temporal prediction of rockburst events. [82] introduced various statistical metrics, such as cumulative apparent volume, energy index, and cumulative released energy, and examined their correlation with rockburst occurrences. Their approach offered a significant reference for rockburst forecasting. [22] proposed a fractal computation technique to analyze the self-similarity of energy distribution in MS events during the initial stages of rockburst development. The daily energy fractal dimension of MS events was noted to rise as an immediate rockburst approached, providing a framework to limit the risk of such occurrences during the excavation of deep, hard-rock tunnels. Furthermore, the utilization of the MS system in rockburst monitoring has a lengthy history, leading to a significant collection of monitoring data over time. This data has established the foundation for the implementation of artificial intelligence (AI) algorithms in predicting rockburst hazards and their location. Recently, various researchers have effectively utilized decision trees, Bayesian networks, logistic regression, neural networks, and other methodologies to forecast rockburst occurrences, demonstrating practical applications in mining locations [83]. However, the aforementioned warning indications may produce varying results for the same event because of their unique principles in representing the development of rockburst precursors. This discrepancy may hinder the precise evaluation of hazard conditions by mining personnel. Furthermore, the forecasting of rockbursts exhibits a significant class imbalance problem, constraining the practical efficacy of machine learning techniques and frequently resulting in overfitting occurrences. Therefore, effectively preventing and controlling rockbursts in the field through the analysis of MS warning indications from a time series viewpoint is difficult.

2.2.1.2. Velocity model for microseismic monitoring systems

The capacity to observe a 3D volume utilizing a distribution of 3D sensors constitutes an optimal arrangement that will provide the most precise source location and parameters. Nonetheless, the distribution of 1D (linear) and 2D (planar) sensors can yield dependable data and may serve as a microseismic array. The installation of triaxial sensors is essential for linear or planar sensor distribution to prevent non-uniqueness.

The chosen velocity model for the rock mass is a critical determinant of the precision of seismic event localization. A singular velocity model is predicated on the premise that the entire volume possesses uniform elastic characteristics, rendering it isotropic and homogenous, with identifiable source locations such as blast holes or areas of significant impact. Nonetheless, the majority of mines continue to employ a singular velocity model for microseismic monitoring. Two-dimensional models employ many parallel layers that may exhibit anisotropy or be isotropic. The most organized velocity model is a three-dimensional model with six horizontal layers and the three-dimensional configuration of voids and caverns. The mining environment is complex due to geological formations, natural voids, and excavation operations. Consequently, the 3D velocity model serves as an effective method for integrating layers, voids, and blocks. The homogenous velocity model is unsuitable for seismic monitoring in mining environments because of the constantly changing conditions. A comprehensive 3D velocity model can be developed. The 3D velocity model can be constructed via ray-tracing or wave front reconstruction [72]. Nonetheless, ray tracing encounters constraints during execution, one of which being a significant rise in velocity within the medium. Consequently, ray tracing is applicable solely to a limited set of velocity models and is more effectively managed by numerical modeling. [72] introduced an enhanced Fast Marching Method (FMM) algorithm for wavefront reconstruction. The approach evaluates transit time and velocity, utilizing a 3D model constructed from existing geological and structural data; this method computes variable velocity models via wavefront reconstruction. The algorithm is tailored for low-velocity volumes, specifically caves or excavated stopes. The standard FMM offers both rapidity and precision for obtaining practical outcomes; nonetheless, the technique necessitates the simulation of the initial arriving wavefront.

The three-dimensional allocation of sensors is an ideal configuration that typically results in enhanced accuracy in determining source locations. Isolines change when traversing horizontal layers and cave zones, leading to reduced velocity. The analysis of the seismic mechanism is typically performed by moment tensor calculations without the aforementioned assumptions. An study devoid of assumptions establishes the foundation for identifying probable failures.

Seismic moment tensor inversion is the technique employed to utilize a three-dimensional velocity model. It necessitates the orientation of seismic energy towards the sensor and an adjustment of amplitude based on distance. The integration of the moment tensor inversion technique with a three-dimensional velocity model will yield more precise input data. Source mechanism analysis is conducted to enhance comprehension of the failure mechanics associated with the positioning of rock fractures.

2.2.2. Spatial-temporal prediction method

Recently, researchers have suggested rockburst warning approaches utilizing a "spatial-temporal integration" approach [11], [10] advocated for the application of active and passive seismic tomography to illustrate geological discontinuities in linear pictures, facilitating the evaluation of stress redistribution and the identification of high-seismicity areas for rockburst hazard assessment. [44] identified sharp-rise-sharp-drop fluctuations in total daily energy, event count, energy deviation (≥20), and event count deviation (≥1) as temporal antecedents for high-energy earthquakes. They devised a spatial-temporal integrated early warning technique for rockbursts by combining temporal indicators with the spatial evolution patterns of the high-energy density index of MS (EDIM), velocity, and velocity anomaly zones. [10] devised a spatial-temporal forecast approach for rockbursts by employing multidimensional data from MS monitoring and creating contour maps for each indicator. [75] utilized temporal and spatial distribution graphs of tremors, in conjunction with energy density cloud pictures, to pinpoint high-stress areas.

Notwithstanding significant advancements in rockburst early warning techniques, the majority of methods depend on qualitative descriptions, such as the continual increase of indicators or evaluations of whether indications surpass key thresholds. These systems rely on human assessment of indicator trends or are constrained by fluctuating critical values resulting from the intricate conditions of mining operations, impeding their widespread use. Moreover, anticipating rockbursts from a spatial viewpoint predominantly involves intricate modeling and computations, complicating the fulfillment of timely and precise warning requirements at mining sites.

Comprehensive laboratory studies and field observations have shown that rockbursts exhibit a nonlinear developmental trajectory [44]. The poor comprehension of the fundamental mechanics behind rockbursts complicates the identification of a singular measurement indicator that comprehensively represents the entire evolution process of rockbursts. Rockbursts, however, arise from stress-induced damage to coal-rock formations, marked by the internal initiation, propagation, convergence, and connection of fractures, finally resulting in the formation of massive fissures. The energy emitted during this process disseminates outward as vibrational waves, electromagnetic signals, and various other forms. Thus, metrics that measure the attributes of energy release signals across different dimensions (such as MS energy, frequency, etc.) likewise demonstrate variations. An exhaustive examination of these evolving patterns is essential for identifying aberrant trends before significant coal-rock damage occurs, acting as a pivotal element in rockburst warning systems. Moreover, the proper identification and quantification of spatial differences in warning indicators at specific locales are crucial for the effective prevention and control of rockbursts.

2.2.3. Support and Backfill

Enhanced support is a mechanism designed to mitigate damage resulting from seismic activity. In conjunction with the type of support system, it is crucial to choose the appropriate timing and place for support installation. Enhanced support is an integrated support system comprising cone bolts, mesh, shotcrete arches, or zero-gauge straps. The integration of these two support systems has proven effective in burst-prone environments and areas adjacent to seismically active geological formations. Enhanced assistance is more efficacious when implemented during the initial development phase, as postponement results in compounded difficulties over time due to elevated in-situ tensions [48]. The release of seismic energy is a dynamic and variable process. The majority of the mining area will remain unaffected; hence, the construction of support across all mining areas is not pertinent due to its exorbitant cost. A seismic hazard map serves as a strategic tool for identifying locations for the construction of increased support to ensure ground stability. Furthermore, it facilitates the further planning of mine growth by establishing infrastructure in safer locations or by implementing a more robust support system. Nevertheless, such support systems are expensive and cannot be implemented during the entire mine development [48]. Evaluating the potential for rockburst damage in a specific section of the mine is essential for predicting the time and positioning of the support system.

Backfill constitutes an alternative form of ground support, and various types of backfill significantly influence the rock mass's response to mining operations. Nonetheless, backfill is region-specific, and substituting the backfill system with an alternative is a costly and protracted endeavor. Backfilling may mitigate rockburst damage solely in instances of relatively thin, tabular orebodies; however, in vast and more widespread orebodies, the impact of backfilling is minimal. The primary cause is material porosity, as it is unfeasible to introduce backfill with sufficient density to counteract convergence in orebodies of substantial thickness [38]. The potential energy in the orebody walls arises from the convergence of walls following mining operations. The energy source responsible for rockbursts is the potential energy within the walls. A portion of the energy released as seismicity is classified as a rockburst or seismic activity if it results in damage. Backfill can be utilized to diminish the discharged energy by absorbing a portion of the potential energy within the orebody walls. The intensity of the rockburst will diminish due to the altered energy equilibrium. A portion of the energy released during mining activities is retained in the pillars and walls, another portion is absorbed by backfill, and the remainder is discharged. The emitted energy is utilized in the fracturing of rock mass as seismic energy. Multiple factors regulate the energy of the wall rocks and the energy released. The primary elements are depth, stress level, stope span, and wall rock modulus. The energy quantity is related to the square of the depth (stress). It indicates that as load escalates, the stiffness of the wall rock must be augmented, and the stope span must be reduced [38].

2.3. Simplex Method

The simplex technique, first introduced by [58] as an optimization tool for minimizing functions, has achieved broad adoption in numerous scientific and technical fields. [53] enhance the discussion on optimization techniques, highlighting the effectiveness and versatility of the simplex method. Its capability in addressing complex, non-linear issues makes it a viable option for applications like seismic event source localization.

The computing efficiency of the simplex method is crucial in the real-time analysis of seismic event source location. [2] broaden the discussion to the utilization of optimization techniques, such as the simplex method, in addressing inverse problems in seismic monitoring. The intrinsic difficulties of these inverse problems, arising from uncertainty in velocity forecasts and sensor data, highlight the need for effective optimization methods. [70] presents a stochastic search and optimization framework to tackle the issues associated with uncertainty in seismic monitoring. This stochastic method improves the applicability of the simplex technique, especially in situations characterized by uncertainty in velocity forecasts and sensor data.

[71] explore the many uses of optimization techniques, including the simplex approach, within control theory. This literature, although not primarily focused on seismic monitoring, offers valuable insights into possible synergies with the subject, offering a comprehensive viewpoint on optimization applications.

In conclusion, the simplex technique proves to be a powerful and adaptable optimization instrument in the localization of seismic event sources. Its adaptability to diverse geological circumstances, capacity to manage uncertainties, and computational efficiency render it a valuable asset in the advancement of seismic monitoring systems. Continued research efforts are essential for enhancing and broadening the application of the simplex approach, tackling complex difficulties.

2.4. Numerical Modelling

Numerical modeling is a mathematical representation of a physical or other behavior founded on relevant hypotheses and simplifying assumptions [69]. According to [34, 35] , numerical modeling techniques in rock mechanics can be categorized into continuum, discontinuum, and hybrid methods.

Over the past 50 years, substantial breakthroughs have been achieved in numerical modeling to replicate physical processes in rock mechanics and rock engineering at several scales, owing to the swift progress in computer technology and software. The numerical modeling method offers advantages such as cost-effectiveness, safety, time efficiency, and flexibility in comparison to alternative approaches like physical simulation and field testing. It may additionally provide further information.

[67] assert that numerical modeling may be beneficial for many facets of the rockburst issue, encompassing the correlation between mining operations and the resultant seismicity, the source mechanism, and the effects of seismic waves on mining excavations. Numerical simulation techniques have been extensively employed to investigate the reasons of rock mass failure and the mechanical behavior of intricate rock masses. The simulation results, including seismic locations, magnitudes, and mechanisms derived from the numerical model, when compared with field seismic data, enhance confidence that the FDM/DEM coupled model operates realistically, despite being a considerable simplification of reality. The precise forecasting of rockburst occurrence is highly intricate due to the stochastic nature and intricacy of the rockburst mechanism [64, 90]. The incidence of rockbursts is predominantly influenced by alterations in ground tension resulting from excavation activities. Technologies for geological surveys, ground stress detection, rock mechanics theories and methodologies, along with advancements in long-term numerical simulations, have facilitated both qualitative and quantitative predictions regarding the location and strength of rockbursts [64]. Researchers assert that the era of quantitative rockburst prediction has commenced, necessitating a synthesis of numerical simulation and field observation [9].

Numerical modeling is the most effective method for assessing the reaction of rock masses to various mining systems and sequences. Furthermore, challenges associated with the sequencing and mining systems are highly intricate and difficult to modify. Numerical modeling is the appropriate method for evaluating mining tactics to mitigate the rate of energy release from the system.

Numerical models can quantify stress-strain variations induced by extensive mining activities in the absence of geotechnical monitoring [76]. Developed numerical models may indicate optimal access locations and appropriate stope sequencing. The process by which rock mass responds to mining, resulting in seismic energy release and potential damage to excavations, is intricate and not yet fully comprehended. Consequently, laboratory tests conducted in a controlled setting are a suitable approach for the research of seismicity.

The factors governing seismic activity in the mine differ from those influencing the extent of damage resulting from seismicity. Elevated stress is not the sole determinant of seismicity; hence, not all regions under significant stress induce rockbursts. A significant association exists between locations experiencing a substantial decrease in stored energy and seismically active areas. An analysis comprising three components is required to evaluate the potential energy release associated with mining operations. The principal elements of the analysis include: - Stress analysis - Energy analysis - Loading system analysis.

Multiple criteria must be fulfilled for the seismic energy release from the rock mass:

a) Applied stresses must exceed the strength of the rock mass.

b) A significant volume of energy must be stored and subsequently released.

c) Energy release must occur within a brief timeframe to trigger the dynamic, non-linear reaction of the rock mass.

Consequently, simulating mining operations using a tripartite analysis is essential for evaluating potential damage induced by seismic activity [38].

2.5. Summary

Rockburst incidents substantially affect personnel safety and mining productivity. Preventing such situations is seen preferable to addressing their repercussions. Recent studies demonstrate that microseismic monitoring devices are essential in deep underground mines, facilitating the characterization of mining-induced seismicity for a thorough assessment of seismic hazards. These monitoring systems are essential for reducing personnel and equipment exposure to potential seismic hazards, therefore alleviating seismic risks.

The efficacy of seismic monitoring systems significantly depends on their capacity to detect, locate, and measure mine seismic occurrences, hence enhancing the comprehension of rockbursting mechanisms. This comprehension is crucial for managing and alleviating seismic threats, leading to increased worker safety and higher mining output. The precision of these systems in consistently identifying event sources is intricately connected to the input velocity utilized in the event source computation method.

Employing a singular static input velocity or presuming a stratified model with a uniform rock mass in an underground mining context is impractical and frequently leads to considerable source localization inaccuracies. Underground mining activities result in ongoing alterations in rock mass characteristics and void conditions. Mining-induced stress changes can lead to rock mass fracturing, compromising its quality and triggering fault movements. Additionally, voids generated during ore extraction may be backfilled with materials of diverse sorts and strengths, while certain spaces remain unfilled. Thus, the conditions associated with underground excavations and the status of the formed voids are in a constant state of flux throughout mining activities. Therefore, employing a singular static input velocity or a stratified model with a uniform rock mass in seismic monitoring systems for source localization computations is unsuitable.

Upon examining the literature, it is clear that a major source of uncertainty impacting source location precision is the velocity model employed in the localization method. Developing a dependable velocity model in mining is difficult due to the presence of many rock types and the continual fluctuations in rock mass conditions caused by void formation and stress variations. This complexity requires a dynamically evolving velocity model, which differs from the prevailing assumptions of employing single (homogeneous rock mass assumption) or variable static constant velocity models (layered rocks assumption) in seismic monitoring systems for seismic source localization computations.

3. METHODOLOGY

To fulfill the thesis objectives, three primary tasks must be accomplished. The initial aspect pertains to the utilization of discrete physical models within a laboratory setting to simulate rock mass deterioration in subterranean mining. The laboratory provides a controlled setting to analyze fluctuations in seismic wave velocity due to ground condition deterioration. Executing experiments in regulated settings enables researchers to modify critical factors, meticulously analyzing their impacts both alone and collectively on the results. Homogeneous cubic samples of granite and concrete, varying in size and hole diameter, signify the progressive maturity of a mine. An rise in sample size indicates a larger mine, while a larger hole diameter reflects an enhanced extraction ratio with time. The spaces were filled with diverse materials (varied proportions of sand, cement, and water) reflecting distinct backfill types at different curing phases. The rock blocks were broken with a static cracking chemical to replicate mining-induced stress fracturing. Following the simulation of rock mass deterioration in subterranean mining, the wave velocity was assessed using rock blocks under the aforementioned conditions utilizing the Acoustic Emission (AE) technology. The experimental data was subsequently compiled into a database for future activities.

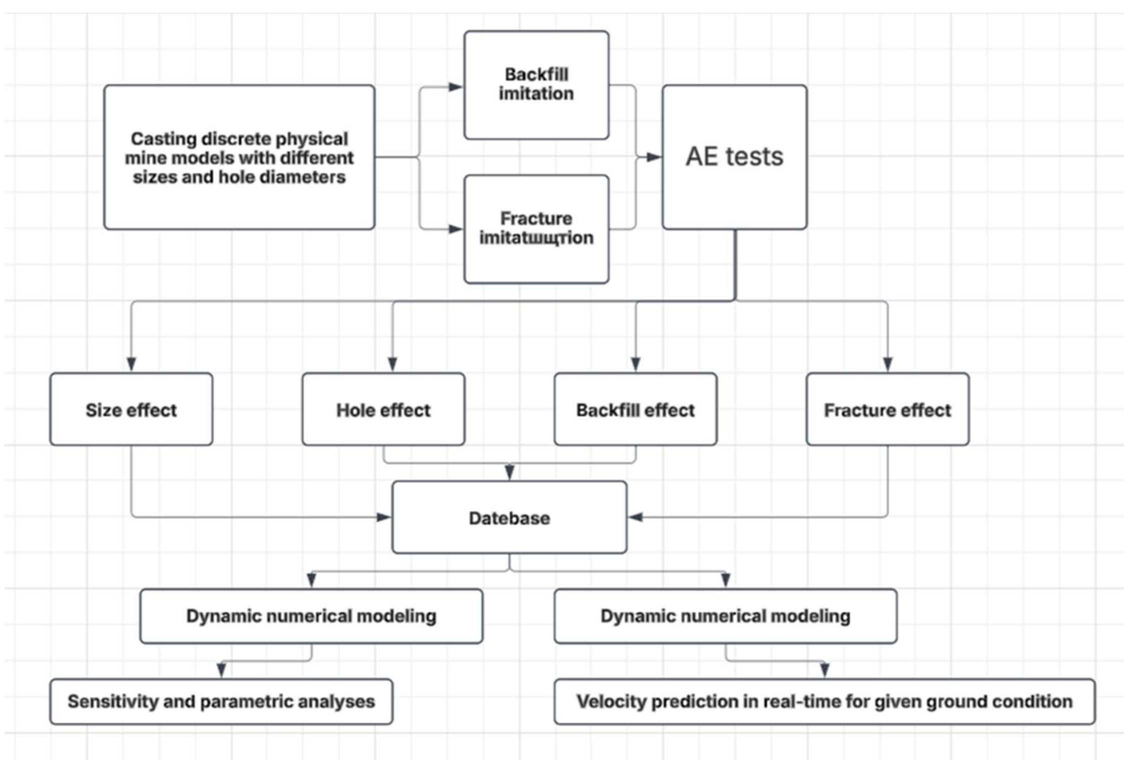

Figure 1. Schematic representation of methodology

The second task involves employing numerical modeling to analyze the sensitivity of seismic wave velocity to different parameters in the underground mining environment, as seismic wave velocity is closely related to the physical qualities of rock. Dynamic numerical modeling was performed using FLAC3D for this purpose. The selection of the program was determined by the nature of the material being modeled and the spatial dimensions of the issue. FLAC3D, employing continuum mechanics, is appropriate for materials seen as continuous solids, whereas UDEC and 3DEC, grounded on the discrete element approach, are optimal for distinctly separated or cracked materials. The research examines the impact of voids and the elastic properties of rock on the velocity of seismic waves in rock samples under transitory settings. Laboratory experiment findings involving granite and concrete cubes are simulated by dynamic numerical modeling in FLAC3D to accomplish this.

The primary objective of this job is to conduct sensitivity and parametric assessments through a numerical simulation of granite and concrete cubes, focusing on their dynamic behavior. The data utilized for the simulation originates from experiments concerning AE outlined in the initial task. Comprehending the influence of many aspects on this analysis is essential, particularly concerning the velocity of wave propagation through rock and the transmission of seismic waves. This comprehensive analysis is crucial, as a precise comprehension of wave speed might enhance the reliability of rockburst incidence predictions.

The third objective entails employing machine learning to forecast seismic wave velocity under diverse underground mine settings in real-time, intended as input for the seismic monitoring system's algorithm for source localization. This methodology is an innovative, three-faceted strategy that employs machine learning approaches for velocity forecasting and seismic event source localization, utilizing the simplex method. The database created with AE equipment was utilized to train the models. The initial phase emphasizes forecasting the velocity of seismic waves under diverse conditions utilizing machine learning algorithms, such as Linear Regression, Artificial Neural Networks (ANN), and Decision Trees (including ensemble techniques like Random Forest and Gradient Boosted Trees), to determine the most effective model. The second phase entails utilizing the simplex method for the initial identification of seismic event sources. The simplex technique optimizes an objective function that represents the travel time of seismic waves, which is contingent upon the anticipated velocities and likely locations of seismic events. To rectify the inaccuracies identified in the second phase, both the original and an enhanced dataset were utilized to train a machine learning model for the direct prediction of seismic event locations. This phase seeks to provide a more precise and refined prediction of seismic event sites.

In conclusion, the extensive methodology incorporates acoustic emission testing under regulated laboratory circumstances, dynamic numerical modeling using FLAC3D, and the implementation of machine learning. This comprehensive approach underpins succeeding chapters, augmenting the study's robustness and enabling further analysis and inquiry.

4. LABORATORY EXPERIMENTS ON DISCRETE PHYSICAL MODELS MIMICKING MINE ENVIRONMENT

4.1. Materials and methods

Laboratory tests simulating underground mining conditions are undertaken to comprehend alterations in seismic wave velocity inside continuously deteriorating rock mass settings. Concrete and granite blocks were utilized to replicate different stages and circumstances in subterranean mining. The utilized blocks were cubic in shape. The selection of sample material was predicated on material uniformity. The cube dimensions ranged from 150 mm to 450 mm (Figure 2), taking into account the influence of boundary conditions according to the theory of elasticity. Each cube was designed with and without a hole to illustrate the progressive increase in mine extraction over time. The concrete cubes were fabricated in compliance with the ASTM C-109 standard. The cubes underwent testing following a 28-day curing period, at which point they would achieve 99% of their strength. The apertures were located at the center of the cubes and extended through the blocks. The diameters of the holes ranged from 50 mm in the 150 mm cube to 150 mm in the 450 mm cube, increasing in increments of 25 mm, while the cube dimensions expanded by 75 mm from the 150 mm cube to the 450 mm cube (Table 1), illustrating a mine with a progressively increasing extraction ratio over time.

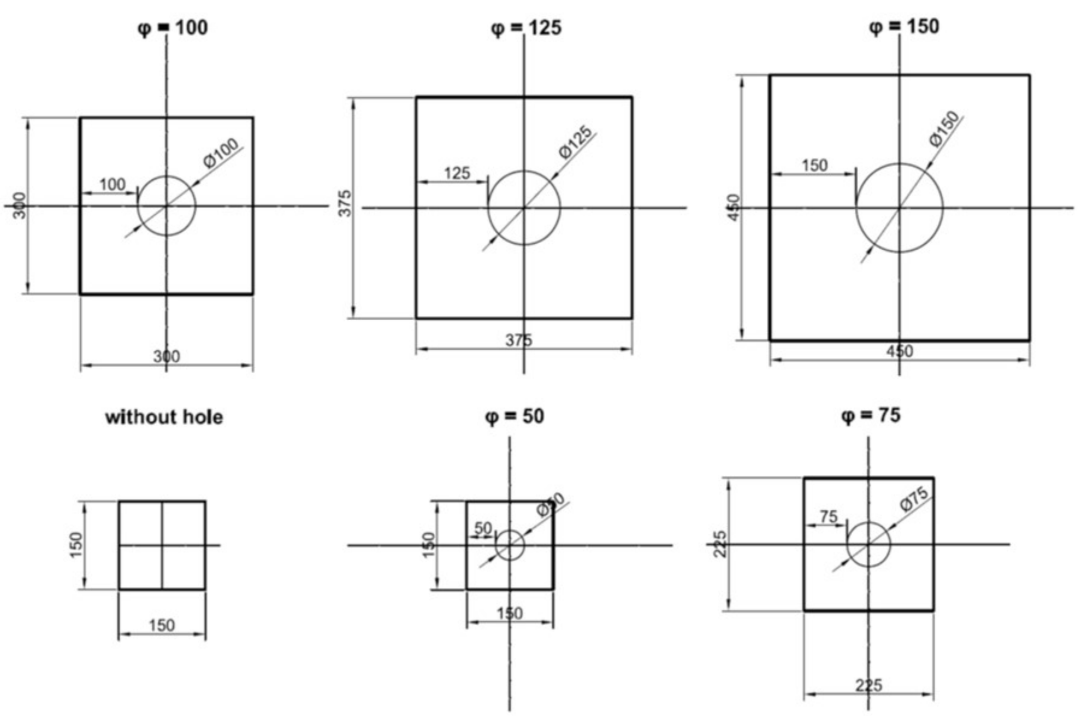

Figure 2. Sample sizes

Table 1.

Geometry of rock samples

Cube size (mm)	Material type	Hole diameter (mm)
150	concrete	0 (No hole)
150	concrete	50
225	concrete	0 (No. hole)
225	concrete	75
300	granite	0 (No hole)
300	granite	100
375	concrete	0 (No. hole)
375	concrete	125
450	concrete	0 (No. hole)
450	concrete	150

The replicated mining cavities within the cubes were filled with diverse combinations of sand, cement, and water at varying proportions to simulate different backfilling processes at distinct extraction stages and intervals. A backfill ratio of 0% cement (100% dry sand), 0% cement (water-saturated sand), 5% cement, 10% cement, 15% cement, and 20% cement contents was employed. Each kind of backfill was evaluated at many curing intervals (8 hours, 1 day, 7 days, 14 days, and 28 days) to assess the influence of the backfill cement ratio and duration on seismic wave velocity.

Induced stress and blasting effects were modeled using a static cracking agent (SCA), a highly expansive powdered cementitious substance for the fragmentation of rock and concrete [81]. The level of damage in the rock and concrete cubes was assessed using a modified Rock Mass Rating (RMR) system [5], adapted for laboratory-scale application. Fractures in the rock and concrete cubes simulate joints found in actual mines. Acoustic emission studies were performed to ascertain wave velocity through each investigated cube condition, encompassing backfilling and fracture stages. Eight sensors were strategically positioned on the cubes, with one functioning as a pulser to generate the wave across the hole, while the remaining seven served as receivers. The data obtained from the AE tests encompassed the wave arrival time at each sensor. Sensor 1 (pulser) was positioned at the center of the front view of the cube to facilitate the passage of the generated wave through the aperture in the middle of the block (Figure 3).

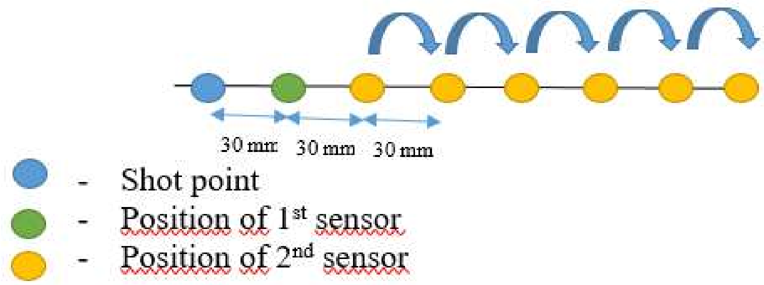

Fig. 6. general scheme of equipment testing methodology

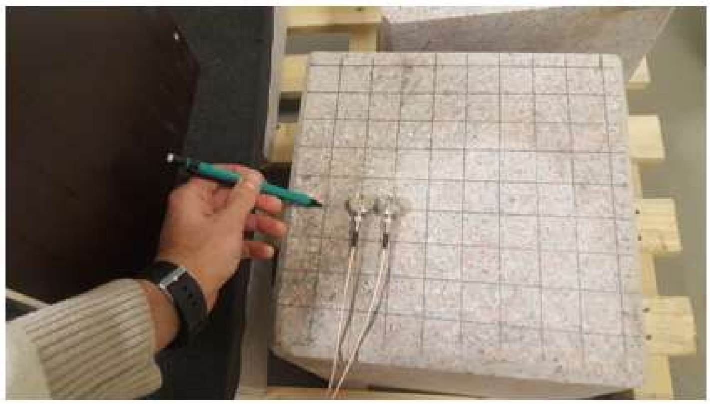

Figure 3. AE sensors attached to the rock sample

In mining operations, voids like stopes are typically filled with various types of backfill. To replicate backfilling, the voids in the blocks were later filled with backfill (Figure 4) utilizing varying cement to sand ratios of 0%, 5%, 10%, 15%, and 20%. The backfill with 0% cement concentration was evaluated in both dry and wet conditions. Each backfill type was cured for 8 hours, 1 day, 7 days, 14 days, and 28 days, and subsequently evaluated to evaluate the effect of curing duration on seismic wave velocity.

Figure 4. Granite rock samples with the cube size 300 mm with and without holes (hole diameter is 100 mm)

Initially, samples containing voids were evaluated devoid of any backfill to simulate a mine without backfill material. The subsequent tests involved filling the holes with various cement-to-sand ratio backfills, which were cured for durations of 8 hours, 1 day, 7 days, 14 days, and 28 days, to simulate a mine with diverse backfill kinds and ages.

4.1.1. Granite cubes

The research employed laboratory trials utilizing homogenous granite rock samples. The uniformity of the sample was the decisive element in selecting the rock type. The cube surfaces must be polished to a tolerance of 1 mm, ensuring that each pair of opposite faces is parallel. The uniformity and isotropy of the granite facilitated comparable outcomes. Preparing granite cubes in-house to match these criteria proved to be a difficulty. Consequently, a competent stone supplier was employed.

The project was ideally meant to utilize solely granite cubes. Nevertheless, the expense of granite cubes and the difficulty in acquiring samples with uniform composition led to the utilization of synthetic rock in the form of concrete cubes.

4.1.2. Concrete cubes

The concrete cubes were fabricated in the laboratory using a blend of sand and cement to simulate rock. Sieve analysis was conducted utilizing the vibrating sieve shaker AS 200 basic to exclude clay particles, organic matter, and oversized fragments from the sand. Particles above 4mm were eliminated as oversized fragments, whereas particles smaller than 0.002mm were discarded as clay. A proper cement to sand ratio was determined in accordance with ASTM C-109 C standard [7]. The cubes were utilized following a 28-day curing period. The material proportions for standard mortars, as per ASTM C-109 C standard, were utilized as follows: a sand to cement ratio of 2.75 and a water to cement ratio of 0.485.

Upon filling the mold with the mixture, it was vibrated for four minutes to ensure compaction and the expulsion of surplus air. Samples with a diameter of 37mm and a height of 74mm were prepared from the identical mixture for the UCS test as a control measure to guarantee uniformity in strength across all blocks.

4.1.3. Backfill Characteristics and Curing

Core samples containing 5%, 10%, 15%, and 20% cement were cast in wooden molds (Figure 5 a,b). The creation of the cement, sand, and water mixture involved two stages: the amalgamation of dry components (cement and sand) and the incorporation of wet components (the mixture of cement, sand, and water). Each process was executed for a duration of 3 minutes. The ASTM standard recommends a length-to-diameter ratio of 2 to 2.5 for core specimens used in UCS tests. The prepared backfill core samples possess diameters of 37 mm and heights of 80 mm. All backfill samples were polished and assessed for the smoothness of the terminal surfaces using an absolute digimatic indicator, as depicted in Figure 5 c and d. According to the ASTM standard, the surface variation of the sample has not surpassed 1 mm.

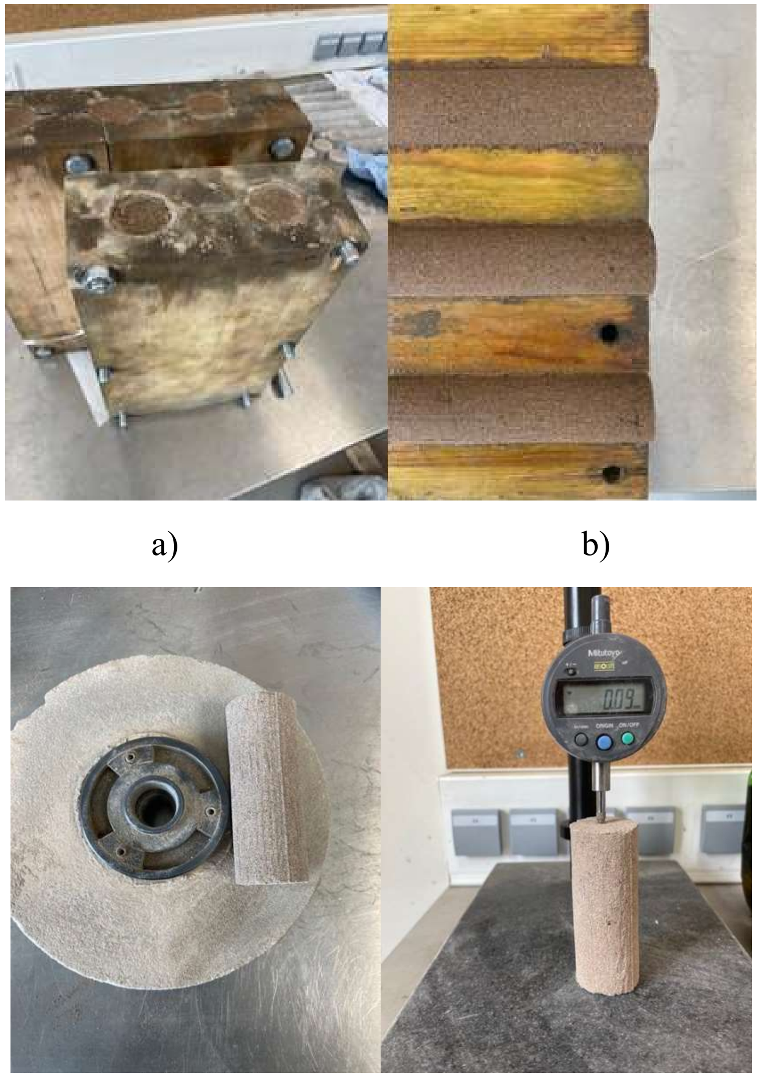

a) b)

c) d)

Figure 5. Preparation of core samples for UCS testing at various ages: molding (a); core samples (b); polishing (c); smoothness check (d).

The backfill strength was assessed by UCS tests. The UCS tests were conducted at curing ages of 1 day, 7 days, 14 days, and 28 days. UCS tests on core samples cured for 8 hours were disregarded due to the samples being excessively weak and moist for the testing protocol. Five tests were performed at each sample age for every backfill type; Figure 6 illustrates the average value of each UCS test.

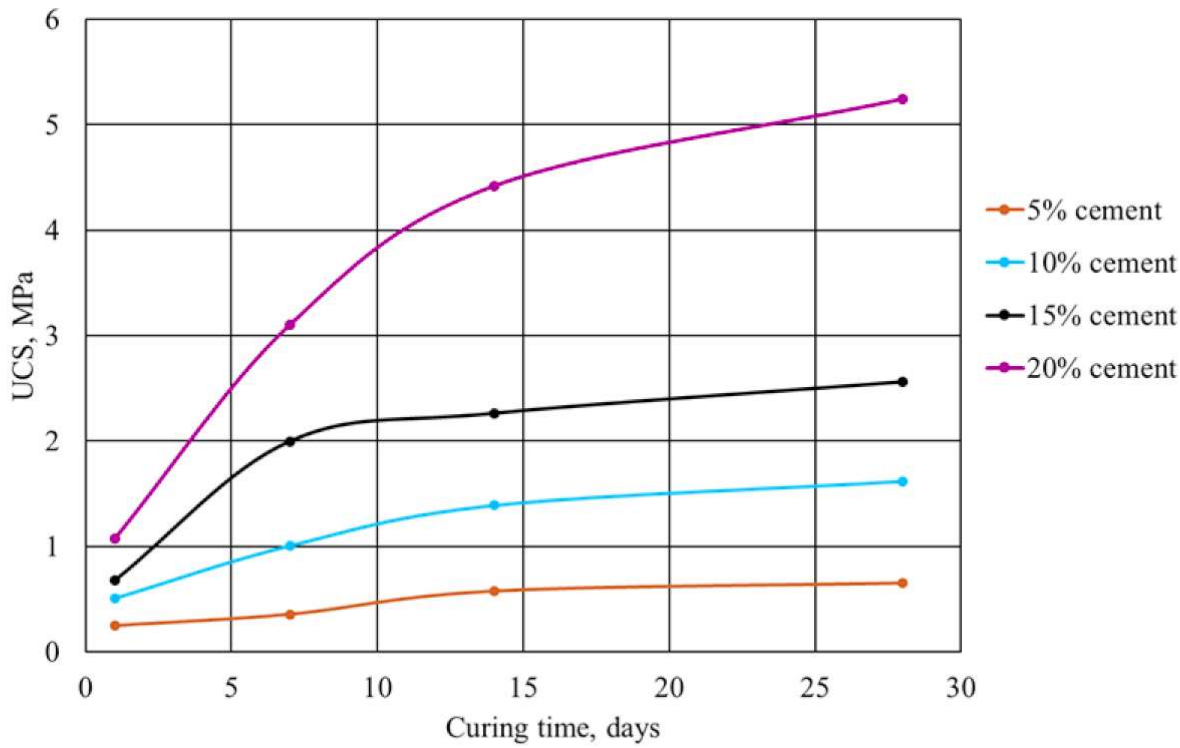

Figure 6. Backfill strength and curing time relationship.

The uniaxial compressive strength elevates with extended curing duration and increased cement content. UCS tests on core samples of backfill with cement contents of 5%, 10%, 15%, and 20%, cured for 28 days, exhibited greater magnitudes than those cured for 1 day with same cement contents. The strength increased by 2.65 times for samples containing 5% cement, 3.1 times for those with 10% cement, 3.75 times for samples with 15% cement, and 4.9 times for those with 20% cement.

4.1.4. Fracturing of cubes to mimic blast and stress induced fractures in underground mining

A static cracking agent (SCA) was employed to create fractures in the cubes as an alternative to blasting. SCA is an extensive powdered cementitious substance utilized for the fragmentation of rocks and concrete [81]. The SCA makeup is presented in Table 2. Upon combining with water and being poured into a cavity, the SCA expands, exerting pressure on the walls of the cavity to fracture the rock or concrete. SCA is ecologically sustainable and secure, as it does not emit any noxious vapors or detrimental materials. Furthermore, there is an absence of noise and airborne debris during the expansion and demolition of the fractured materials.

The SCA powder was combined with clean water at a ratio of 20% SCA to water. The liquid was poured into the block's holes within 5 minutes of preparation at a room temperature of 25 ℃ and a water temperature of 20 ℃. Fracturing of the blocks transpired after 2-3 hours of filling (Figure 7).

Table 2.
Chemical Characterization of SCA [40]

SiO2	MgO	Fe2O3	CaO	AI2O3
5.10%	2.20%	1.40%	87.10%	2.40%

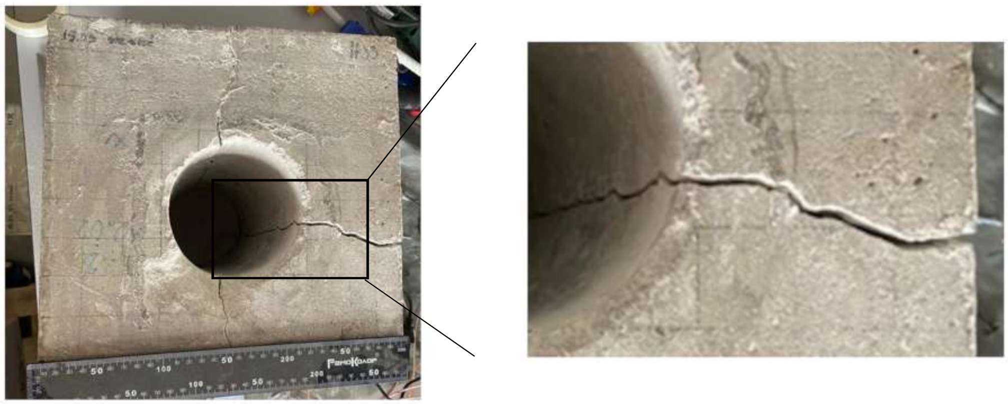

Figure 1. Fractured cube with 3 joints

4.2. Acoustic Emission Testing

4.2.1. Equipment

Acoustic Emission Testing (AET) is a method employed for the non-destructive evaluation of materials. AET can monitor alterations in material properties. This approach enables observation of crack propagation occurring within the interior of a material. Various terminologies are employed to characterize instabilities or "events" resulting from rock fracturing at distinct scales, as seen in Figure 8.

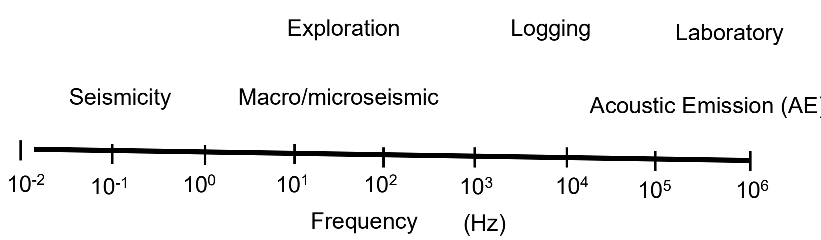

Figure 8. Monitoring frequency ranges of earthquakes, macro/microseismic activity, acoustic emission, and associated fields of study/domains of research [13]

[13] observes that in mine seismology, significant occurrences within the seismic spectrum are frequently referred to as mine tremors or mine-induced seismic events. Minor events typically situated near active mine stopes are commonly referred to as "microseismic events" because of their significantly lower magnitudes. At the lower end of the magnitude range, "acoustic emission" typically refers to high-frequency emissions or "rock noise" detected in rock samples subjected to loading in a laboratory or noticed in localized failure zones within a mine. The delineation between these

categories is ambiguous, and some writers, including [20], using the term "acoustic emission microseismic" or "AE/MS" to broadly encompass the latter two categories. Consequently, microseismicity occurring during the failure phase of a material under load closely resembles acoustic emission (AE). Acoustic emissions are defined as the energy discharged from stressed materials. The discharge of localized strain energy may result from fracture and can be detected on the material's surface by sensors. Consequently, AET is juxtaposed with seismological procedures due to their analogous principles yet distinct scales.

AET has been employed to monitor rock mass flaws in the initial phase before total failure occurs. The primary distinction from other non-destructive testing is in the nature of the data obtained and the method of application. In the ultrasonic approach, artificially generated signals and source-receiver configurations are employed to ascertain the geometric configuration of a defect within a sample. Conversely, AET can identify elastic waves traversing cracks within a sample [26]. In comparison to alternative non-destructive techniques, AET necessitates just a limited number of sensors under specific conditions capable of transmitting signals that exceed a trigger level threshold. AET does not require access to all sides of the sample, unlike all other through-transmission methods [26].

Figure 9 depicts a conventional acoustic emission detection system. AE sensors convert dynamic movements into electrical signals and identify AE waves at the surface of a substance. A preamplifier and main amplifier are employed to amplify weak AE signals, potentially offering a gain exceeding 1000 times. Elastic waves produced by the source disseminate across the material and are monitored by acoustic emission sensors [26].

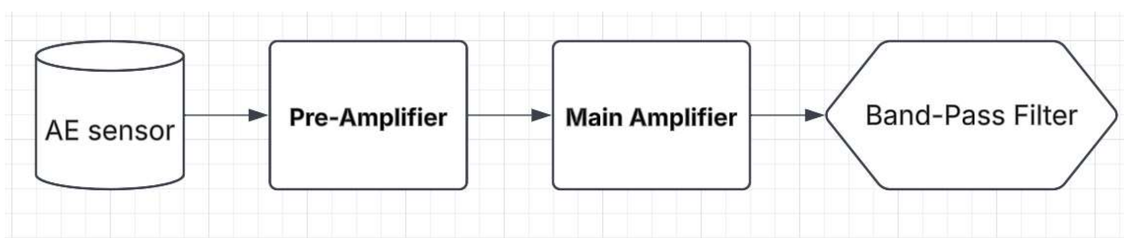

Figure 9. AE detection system [26]

The AE approach has been employed to investigate mine seismicity [19] and Kennet et al. (2000). Figure 9 illustrates the AE system and its attachments. This study utilized the SAEU3H AE system. The SAEU3H AE system is a multi-channel apparatus comprising AE data acquisition modules, a chassis with front and rear panels, an optional network communication module, a laptop, eight sensors, preamplifiers, and cables (Figure 10).

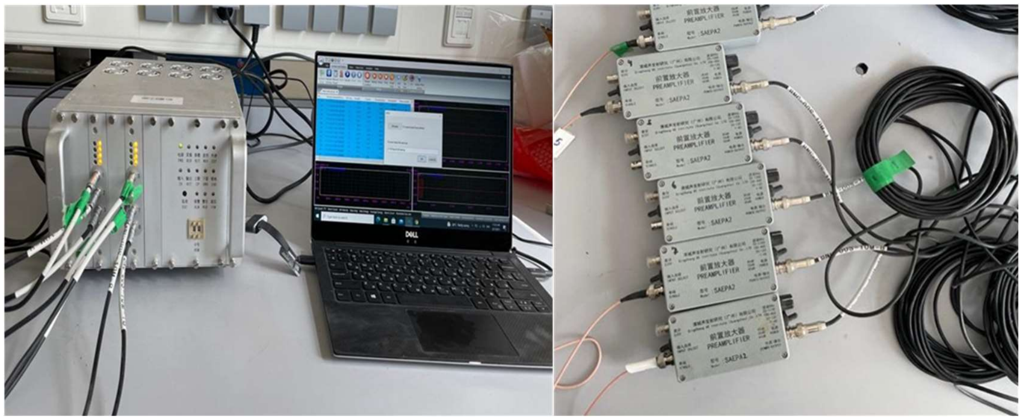

(a) AE data acquisition modules, chassis with front and rear panels, optional network communication module, laptop

(b) Preamplifiers and cables

Figure 2. AE system and accessories

In the laboratory experiments of this study, AE sensors were affixed to the surfaces of the cubes with hot glue, as seen in Figure 11. Each cube was equipped with eight sensors, one of which functioned as a generator to generate a pulse, while the remaining seven acted as receivers to detect the pulse wave. The wave was produced as a pulse from sensor number 1, positioned centrally in the front view of the cube, to facilitate the propagation of waves through the aperture.

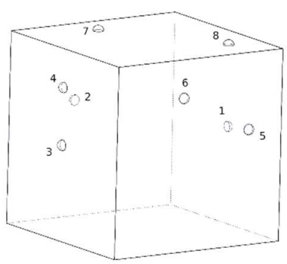

(a) 150 mm cube

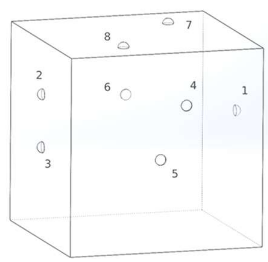

(b) 225 mm cube

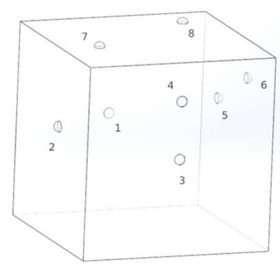

(c) 300 mm cube

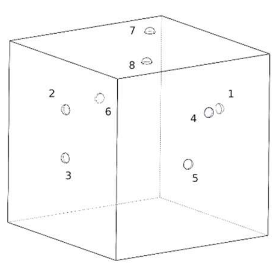

(d) 375 mm cube

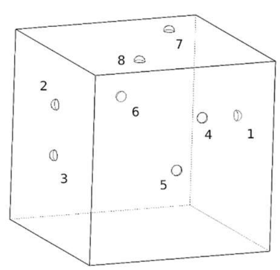

(e) 450 mm cube

Figure 11. Sensor positions on the various cube sizes without hole

The SR150M High-frequency broadband AE sensor is the type of sensor utilized in the studies with cube sizes of 150 mm, 225 mm, and 300 mm. The sensor operates within a frequency range of 60-400 kHz, with a peak sensitivity exceeding 75 dB. The SRI150 sensor type was utilized for larger cubes measuring 375 mm and 450 mm. The sensor incorporates a preamplifier with a frequency range of 60 kHz to 400 kHz and a sensitivity of 40 dB. The alteration in sensor type was required since the SR150M sensors were unable to detect wave arrival times at the receiving sensors due to seismic wave attenuation in inelastic materials like rocks and concrete utilized in the investigation. Seismic waves diminish with time and distance in inelastic materials due to multiple inelastic energy dissipation mechanisms, including porosity, fractures, and tiny motions along mineral dislocations or shear heating at grain boundaries [1]. Seismic wave attenuation ($\in$) is frequently measured by the quality factor (Q) (Equation 1) as noted by Ammon in [1].

$$\in = \frac{\gamma}{m\omega_o} = \frac{1}{2Q} \tag{1}$$

Where ɣ=coefficient of friction, m=mass and ωo=resonant frequency

A low attenuation (high quality factor Q) may signify a densely consolidated rock mass, capable of transmitting a displacement pulse with minimal energy dissipation, thereby arriving at the free surface with virtually full intensity, and conversely. Consequently, the bigger cubes and SR150M sensors experienced energy loss that halted wave propagation before reaching the receiving sensors, necessitating a transition to the SRI150 sensors. [13] observes that the characteristics of the rock mass impact the propagation of seismic waves within the medium, influencing not only the velocity of the waves but also the relative amplitude and frequency content of the signals, a phenomenon known as signal degradation or attenuation. In a mining context, seismic waves traversing a host medium are influenced by the rock composition, backfill material, voids, stress conditions, and the nature and distribution of geological structures like as faults, shears, and joints.

4.2.2. Measurement setup

The choice of suitable AE sensors was determined by the operating frequency range of the AE transducer and the characteristics of the wave propagation medium. Specifically, the former must align with the frequencies at which corrosion is anticipated to produce acoustic emissions. In the [18] the medium through which the waves propagate is concrete, a material characterized by low-frequency propagation. Furthermore, [85] indicated that in concrete monitoring, although the sensitivity of acoustic emission sensors improves with a decrease in resonant frequency, transducers with a low resonance frequency of 30 kHz are susceptible to significant noise interference. Consequently, AE sensors operating within the frequency range of 60-400 kHz and exhibiting peak sensitivity above 75 dB were employed.

The peak definition time (PDT), hit definition time (HDT), and hit lockout time (HLT) are critical factors for acoustic emission data collecting. The Pulse Detection

Time (PDT) denotes the duration measured by a counter, which resets to zero upon the identification of a fresh maximum signal, preceding the assessment of the genuine peak of the AE waveform seen in Figure 12. The HDT denotes the duration, measured by a counter reset to zero upon threshold crossing detection, necessary for the system to determine the conclusion of a hit, complete the measurement procedure, and retain the characteristics of the recorded signal as depicted in Figure 13. The HLT is the duration after a hit's conclusion during which the system refrains from responding to any threshold crossings, serving to mitigate the measurement of reflections and delayed signals [18].

To prevent an extension of the AE activity period due to interfering reflections, PDT, HDT, and HLT were designated as 200, 400, and 3000 μs, respectively.

Table 3.
Summary of AE software settings

Parameter	**Unit**	**Value**
Threshold	dB	30
Parameters of timing		
PDT	μs	200
HDT	μs	400
HLT	μs	3000
Waveform setup		
Sampling rate	MSPS	10000
Sampling frequency	Points	10000
Digital filter		
Lower	kHz	60
Upper	kHz	400

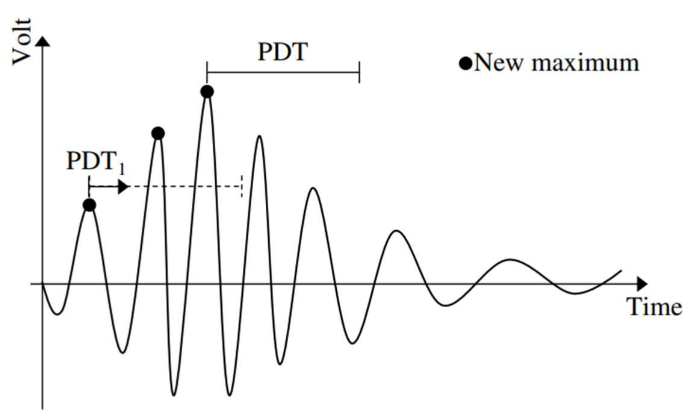

Figure 12. Peak definition time

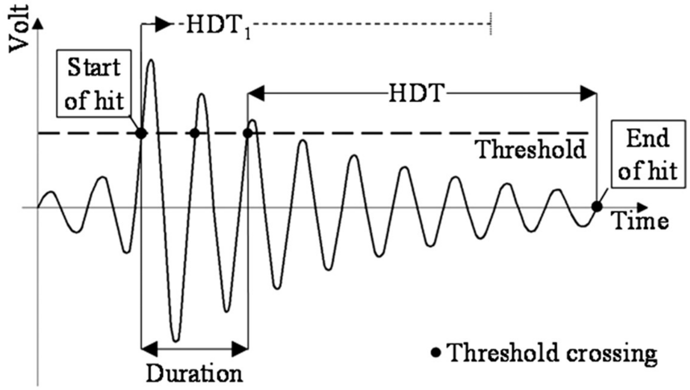

Figure 13. Hit definition time

4.2.3. Procedure of velocity calculation with AE equipment

[28] asserted that seismic monitoring systems primarily record the arrival timings of seismic waves, and by knowing the coordinates of the sensors and assuming a consistent velocity of seismic signal propagation through the rock, one can estimate the source location. Source location determination can be achieved through two primary methods: utilizing the arrival timings of P-waves exclusively or employing the arrival times of both P- and S-waves [28]. This research employed the direct approach of source localization as described by [6] and discussed by [28].

$$d_i = \sqrt{(x_i - x_1)^2 + (y_i - y_1)^2 + (z_i - z_1)^2} \tag{2}$$

Where $i = 2, 3, 4, 5, 6, 7, 8$ and *x, y, z* – sensor coordinates.

For each wave arrival time, the test was performed five times, and the mean arrival time at each sensor was employed to compute the wave velocity associated with that sensor.

Wave velocity was calculated using the equation that subtracts wave arrival time from wave creation time.

$$v = \frac{d_i}{\Delta t} \tag{3}$$

For each wave arrival time, the test was performed five times, and the mean arrival time at each sensor was employed to compute the wave velocity associated with that sensor.

The wave velocity was calculated using the equation that subtracts the wave arrival time from the wave creation time.

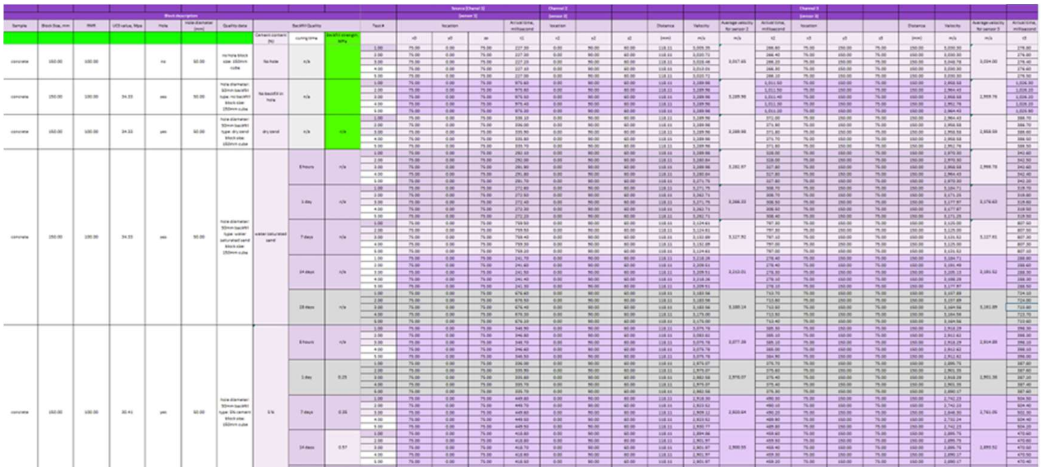

Figure 14. Snapshot of AE results database

The data collected, as illustrated in Figure 14 and detailed in Appendix 1, comprise the following:

- Material type (rock or concrete)
- Backfill characteristics, quality, and curing duration
- Source location for each material
- Wave arrival time at each sensor
- Calculated wave velocity at each sensor.

4.3. Analysis of results from AE tests

4.3.1. Size effect on seismic wave velocity

The research primarily aimed to examine the influence of size, voids, varying backfill compositions, and age on seismic wave velocity. Figure 15 illustrates the seismic wave velocities for cubes of varying diameters devoid of perforations. According to the test findings depicted in Figure 15, there is no substantial variation in seismic wave velocities with increasing cube size, except at sensor 7. The wave velocity vary from 3,000 to 3,500 m/s, which falls within the values of 3,160 to 3,818 m/s. The minor variations in velocities among the five cubes may be attributed to discrepancies in the concrete mix quality and potential inaccuracies in measuring wave arrival times.

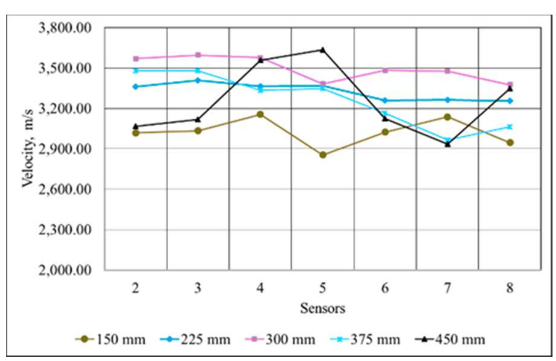

Figure 15. Seismic wave velocities on concrete cubes without holes

4.3.2. Hole effect on seismic wave velocity

Figure 16 illustrates the outcomes of acoustic emission measurements conducted on concrete cubes including voids. The test results in Figure 16 indicate that the velocities in the 150-, 225-, 300-, and 375-mm cubes with 50-, 75-, 100-, and 125-mm diameter holes are not considerably impacted when compared to their corresponding solid cubes. The velocity at the sensors for these cubes range from 3033 to 3577 m/s. The 450 mm cube with a 150 mm hole width exhibits a notable alteration in seismic wave velocity at sensors 2, 3, 6, and 7. Sensors 4 and 5 exhibit velocities of 3558 and 3635 m/s, respectively, indicating that they are unaffected by the void. Sensors 6 and 7 exhibit the most pronounced decline in velocities, over 1500 m/s, from the peak value in the 450 mm cube with a hole width of 150 mm. The considerable decrease in velocities is attributable to the positioning of the sensors directly opposite the source sensor. Wave energy attenuation is significant due to the vacant 150 mm diameter aperture and the disregarded influence of ray path tracing in the distance computation, leading to prolonged arrival times and consequently reduced velocities. The findings indicate that the assumption of straight ray routes was not substantially influenced by the holes in the smaller cubes; but, the 150 mm hole in the 450 mm cube did change the paths, with the extent of impact varying based on the sensor's position relative to the source and the hole.

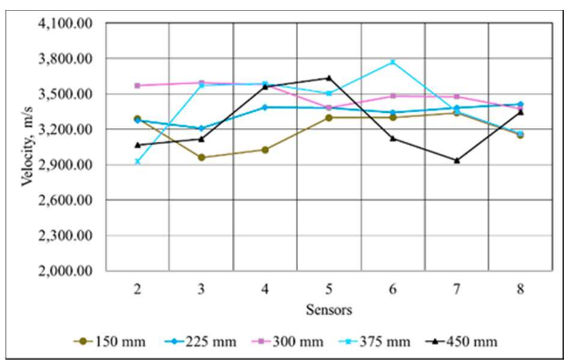

Figure 16. Seismic wave velocities in blocks with holes of different diameters at sensor locations

4.3.3. Backfill effect on seismic wave velocity

Figure 17 presents the seismic wave velocity outcomes for each backfill type at the cured age for wet sand (0% cement), 5% cement, and 20% cement, corresponding to a cube size of 150 mm with a hole width of 50 mm. The ray paths of sensors 2, 3, 4, and 5 in Figure 16a for wet sand remain unaffected by the backfill in the void, whereas the ray paths from the source to sensor 7 are considerably influenced by the void and its contents on days 14 and 28, when the wet sand would have dried. The elevated cement content backfill (15% and 20% cement) exhibits a diminished effect on wave velocity after 28 days of curing, as illustrated in Figure 17c. Figure 17b illustrates a general decline in velocities across all curing durations at sensors 5 to 8, which is ascribed to the void and its contents, as well as the positioning of these sensors in relation to the source. Figure 17c, featuring a backfill cement percentage of 20%, demonstrates a substantial influence of the void and its composition on the pulse wave velocities at sensors 5, 6, and 8, attributable to their respective proximities to the void and source. It is plausible to assert that, although straight ray pathways were presumed in the pulse wave velocity calculations, the influence of the void and its contents is evident without ray tracing, albeit it could be enhanced with ray tracing.

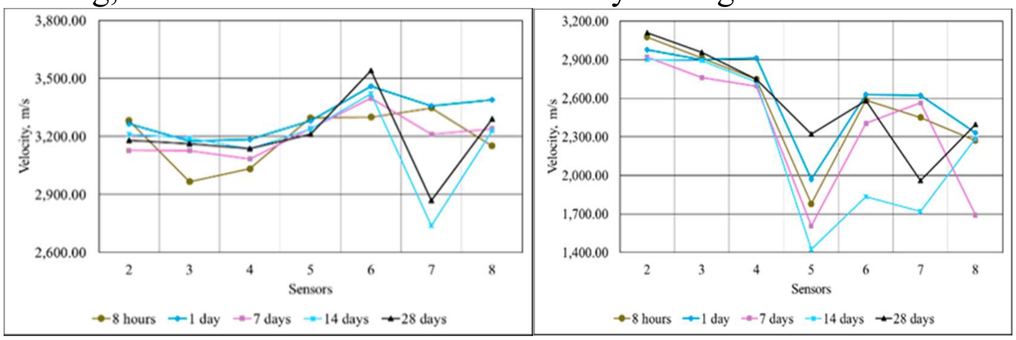

(a) Wet sand (0% cement) (b) 5% cement

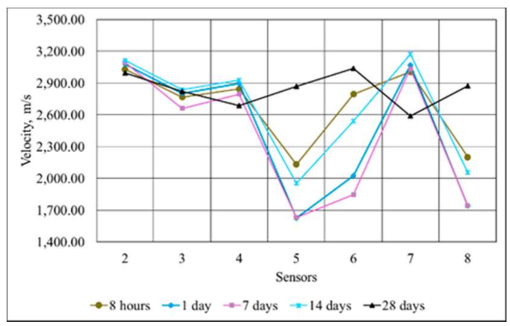

(c) 20% Cement

Figure 3. Backfill effect on seismic wave velocity for 150 mm cube with 50 mm diameter hole (a) Wet sand - 0% cement (b) 5% cement (c) 20% cement backfill.

Figure 18 illustrates the influence of the void and backfill effect on wave velocities at the receiving sensors on the 225 mm cube with 5% and 15% cement content backfill within the void. In Figure 18a, for a 5% cement content backfill, the wave velocities for all curing durations vary from 2879 to 3200 m/s, similar to the behavior observed in a concrete cube without a void. The pulse wave velocity is considerably influenced from the source to receiving sensors 2 and 4 in Figure 18b due to the presence of voids and backfill.

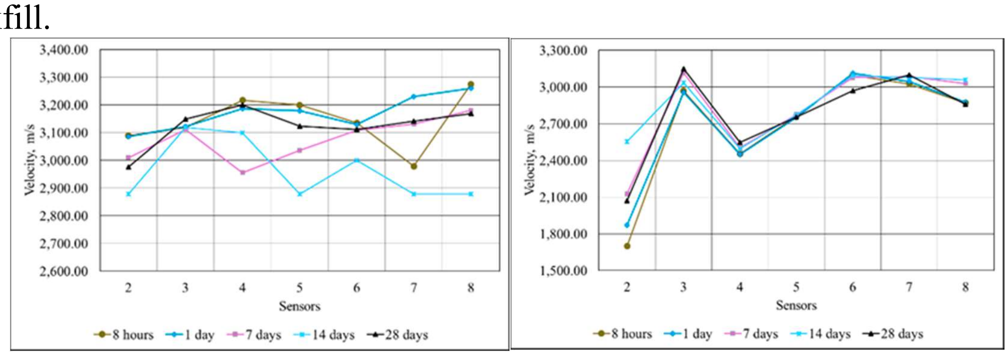

(a) 5% cement (b) 15% cement

Figure 4. Backfill effect on seismic wave velocity for 225 mm concrete cube with 75 mm diameter hole (a) 5% cement (b) 15% cement

Figure 19 illustrates the acoustic emission test results for the 300 mm granite cube with varying cement content backfills at different ages. Figure 19 a-d illustrates reductions in velocities at sensors 3, 4, and 7, indicating their positional relationship to the source and vacuum.

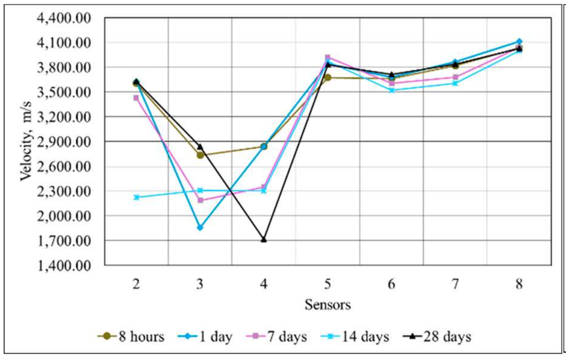

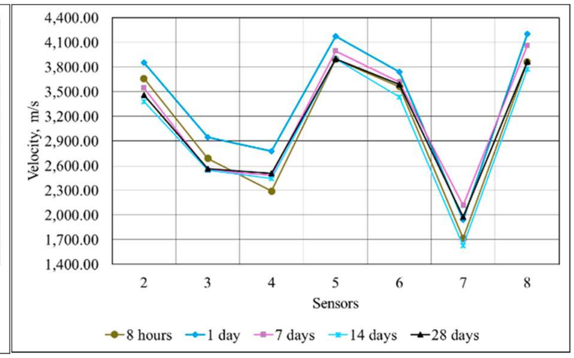

(a) 5% cement (b) 10% cement

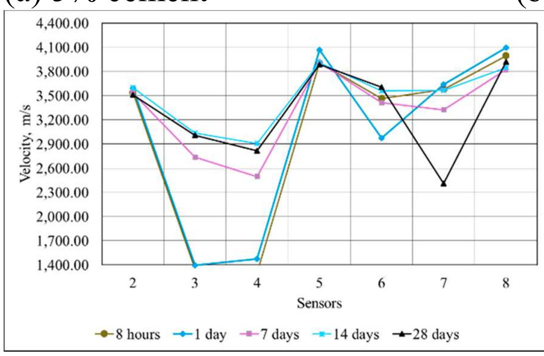

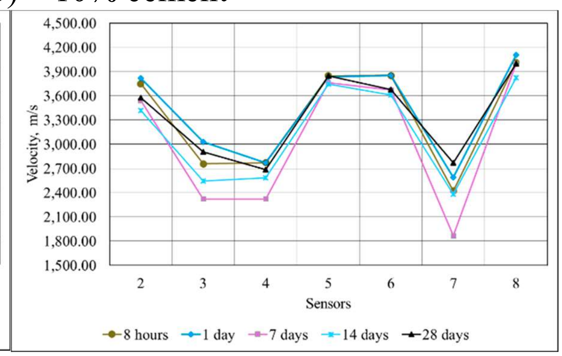

(c) 15% cement (d) 20% cement

Figure 5. Backfill effect on seismic wave velocity for 300 mm granite cube with 100 mm diameter hole (a) 5% cement (b) 10% cement (c) 15% cement (d) 20% cement

The velocities to the other sensors remain unaffected, indicating that their ray trajectories were not influenced by the void. The velocities at sensors 2, 5, 6, and 8 remain unaffected, ranging from 3600 m/s to 4100 m/s.

Figure 20 indicates that sensors 7 and 8 are considerably influenced by the 125 mm diameter void and the temporal alterations in backfill qualities within the 375 mm cube. The two sensors are positioned at the apex of the cube, adjacent to the void, and the wave pathways to these sensors are influenced by the vacuum and its contents to varying extents.

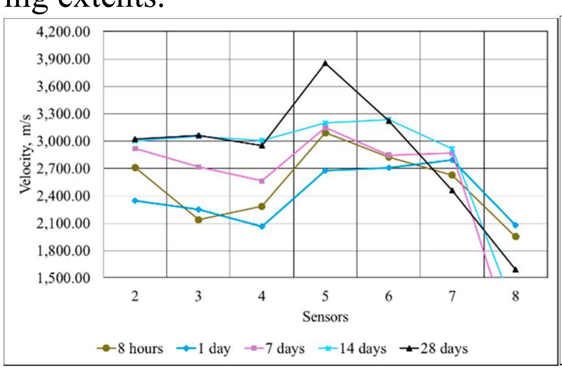

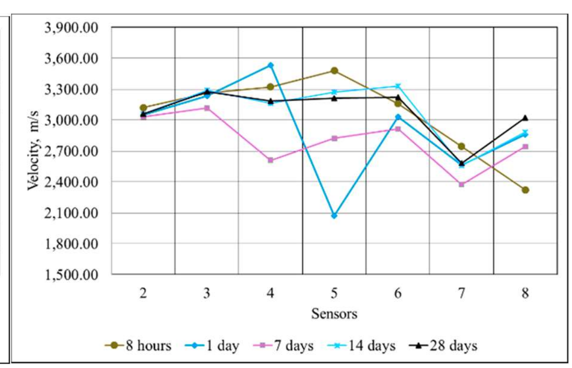

(a) Wet sand (0% cement) (b) 5% cement

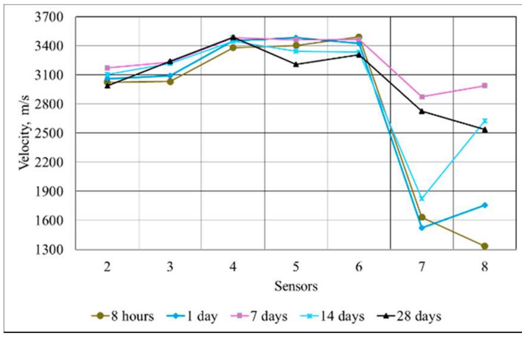

(c) 10% cement

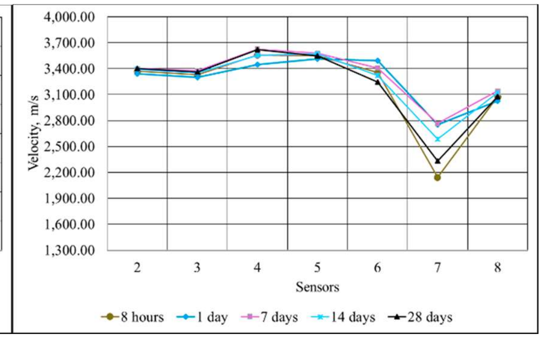

(d) 15% cement

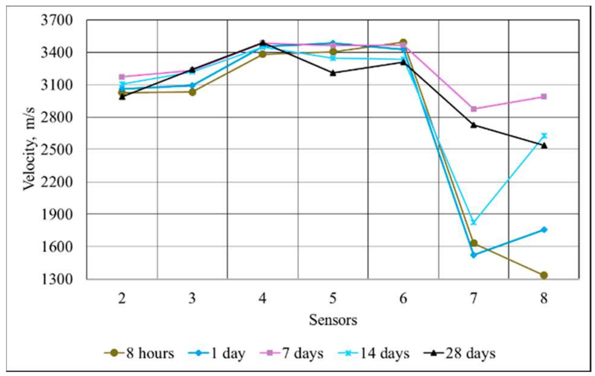

(e) 20% cement

Figure 6. Backfill effect on seismic wave velocity for 375 mm concrete cube with 125 mm diameter hole (a) wet sand (b) 5% cement (c) 10% cement (d) 15% cement (e) 20% cement backfill

Figure 21 shows the results of the impact of backfilled cement content with time on wave velocities at sensors attached to the 450 mm cubes with a void of 150 mm diameter at different locations relative to the source and void. In Figure 21a for wet sand with 0% cement, the velocities show lower values at sensors 2, 3, 7 and 8. This is due to the sensor locations relative to the void and source.

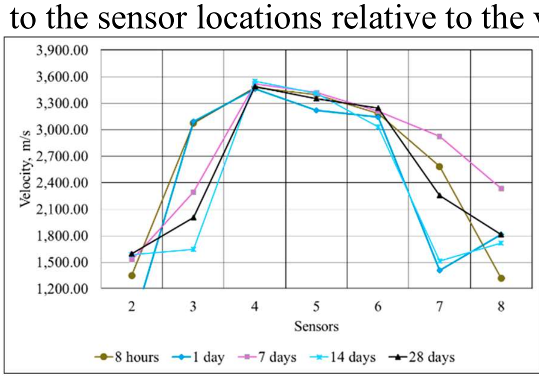

(a) Wet sand (0% cement)

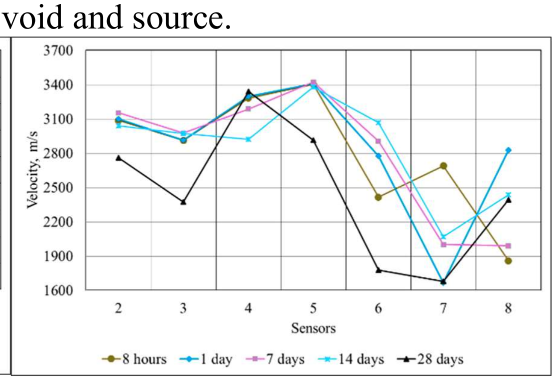

(b) 15% cement

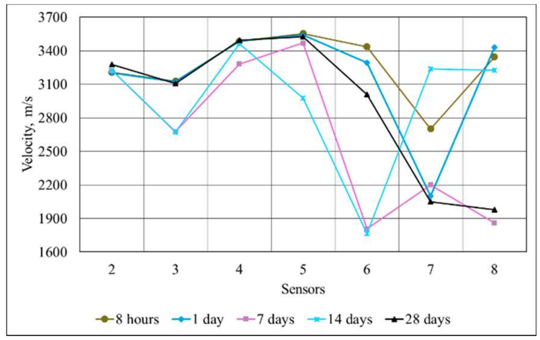

(c) 20% cement

Figure 7. Backfill effect on seismic wave velocity for 450 mm concrete cube with 150 mm diameter hole (a) wet sand (b) 15% cement (c) 20% cement backfill

4.3.4. Fracture effect on seismic wave velocity

Following the fragmentation of rock and concrete cubes, the SCA was extracted from the cavities. Fragmented components were systematically reassembled and secured with tape where required. Figure 22 illustrates the positions of the source and the sensors concerning the fissures in the concrete specimens.

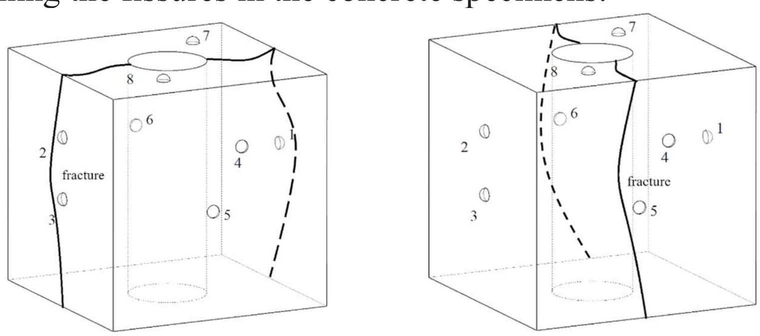

(a) (b)

Figure 8. The projected source and sensors' locations for a) 225 mm with hole diameter 75 mm b) 375 mm with hole diameter 125 mm concrete sample

Figure 23 illustrates the seismic wave velocity within a cracked cube including backfill. Sensors 1, 5, and 7, positioned before the fissures, accurately detected the signal. Conversely, sensors 3, 4, and 6 were unable to detect the signal or got a diminished signal due to signal attenuation in the cracks.

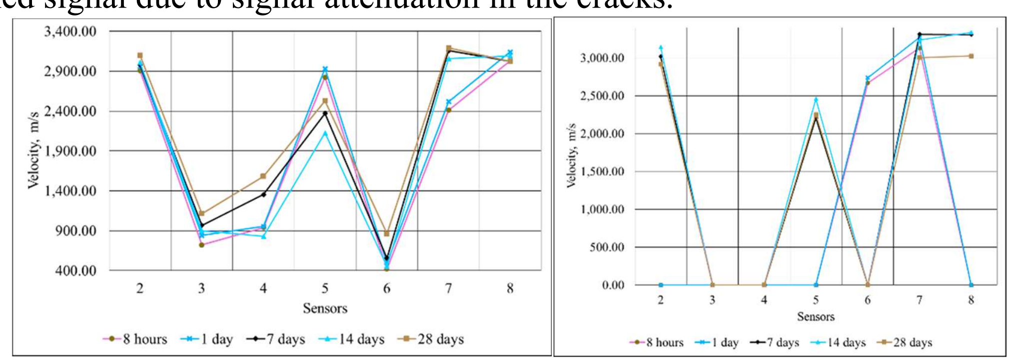

(a) 5% cement (b) 20% cement

Figure 9. Fracture effect on seismic wave velocity for 150 mm concrete cube with 50 mm diameter hole (a) 5% cement (b) 20% cement backfill

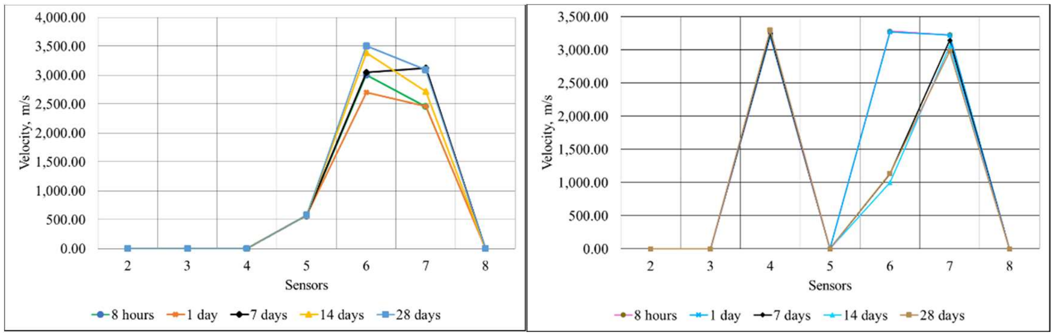

(a) 5% cement (b) 20% cement

Figure 10. Fracture effect on seismic wave velocity for 225 mm concrete cube with 75 mm diameter hole (a) 5% cement (b) 20% cement backfill

Upon filling the broken 225 mm sample with backfill, the cube exhibited two cracks in relation to the sensors. Figure 24a indicates that only sensors 5, 6, and 7 successfully received the signal. Sensor 5 is positioned opposite the hole relative to the source; yet, it may detect the signal with a delayed arrival time due to the fracture, as indicated by the reduced wave velocity of 500 m/s. The crack presumably contained infill from the backfill, facilitating the transmission of the pulse signal across the fracture at this sensor's site.

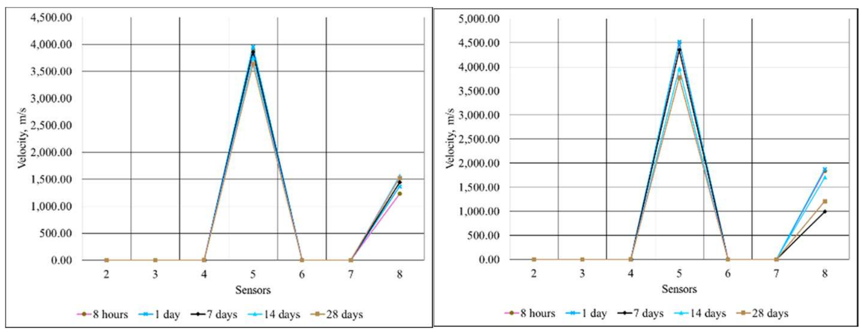

(a) 5% cement (b) 20% cement

Figure 11. Fracture effect on seismic wave velocity for 300 mm granite cube with 100 mm diameter hole (a) 5% cement (b) 20% cement backfill

In a 300 mm granite cube, only sensor 5 received an unattenuated full signal, while sensor 8 detected a weak signal due to its position before the crack; the remaining five sensors were unable to receive any signal due to complete attenuation caused by the crack.

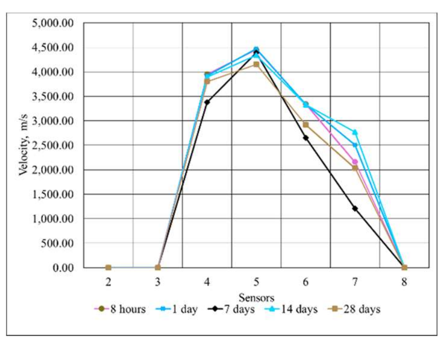

Figure 12. Fracture effect on seismic wave velocity for 375 mm concrete cube with 125 mm diameter hole filled with 15 % cement backfill

Two cracks were present in the 375 mm cubes containing 15% cement backfill. Figure 26 illustrates the seismic wave velocity within a cracked cube including backfill. Sensors 4, 5, 6, and 7, positioned before the cracks, accurately detected the signal. Conversely, sensors 2, 3, and 8 failed to detect the signal due to complete attenuation within the fissures.

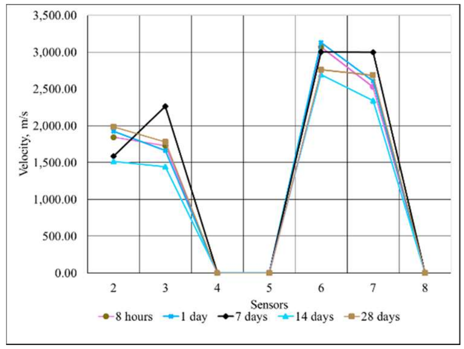

Figure 13. Fracture effect on seismic wave velocity for 450 mm concrete cube with 150 mm diameter hole filled with wet sand backfill

Two cracks were discovered in the 450 mm cube. Figure 27 illustrates the seismic wave velocities within a 450 mm cube containing fractures filled with backfill. Sensors 2, 3, 6, and 7, positioned in advance of the fissures, detected the signal as anticipated. Conversely, sensors 4, 5, and 8 failed to detect the signal, which was ascribed to complete signal attenuation caused by the cracks.

4.4. Rating of fractured blocks

An assessment of two prevalent rock mass categorization techniques, RMR and Q, was performed to ascertain their suitability for application to the specified fractured blocks. The rationale for choosing a categorization system was its ability to effortlessly shift from field-scale application to laboratory-scale use. RMR provides a benefit in the decision-making process by incorporating the rock mass uniaxial compressive strength as a crucial metric. This trait is crucial for distinguishing between weak and strong rock formations that have analogous structural characteristics. Consequently, RMR became the favored option for evaluating the fragmented blocks in the laboratory. The RMR system presented in Table 8 [5] was employed to evaluate the characteristics of the blocks post-fracture. Prior to the computation of RMR, the following procedures were executed in accordance with the RMR determination protocol established by [5]:

- Enumeration of all fractures within the block - Measurement of the apertures of the fractures - Measurement of the lengths of all fractures

Assessment of the roughness of each fracture

Table 4.
RMR system [5]

Parameter	RMR							
	1973	1974	1976	1979	1989	2011	2013	2014
Intact rock strength (MPa)	10-0	10-0	15-0	15-0	15-0	15-0	15-0	15-0
RQD (%)	16-3	20-3	20-3	20-3	20-3	20-0	-	-
Joint spacing (mm)	30-5	30-5	30-5	20-5	20-5	20-0		
Discontinuity density (Joints per meter)	-	-	-	-	-	-	40-0	40-0
Separation of joints (mm)	5-1	-	-	-	-	-	-	-
Continuity of joints (m)	5-0	-	-	-	-	-	-	-
Weathering	9-1	-	-	-	-	-	-	-
Condition of joints	-	15-0	25-0	30-0	30-0	30-0	30-0	20-0
Groundwater	10-2	10-2	10-0	15-0	15-0	15-0	15-0	15-0
Alterability (%)	-	-	-	-	-	-	-	10-0
Adjustment F_0	15-3	15-3	0-(-12)	0-(-12)	0-(-12)	0-(-12)	0-(-12)	0-(-12)
F_e	-	-	-	-	-	-	-	1.32-1
F_s	-	-	-	-	-	-	-	1.3-1

Fo - adjustment factor for the orientation of tunnel axis, Fe - adjustment factor to account for an excavation method and Fs - adjustment factor considering stress-strain behavior of the rock mass at the tunnel face.

4.4.1. Scaling of RMR parameters

[80] emphasized the necessity of appropriately scaling results from a physical model to align with actual mining circumstances. They observed that attaining total congruence between physical models and real mines is difficult; however, geometric similarity is the crucial element and may be very easily accomplished in a physical simulation. To appropriately depict the dimensions of concrete blocks that replicate mining settings, characteristics such as Rock Quality Designation (RQD), fracture length, and spacing must be modified.

Geometric similarity was identified as the fundamental factor in scaled physical models, as highlighted by [80]. The research executed particular scaling modifications for fractures, concentrating on the subsequent metrics:

$$l_m = \emptyset * l_d \tag{4}$$

Where l_m signifies the length of the fracture inside the simulated in situ rock mass,, ϕ represents the length scale coefficient, and l_d refers to the length of discontinuity employed in the RMR system for assessing in situ conditions.

$$s_m = \beta * s_d \tag{5}$$

s_m denotes the spacing of fractures in the mimic model, s_d signifies the spacing of discontinuities in the RMR system rating, and β represents the length scale coefficient. Table 6 displays the modified values for distinct cube dimensions, calculated using the length scaling factors obtained from equations 4 and 5, in accordance with the joint condition rating method established by [5] for in-situ rock formations. The RMR parameters necessitating scaling from in situ to laboratory scale models are RQD and fracture attributes.

4.4.1.1.1. RQD scaling

In 1967, Deere [17] first presented the Rock Quality Designation (RQD) framework as a uniparametric system for the characterization of rock masses. RQD is a modified metric for core recovery percentage, calculated by dividing the cumulative length of unbroken core samples longer than 100 mm by the overall length of the core run. The sensitivity of RQD to the core traverse extent is recognized, leading to the advice by [66] that its calculation should be based on real field-derived drill lengths, ideally restricted to 1.5 meters.

In 1982, Palmstrom established the notion of volumetric joint count (Jv) for quantifying joint occurrences in rock masses [61]. Jv represents the quantity of joints per cubic meter and is determined by enumerating the joints within a certain area and dividing that count by the area [61]. Palmstrom in the [61] presented Equation (6) that correlates Jv with RQD.

$$RQD = 110 - 2.5J_v \tag{6}$$

This research employed the Jv approach to ascertain RQD in fragmented blocks. The methodology for calculating the scaled RQD from the broken blocks is outlined in Section 4.5.4.

(a) 2 fractures in 375mm cube (b) 3 fractures in 150mm cube

Figure 14. Fractured cubes with different fracture patterns and densities

4.4.1.2. Calculations of the scaled RQD

Palmstrom in the [62] indicates that in the absence of borehole or scanline logging data, as in this work, Equation (6) can be utilized to determine RQD from Jv, which is necessary for the Q and RMR classification systems. Equation (6) can be reformulated as presented in Equation (7):

$$RQD=110-2.5(K.J_s) \tag{7}$$

Js denotes the density of joints per unit area in a two-dimensional framework, as ascertained via window mapping. The transformation of Js to Jv in a three-dimensional environment is accomplished via the factor K, such that Jv = K * Js. The value of K generally lies between 1.25 and 1.35 under conventional conditions, however with uniformly distributed joints in all directions, it varies from 1.15 to 1.5, as per Palmstrom [61]. Palmstrom in the [62] determined that Equation (7) is applicable for Jv values ranging from 4 to 44. Outside this region, the Rock Quality Designation (RQD) metric exhibits diminished sensitivity to joint frequency. The concordance between Jv and RQD corroborates the apprehensions earlier articulated by Palmstrom in the [62], along with those of [52, 25]. Nonetheless, given the lack of a substitute, RQD remains a crucial component of rock mass classification systems.

This study evaluated the number of fractures from a plan perspective of each cube. Table 5 delineates the fracture count per unit area for different cube dimensions, as well as the factors necessary for RQD calculation. The dimensions of each cube's plan view determine the size of the surrounding window used for fracture counting.

The subsequent phase requires the identification of appropriate scaling factors to accurately adjust the field's window mapping area to the plan view area of the laboratory's cubes. The ultimate dimensions of the window utilized in geotechnical mining depend on various aspects, including project-specific goals, data type, available resources, and equipment. Window diameters typically range from a few millimeters to several meters, depending on the extent of the mining operation and the required complexity for mapping and geotechnical activities. The dimensions of the window for RQD calculation depend on the excavation's size and the exposed surface area.

4.4.1.3. Scaling cube fracture area density from field window mapping practice characteristics

To compute Js in Equation (7), it is essential to modify the fracture density from the plan view area of the laboratory-scale cubes to correspond with the dimensions of the mapping windows for in situ rock mass assessment.

[56] examined methodologies for mapping geological characteristics to evaluate slope stability. They proposed that, contingent upon the available region for mapping, the mapping window should typically extend approximately 10 meters in length. In mapping open pit regions with significant exposed rock, bigger window widths, typically spanning tens to hundreds of meters, are frequently employed. [77] and [29] utilized window dimensions ranging from 90 meters by 45 meters to 130 meters by 65 meters to investigate the reliability of slope stability. They determined that employing rectangular windows for mapping was superior to utilizing circular ones. [3] conducted another investigation with smaller window dimensions of 1.9 meters by 2.2 meters for

excavations varying in size from 3 meters by 4 meters to 6 meters by 6 meters. They employed a 1 meter by 1 meter window, as indicated by the research of [88]. [78] referencing the work of [56], established rules for ascertaining window size in slope stability mapping. [78] proposed that the roughness of discontinuities should preferably be assessed on exposed surfaces measuring at least 2 meters in length, if feasible. [42] employed a window measuring 1 meter by 0.67 meters on a rock outcrop. [56] emphasized that assessing roughness on exposed surfaces measuring a minimum of 2 meters in length in the field could serve as a foundation for establishing a suitable window size. Circular window mapping [74] has also been proposed; however, this study exclusively concentrated on rectangular or square designs and did not take circular windows into account.

[43] employed window dimensions of 1.8 meters by 1.8 meters in an underground hard rock mine. Besides the dimensions of subterranean excavations determining window size, [51] noted that the mapping height is typically constrained to approximately 2 meters. This is due to the improbability of an individual safely attaining a height above 2 meters in contact mapping, irrespective of the general accessibility of the rock exposure.

4.4.1.4. Scaled RMR for fractured cubes

Given the aforementioned window size possibilities and methodologies, it is prudent to propose a window dimension of 2 meters by 2 meters as adequate and appropriate for subterranean mapping to ascertain fracture density (Js). This window dimension enables the laboratory-scale cubes to be enlarged to match the field window size. Table 5 presents the conversion factors for various cube dimensions utilized in this investigation.

Table 5.

Conversion factors for scaling laboratory-scale plan view fracture densities (Jls) to field-scale fracture densities (Js) and RQDs.

Cube side length (m)	Window size (plan view): Area (m^2)	Scaling factor	Number of fractures	J_{ls}	J_s	J_v	RQD (%)
0.150	0.0225	1:13	3	133	10.2	13.4	77
0.225	0.0506	1:9	3	59.3	6.59	8.56	89
0.225	0.0506	1.9	2	39.5	4.39	5.71	96
0.300	0.0900	1:7	2	22.2	3.17	4.17	100
0.300	0.0900	1.7	3	33.3	4.75	6.18	95
0.300	0.0900	1.7	8	88.9	12.7	16.51	69
0.375	0.1406	1:5	2	14.2	2.84	3.70	100
0.450	0.2025	1:4	2	9.9	2.47	3.21	100

According to Section E of [5] table on Rock Mass Rating (RMR) variables, all fractures within the cubes are classified as dry, rough, unweathered, and free of infilling. These attributes correlate to scores of 0, 5, 6, and 6, yielding a total rating of 17. Table 6 displays the factor ratings for RMR along with their corresponding values for the examined mortar cubes.

Following a curing time of 28 days, core samples were taken from the mortar cubes and subsequently fractured. The samples were subsequently subjected to uniaxial compressive strength (UCS) tests. The uniaxial compressive strength values for the shattered cubes, presented in Table 6, indicate a notable diversity in the strengths of the mortar cubes. Furthermore, fracture spacing, lengths, and apertures were measured in each broken block from a plan view perspective.

Table 6.

RMR calculations for each fractured cube.

Cube side length (mm)	RQD		Fracture spacing		Fracture aperture		Fracture length		UCS		RMR
	(%)	Rating	(m)	Rating	(mm)	Rating	(m	Rating	MPa	Rating	
150	77	17	0.65-1.30	15	0.1-1.0	4	0.98-1.95	4	34	4	61
225	89	17	0.68-1.35	15	1-5	1	1.0-2.03	4	19	2	56
225	96	20	0.68-2.1	1[illegible]	1-5	1	1.0-2.03	4	32	4	61
300	100	20	0.70-2.10	15	1-5	1	1.05-2.10	4	26	4	61
300	95	20	0.14-0.28	10	5.56	0	0.28-0.91	6	32	4	57
300	69	13	0.035-0.28	10	2.47	1	0.14-0.91	6	32	4	51
375	100	20	0.63-1.88	15	>5	0	1.31-2.63	4	24	2	58
450	100	20	0.60-1.80	15	1-5	1	0.90-1.80	4	12	2	59

The findings indicate that expanding the in situ RMR system to laboratory-scale physical models for fractured concrete blocks is viable. Scaled RMR values will be utilized to evaluate fractured cubes to assess the impact of fracture intensity on seismic wave velocity.

4.5. Summary

Chapter 4 presents an experimental research aimed at examining the features of AE signal propagation to signal receivers under challenging conditions, utilizing laboratory physical models that replicate the intricate mining environment. The subsequent results are drawn from the acoustic emission measurements conducted on different circumstances of concrete and granite samples:

- In isotropic homogeneous (intact) blocks, the assumption of a straight raypath is valid, allowing for the safe application of constant and layered velocity models in the presence of voids and cemented backfills; - The impact of voids and backfills on acoustic emission signal travel time is insignificant in small 150 mm blocks. Nevertheless, when block size and void diameter rise, together with backfill in the voids, the signal travel time to sensors escalates; - the existence of fractures results in signal attenuation contingent upon the sensors' proximity to the crack and the source.

Additionally, it was essential to segment the block models to replicate stress-induced fracturing resulting from mining activities. The SCA fractured the samples to varying extents based on their quality. To evaluate the characteristics of the fractured samples, the rock mass classification method was employed. RMR was chosen for this purpose due to the scalability of its constituent parameters. The RMR parameters necessitating scaling from in situ to laboratory scale models are RQD and fracture attributes. The findings indicate that the scaling of the in situ RMR system to laboratory-scale physical models for the cracked blocks is viable.

5. DYNAMIC NUMERICAL MODELING

Laboratory studies involving concrete cubes and acoustic emissions were simulated using dynamic numerical modeling in FLAC3D to enhance the understanding of wave propagation characteristics and their sensitivity to diverse medium variables.

5.1. Model Construction and Input Parameters

The model was not exposed to external loading, indicating that no initial stresses were imposed on it. The laboratory AE tests did not involve external force on the blocks. A solid cube with no voids was constructed using a brick with a side length of 300 mm. A cylindrical brick with reflections at both ends was placed on the solid cube to depict a cube with a hollow interior. In the laboratory testing, sensor number 1, which emits the signal, is represented on the model as a red dot according to the established geometry and location (Figure 29). The developed model was employed to examine the influence of diverse circumstances on seismic wave velocity (sensitivity analysis) within the granite and concrete cubes and to comprehend the underlying physics of the issue. The model's input parameters were modified to simulate various rock types in order to analyze the influence of different rocks on seismic wave velocity.

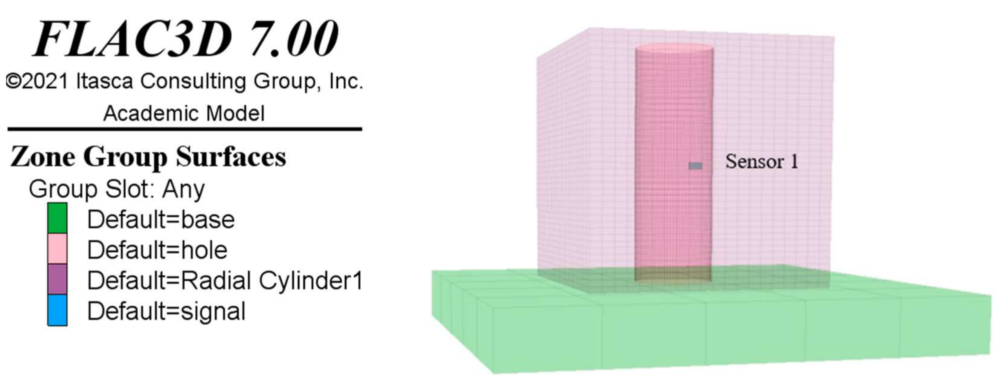

Figure 15. Geometry of the granite cube, with and without hole. Without hole, the green cylinder and the rest of the block have the same properties and with hole it is assigned the properties according to the code guidelines.

The elastic characteristics of granite and concrete samples were derived from laboratory research. Table 7 presents the input parameters of the model.

Table 7.
Granite and concrete properties

Parameter	Concrete	Granite
UCS	25 MPa	153.3 MPa

Tables 7 continued

Parameter	Concrete	Granite
Young's modulus	18.3 GPa	66.56 GPa
Poisson's ratio	0.28	0.23
Shear modulus	11.7 GPa	27.01 GPa
Bulk modulus	17.8 GPa	41.1 GPa
Density	2.4 g/cm3	2.7 g/cm3

Damping must be implemented in a system exposed to dynamic loads; otherwise, the system will oscillate perpetually. FLAC 3D incorporates three damping choices within its code: Rayleigh damping, local damping, and artificial viscosity damping. Local damping was selected for this study. Local damping is incorporated in the FLAC 3D static solution and can be utilized for dynamic analysis when the input time history is uncomplicated. The essential damping ratio is often between 2% and 5%, as determined in laboratory tests; this investigation utilized a value of 5%.

5.2. Boundary Conditions

In dynamic studies, the imposition of boundaries on the model may result in the reflection of applied propagating waves back into the model. Employing a larger model may mitigate this issue; however, it consequently results in more processing time. An approach is to employ a silent (quiet, viscous, or absorbing) border to address the issue. The silent boundary functions within the time domain and is predicated on the utilization of independent dashpots in both the normal and shear directions at the model boundaries. According to [30], a quiet border effectively absorbs propagating waves when the angles of incidence exceed 30°. The silent border is most appropriate for dynamic sources applied within a grid. The side borders of a model should not be utilized when the dynamic source is applied at the top or bottom bounds, as the propagating wave will escape via the side boundaries. In this instance, a quiet boundary was implemented at the bottom, while a free-field boundary was utilized for the remaining sides of the cube.

5.3. Model Meshing

The process of mesh production in FLAC for this arrangement is relatively uncomplicated. The maximum grid size is constrained in the dynamic setup to provide appropriate seismic wave propagation. According to [41, 30] the element dimension, Δl, should not exceed $\Delta l < \lambda/10$. The designated wavelength, λ, corresponds to the greatest frequency component of the input ground motion that possesses substantial energy.

The maximum size of the finite difference grid was determined using Equation 8, where Δl represents the spatial element size, λ and f denote the wavelength and frequency of the highest frequency component with significant energy, respectively, and V_s is the average velocity derived from AE experiments in Equation 8:

$$\Delta l < \frac{\lambda}{10}$$

$$f < \frac{V_s}{10 \times \Delta l} \tag{8}$$

In equation 8, V_s = 3000 m/s, Δl< 2.29 mm.

5.4. Applied Signals and Histories

Acoustic Emission (AE) analysis utilizes various parameters to measure the features of AE signals, such as the count of AE events, amplitude, ringing count, impact technique, rise time, duration, and additional factors [77]. The maximum value of an AE signal's amplitude is utilized to categorize the type of AE source. The energy associated with an AE event is determined by the area that lies between the waveform envelope and the threshold voltage line. The ringing count indicates the intensity and frequency of the AE signal, determined by the number of peaks that surpass the threshold. The duration of the AE signal, measured from threshold to threshold time, captures all AE activities throughout this interval, thereby offering valuable insights into the variations in the local stress characteristics of materials. The parameters are illustrated in Figure 31 and computed for the two scenarios presented in Table 8.

From the laboratory work conducted with the AE system, two wave signals were obtained. AE represents a wave produced by an abrupt release of energy. Following amplification and digitization, an acoustic emission signal is depicted as a voltage versus time graph. Figure 30 illustrates the AE signal acquired for the solid cube scenario.

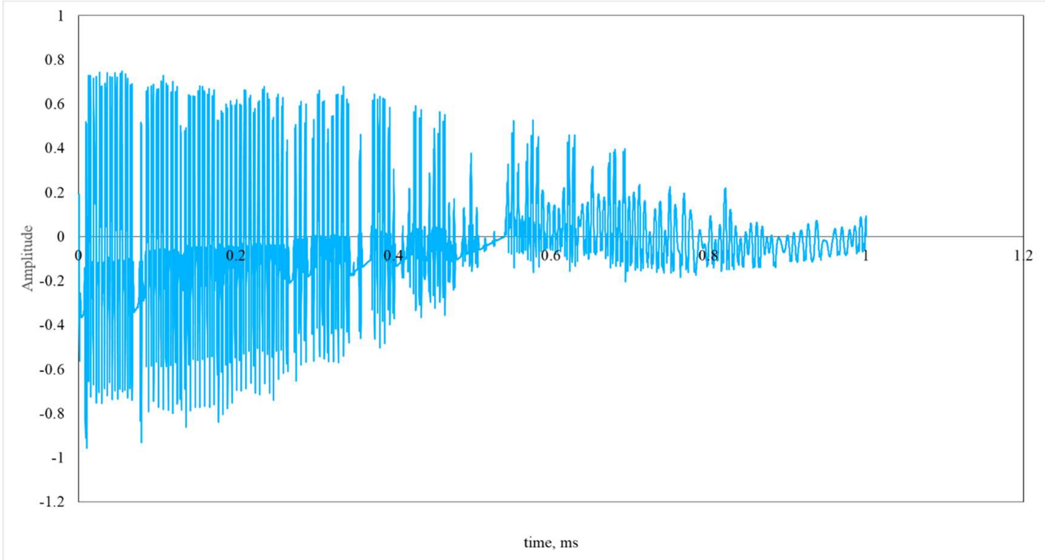

Figure 16. AE signal for solid cube case

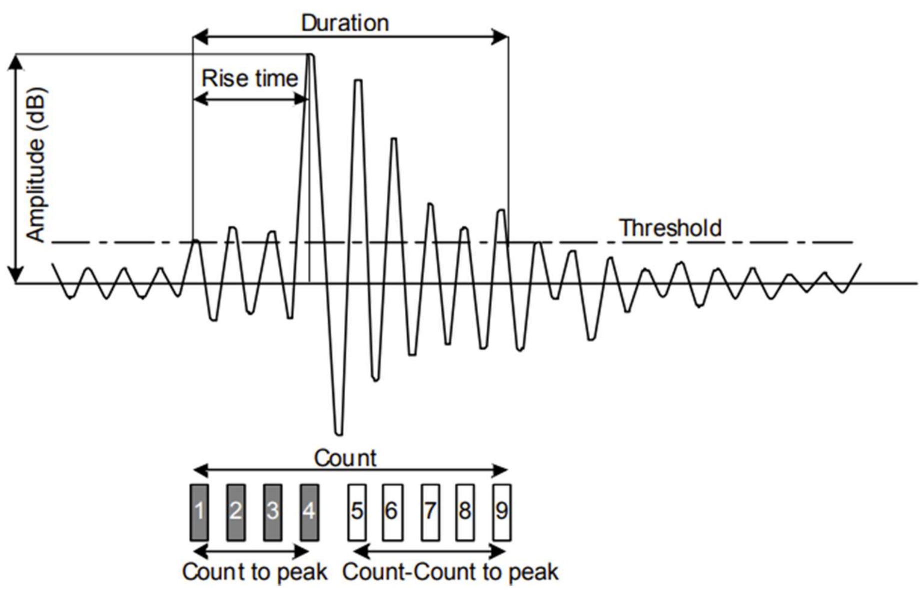

Figure 17. Definition of AE signal features [26]

Table 3.
Results from Channel 1

Experiment	Amplitude	Counts	Rise Time	Duration	Energy
Solid Cube	59.6	251	3	123	4.05
Empty Hole	59.4	323	3	975	4.593

The The time history can serve as an internal dynamic load at grid points within the model or as an external dynamic load at the model's boundary. Dynamic loading can be applied through four fundamental methods: as a time history of acceleration, as velocity, as stress (or pressure), and as force. FLAC indicates that the first and second alternatives are applicable in scenarios involving rigid bases, whereas the third and fourth options are suited for cases with flexible bases.

The discrete measurement of the initial load results in an input time history that may display a pronounced peak velocity, a short rise-time, and a significant high-frequency component. This presents a challenge for simulation calculations, as the element dimension, Δl, needs to be less than 1/10 of the wavelength (λ) to effectively represent the high-frequency component. Consequently, an increase in frequency necessitates a more refined grid generation in FLAC. To address this issue, a filtering process can be implemented on the input time history, eliminating the high frequency components. This allows FLAC to employ a coarser grid generation while maintaining the accuracy of the results. The Bandpass computer code was utilized in this study to filter the time history, effectively removing both low and high frequencies, thereby tackling the previously mentioned challenge [31].

The subsequent steps were undertaken to ready the data for the filtering process:

1. The SWAE software, which is bundled with AE equipment, presents the raw data for acceleration, velocity, and displacement over time, as well as their associated frequency spectrums.

2. The raw data undergoes processing through a Butterworth filter, an Infinite Impulse Response (IIR) technique known for its precision and smooth frequency response, characterized by a gradual change in amplitude.

3. Low frequency components are eliminated to remove motions that persist longer than the shake, as these enduring motions result in non-zero velocities and continuous movement at the conclusion of the velocity and displacement measurements.

The filtering process was accomplished using a Fourier transformation. The process of Fourier transformation takes an input signal and transforms it into a series of sinusoidal waves, each characterized by distinct amplitude, frequency, and phase variations. The plot that results from amplitude versus frequency is referred to as the Fourier amplitude spectrum, while the plot of phase angle is termed the Fourier phase spectrum. The primary frequency of the original wave is determined through the Fourier amplitude analysis. The FFT analysis results for granite cubes are presented in Figure 32.

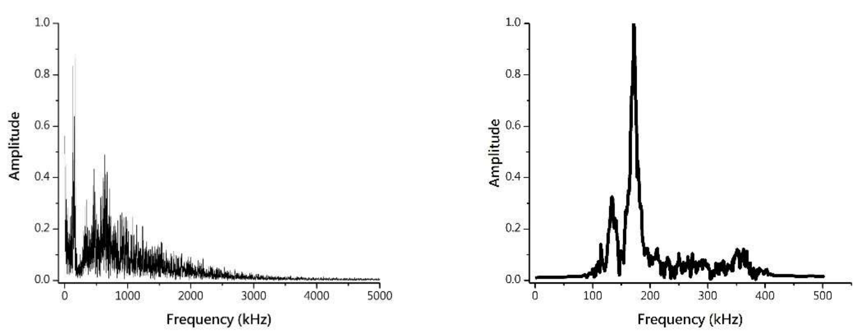

a) b)

Figure 18. FFT analysis for a) granite material b) concrete material

A baseline correction was subsequently executed to ensure that both the residual velocity and displacement equated to zero. This procedure aims to ensure that FLAC does not display ongoing velocity or residual displacements once the motion has concluded.

5.5. Parametric analysis

The model's validation was accomplished by comparing the data produced by the model with the experimental results obtained. This analysis encompassed essential wave characteristics including velocity, amplitude, and attenuation. After validating the model with experimental data, the elastic properties and wave frequency of granite were modified to reflect those of concrete and sandstone. This modification was designed to examine the resulting variations in wave velocity across the various materials. Figure 33 depicts the positioning of sensors relative to the source. Tables 9 and 10 present the calculated wave velocity at each sensor for the granite cube with an empty hole and the solid granite cube, respectively, based on the experimental data obtained from laboratory tests using the AE equipment. Tables 9 and 10 indicate that sensors 2 and 3 exhibit the lowest velocities, attributed to their positioning at the greatest distance from the source, which results in increased signal attenuation.

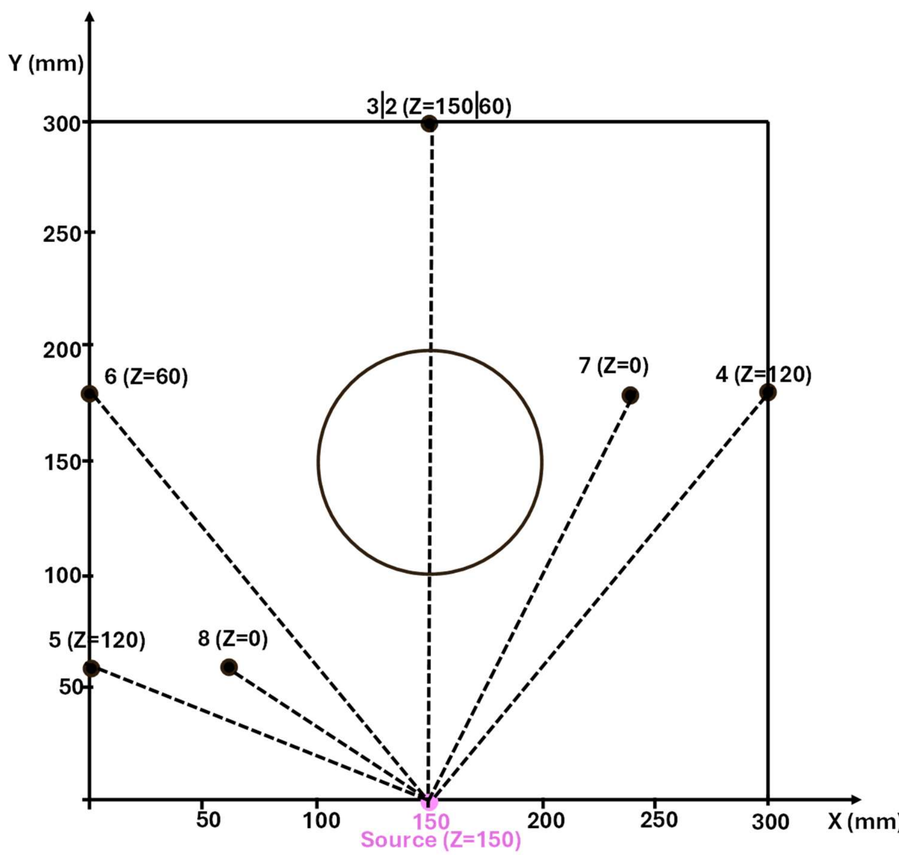

Figure 19. Location of sensors from the source (plan view of 300-mm cube: hole diameter is 100 mm)

Table 4.

Calculated wave velocity at each sensor in granite cube with empty hole

Sensor	Velocity, m/s
1	Source
2	2378
3	1923
4	3786
5	2564
6	2733
7	4031
8	2554

Table 5.

Calculated wave velocity at each sensor in solid granite cube

Sensor	Velocity, m/s
1	Source
2	3343
3	3442
4	4209
5	3906
6	4076
7	3936
8	3857

The numerical model was enhanced by incorporating two checkpoints aligned with the coordinates of sensors 2 and 5, allowing for the assessment of velocities at those precise locations. The graphs illustrated in Figure 34 showcase both experimental and modeled data for a granite cube featuring an empty hole at sensors 2 and 5. Figure 35 presents both experimental and modeled data pertaining to a solid granite cube. The experimental data, derived from AE test results, yields a unique arrival time at each sensor with established locations. Utilizing this information enables the calculation of velocity at each sensor. The velocity graph for the experimental data was created by interpolating the initial and final points related to velocity and time.

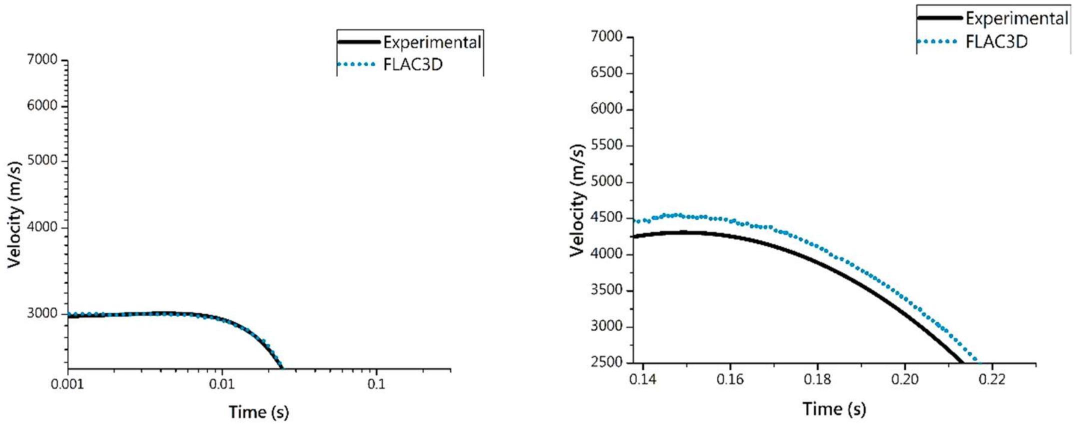

a) b)

Figure 20. Experimental versus modelled velocity in granite cube with empty hole at sensors a) 2 and b) 5

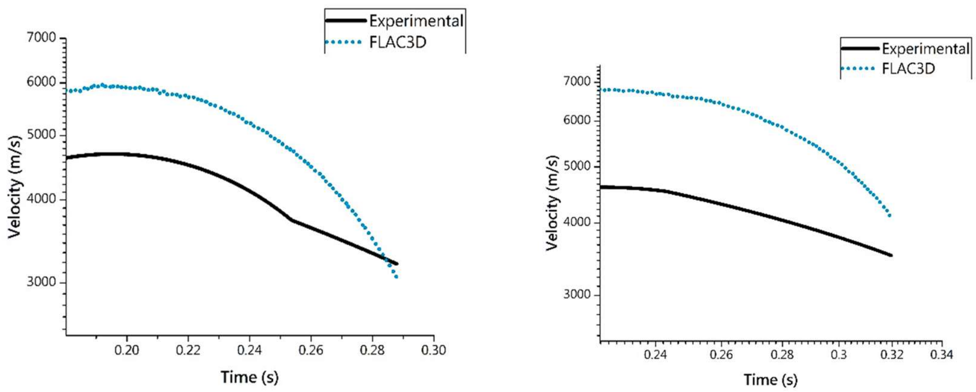

a) b)

Figure 21. Experimental versus modelled velocity in solid granite cube at sensors a) 2 and b) 5

The dynamic modelling results of the solid granite cube, as illustrated in Figure 36, demonstrate wave propagation at time intervals of 0.1 ms and 1 ms following wave generation from the source across the cube.

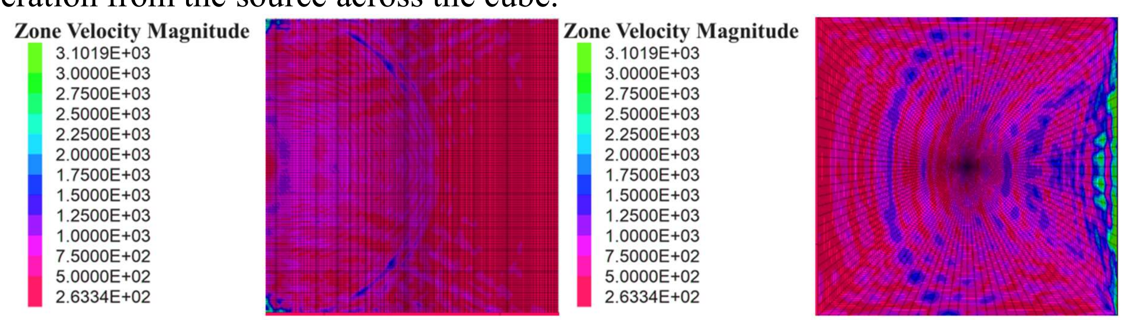

a) b)

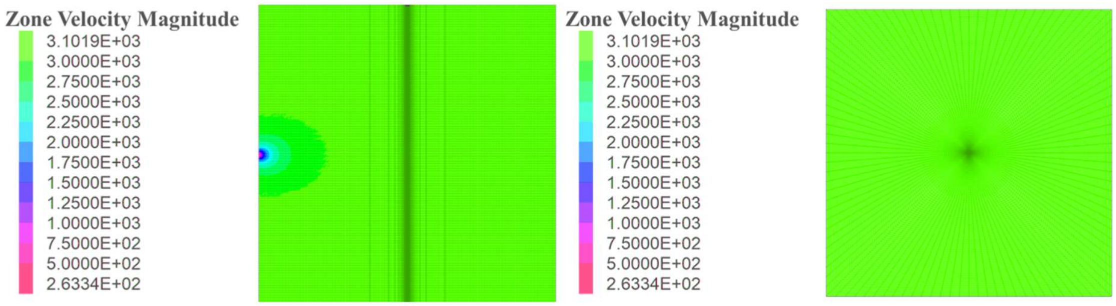

c) d)

Figure 22. Wave velocity in solid granite cube after 0.1 ms a) section view b) top view and 1 ms c) section view d) top view

Figure 37 illustrates the results of dynamic modeling for a granite cube featuring an empty hole. The illustrations present snapshots of wave propagation at 0.1 ms and 1 ms, showcasing both top and sectional views. The findings presented in Figures 36 and 37 clearly indicate that the presence of a void significantly influences wave velocity. The emergence of a void causes signal attenuation, leading to a reduction in velocity.

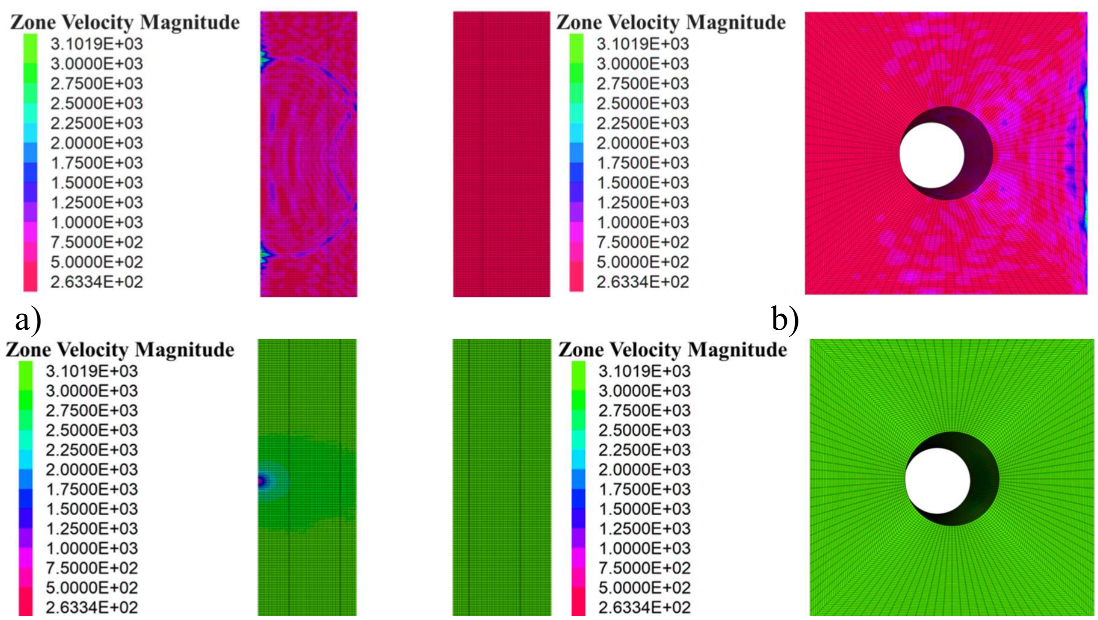

Figure 23. Wave velocity in granite cube with empty hole after 0.1 ms a) section view b) top view and 1 ms c) section view d) top view

Figures 38 and 39 illustrate similar modeling outcomes for concrete material, incorporating modifications to material properties as detailed in Table 7. The visual representations illustrate wave propagation snapshots at 0.1 ms and 1 ms, including both top and sectional views. The observations from Figures 38 and 39 clearly indicate that the existence of a void has a substantial impact on wave velocity, reflecting the trend noted in the granite material analysis.

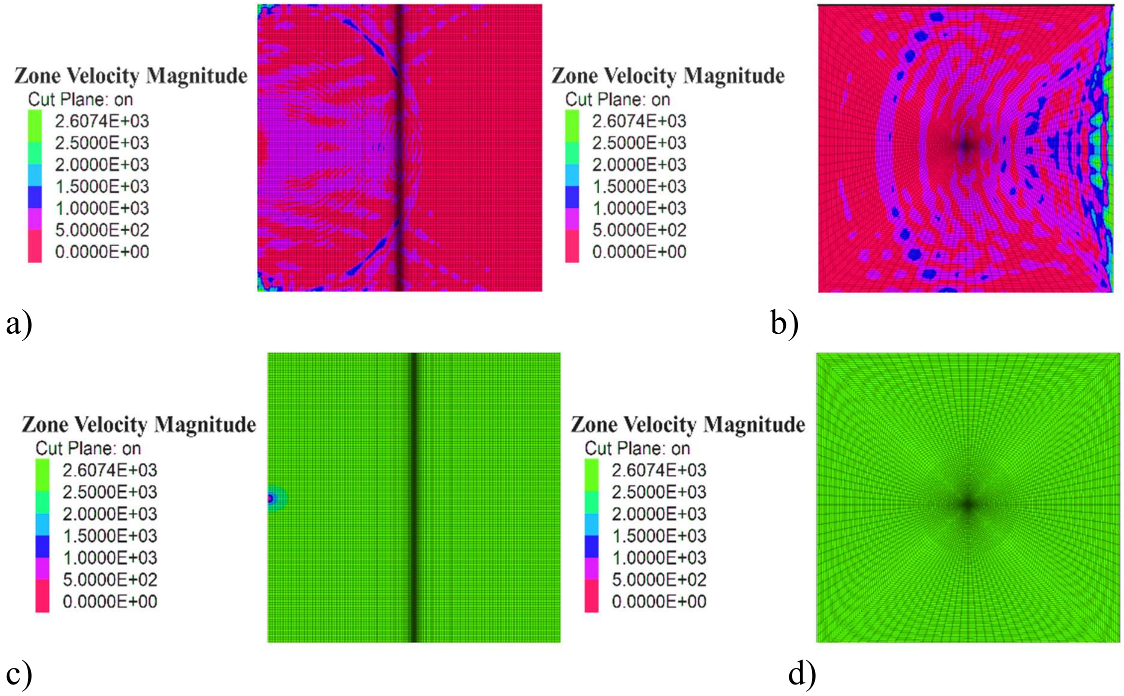

Figure 24. Wave velocity in solid concrete cube after 0.1 ms a) section view b) top view and 1 ms c) section view d) top view

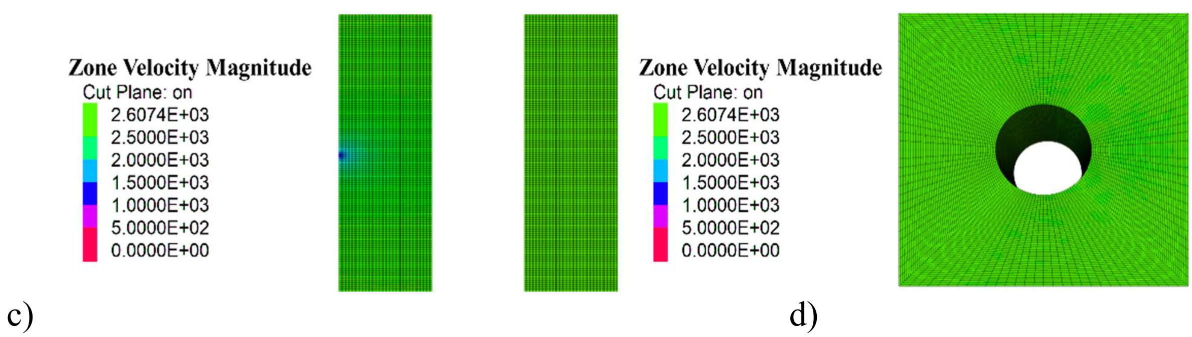

Figure 25. Wave velocity in concrete cube with empty hole after 0.1 ms a) section view b) top view and 1 ms c) section view d) top view

The change in material resulted in a variation in average velocity, showing a decline in the instance of concrete material. The average velocity recorded in concrete was 2700 m/s, while in granite, it measured around 3100 m/s.

In the third modeling scenario, sandstone material was utilized, and Table 11 presents the parameters used for the modeling process. The typical velocity for sandstone is around 1700 m/s [89].

Table 6.

Sandstone properties (Zhang & Guo, 2022).

Shear modulus	5 GPa
Bulk modulus	15 GPa
Density	2.6 g/cm3

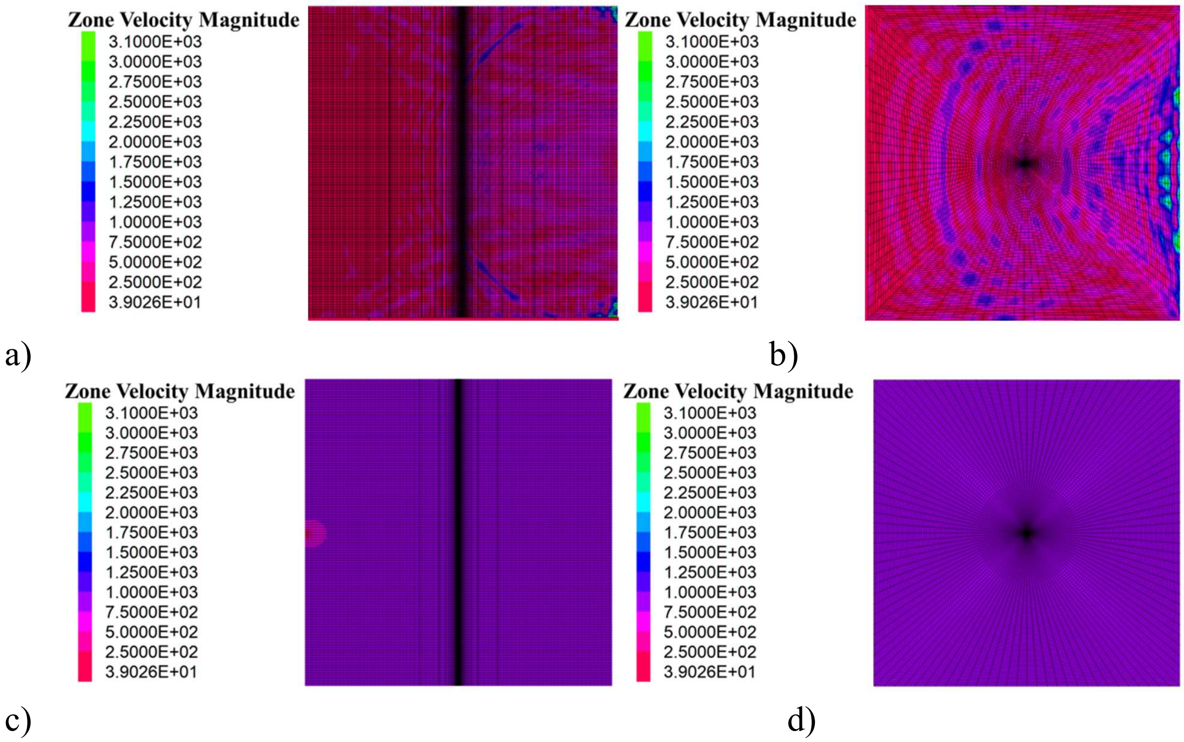

Figure 26. Wave velocity in solid sandstone cube after 0.1 ms a) section view b) top view and 1 ms c) section view d) top view

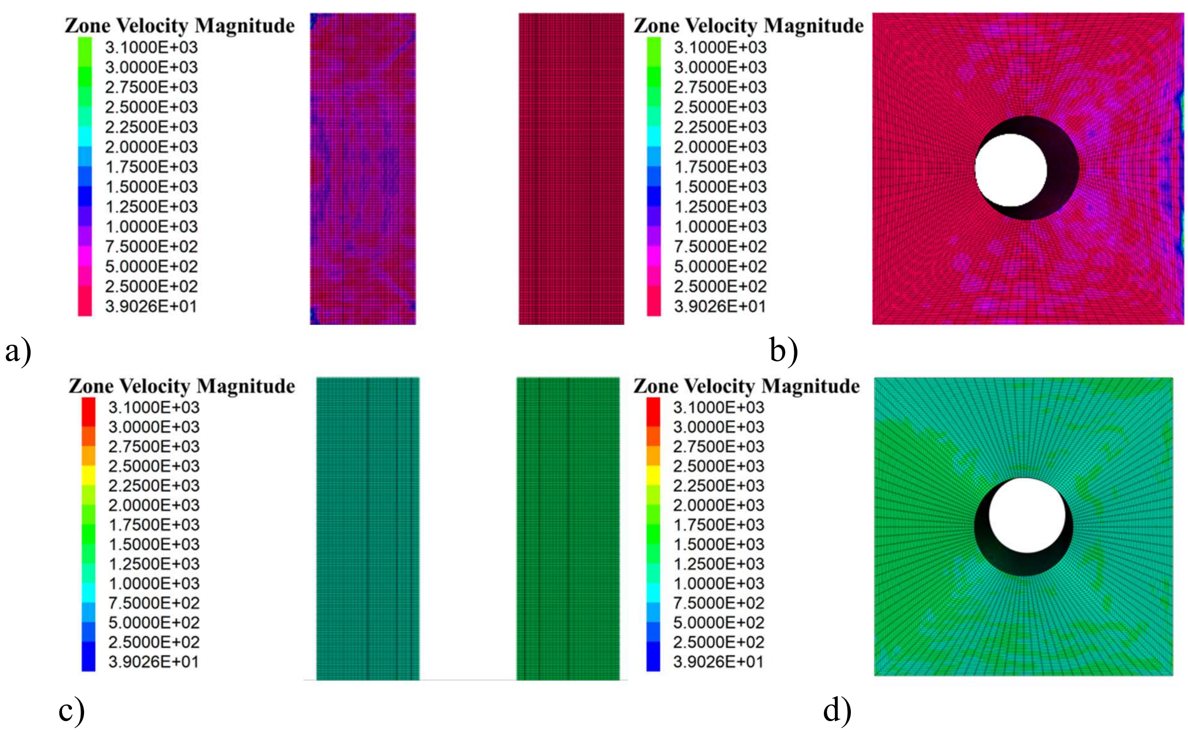

Figure 27. Wave velocity in sandstone cube with empty hole after 0.1 ms a) section view b) top view and 1 ms c) section view d) top view

5.6. Sensitivity analysis

A sensitivity analysis was performed utilizing the material properties of granite outlined in Table 7. The geometric configuration was modified to a cube with dimensions of 450 mm and a hole diameter of 150 mm. Models with varying frequencies for configurations both with and without holes are illustrated in Figures 42-43. The results indicate varying velocities at specific locations within the sample, influenced by the frequency of the emitted signal during wave propagation. As the frequency increases, there is a greater attenuation of wave energy originating from the source, as illustrated in Figures 42 to 43. A higher sampling rate in Acoustic Emission (AE) improves the precision of the signals. The presence of a hole leads to a heightened attenuation of wave energy in the vicinity of the hole, as demonstrated by the findings from the 450 mm cube featuring a 150 mm diameter hole in Figure 43.

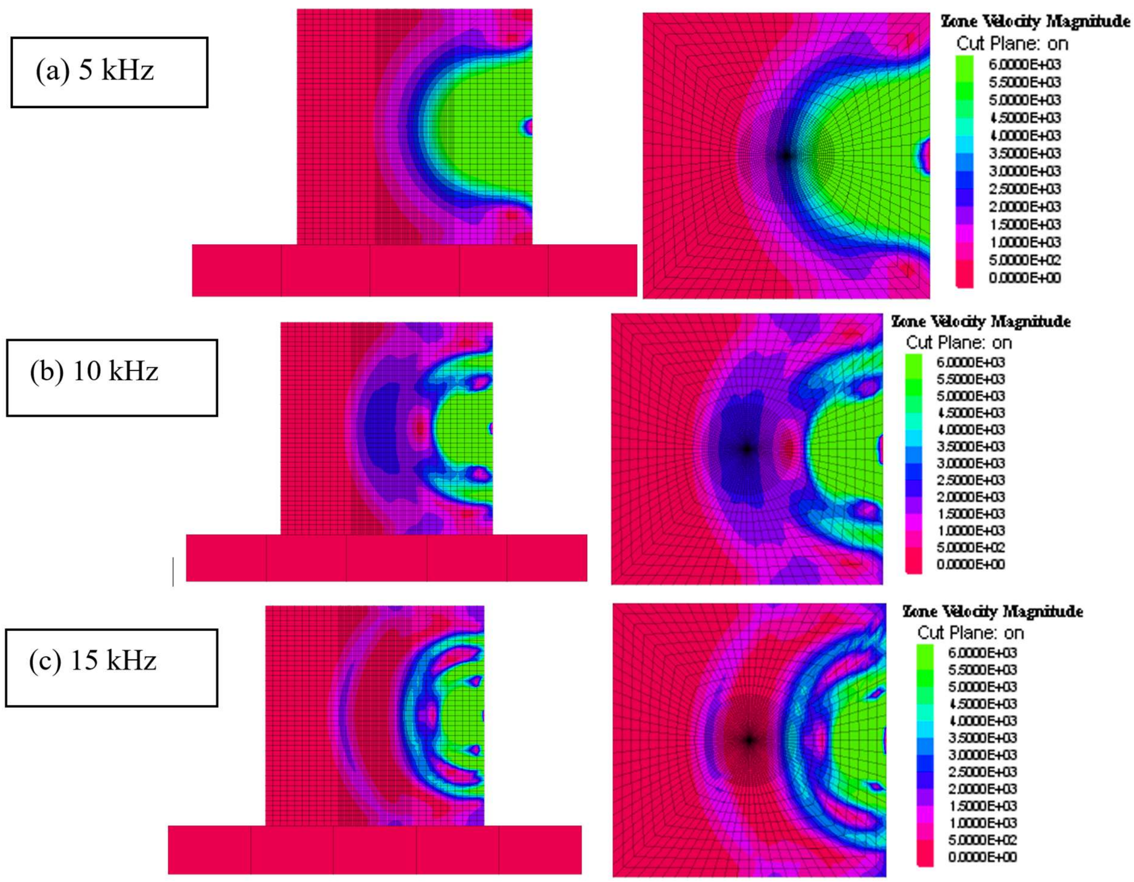

Figure 28. Velocity magnitude with different frequencies for solid 450 mm granite cube without hole. Section view at the middle of the sample and top view at 0.1 ms

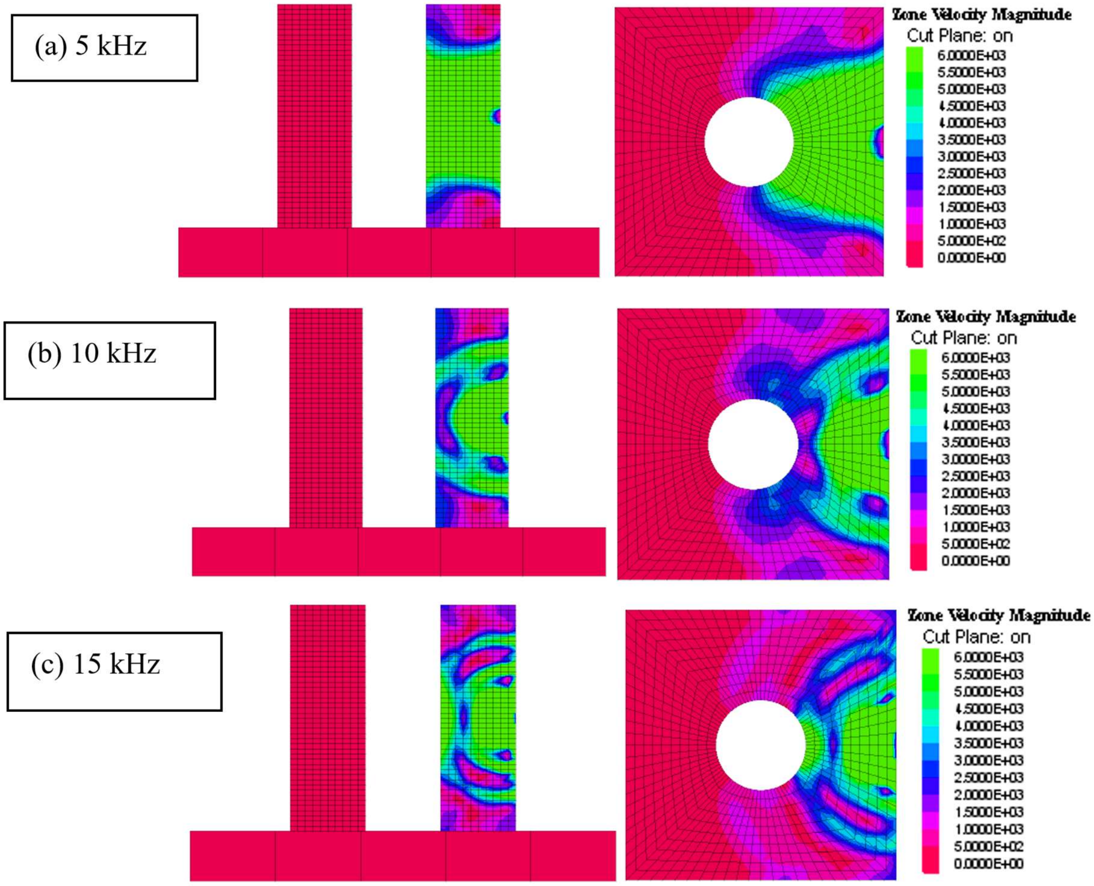

Figure 29. Velocity magnitude with different frequencies for 450 mm granite cube with hole diameter of 150 mm. Section view at the middle of the sample and top view at 0.1 ms

Other elements affecting the wave propagation pattern consist of material density and elastic parameters. Figure 44 demonstrates the variations in density, from loosely compacted materials like soil to more densely compacted substances. At a density of 1700 kg/m3, wave attenuation is notably higher when compared to densities of 220 kg/m3 or more. Therefore, it can be inferred that density influences the attenuation of seismic waves.

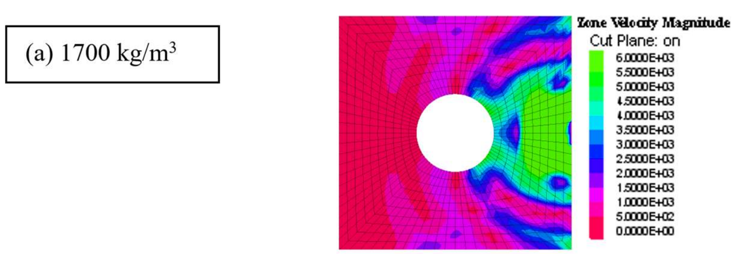

(a) 1700 kg/m^3

(c) 2700 kg/m^3

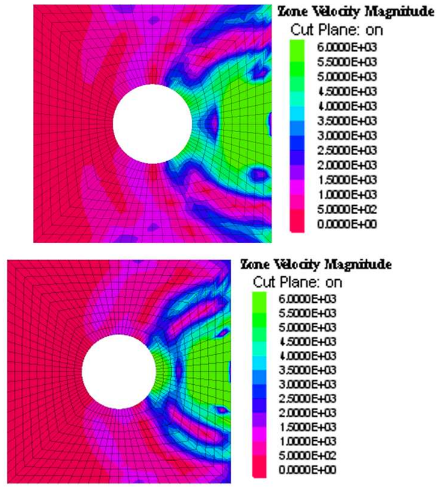

Figure 30. Velocity magnitude with different densities for 450 mm granite cube with hole diameter of 150 mm. Top view of a cut at the middle of the sample at 0.1 ms

Accurate characterization of the elastic parameters of the sample is essential. Figure 45 demonstrates the considerable influence of elastic parameters on wave propagation. The model includes the parameters specified in Table 7. In particular, Figure 45(a) was created using half of the parameters outlined in Table 7, whereas Figure 45(c) employed double those values.

(a) B/2

(b) B

(c) 2xB

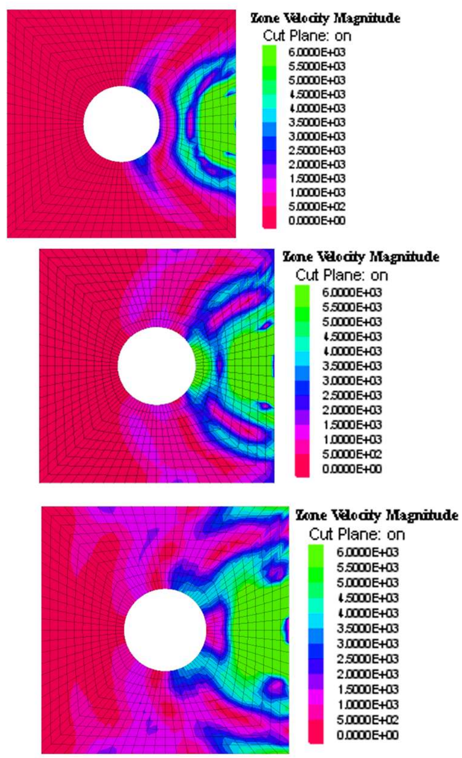

Figure 31. Velocity magnitude with different elastic parameters for 450 mm granite cube with hole diameter of 150 mm. Top view of a cut at the middle of the sample at 0.1 ms

The modeling results depicted in figure 45 indicate a strong positive correlation between velocity and elastic properties.

5.7. Summary

The investigation examined the influence of voids on seismic wave behavior through the use of different materials and configurations, demonstrating that the introduction of voids leads to heightened attenuation. Seismic wave velocity exhibited a clear response to the properties of materials, particularly in relation to variations in density and elastic parameters. The relationship between higher material density and enhanced elastic parameters leads to an increase in seismic wave velocity, providing valuable insights for predicting occurrences such as rockbursts and fluctuations in stress within mining contexts.
The robust correlation between experimental and modeled data confirms the dependability of the modeling methodology. Effective validation boosts trust in the precision of predictions, offering important insights for geomechanics and its applications in seismic hazard evaluation and mining safety.

6. MACHINE LEARNING

Machine learning (ML) represents a comprehensive domain within artificial intelligence, focused on enabling computers to address intricate problems autonomously, without the necessity for explicit programming for every individual task. In the realm of machine learning, the concept of "training" denotes the procedure of acquiring knowledge from historical data. The capacity to learn and adapt by leveraging previous experiences to improve or gain new skills distinguishes ML from traditional methods of programming computers to perform designated tasks. Conventional computer programming relies on precisely articulating a problem by utilizing the established physical laws of the system under examination. On the other hand, ML emphasizes the analysis of data to predict the behavior of intricate systems that are challenging to articulate using conventional approaches. The training in ML can be categorized as supervised, where the system acquires knowledge from a dataset containing correct answers, or unsupervised, which entails recognizing patterns without any prior knowledge of outcomes [36].

6.1. Data exploration

Data exploration entails the process of uncovering insights from data to efficiently pinpoint pertinent data components. To guarantee dependable exploration outcomes, the raw data must be subjected to meticulous selection and cleaning processes. This resembles the management of seismic data at mining locations, where typically there is an individual assigned to the task of refining the seismic data to eliminate blasting events and other related sources that do not reflect the ground's responses due to mining activities. A variety of dataset-handling techniques were employed, such as one-hot encoding, addressing missing values, managing recurring parameters, standardizing data types, and normalization, to ensure the integrity and quality of the data.

6.2 Initial data

The laboratory test results produced in Chapter 4 provided the foundational data for the machine learning application. The dataset included details such as the coordinates of the source and receiving sensors, arrival times of the wave at each sensor, quality parameters of the backfill influencing wave velocity, and the quality of fractured and unfractured cubes, indicated by RMR scores and associated wave velocities.

The dataset originally comprised 64 distinct parameters and a total of 1070 records, with 166 of those lacking any sensor data. Certain parameters included a combination of qualitative and quantitative data, whereas others exhibited missing values. There are repeated parameters, including the average velocity values from all sensors for each provided record. Additionally, the data format displayed inconsistencies, as numeric values were occasionally represented in floating-point format and at other times in text format.

The variables employed for training the models are detailed in Table 12. The sensor coordinates, distance to the source, and arrival time parameters vary based on the specific sensor or channel used. As a result, there exist seven datasets corresponding to each sensor, numbered from 2 to 8, with channel 1 serving as the source channel. Nonetheless, the other parameters maintain consistency throughout all datasets.

Table 12.
Variables used in training the models.

Variable	Unit	Description
Sample	[-]	The type of the experimental cube (concrete or granite)
Block size	[mm]	The type of the experimental cube (concrete or granite)
RMR	[-]	Rock mass rating, the fractured block quality
Hole	[-]	Boolean value that represents the presence of the hole in the cube
Hole Diameter	[mm]	The diameter of the cylindrical hole in the cube
Cement Content	[%]	Percentage of the cement mixture in the hole
Curing time	[ms]	The time elapsed after the hole was filled
Backfill strength	[MPa]	Backfill material quality
Source coordinates	[m, m, m]	Source coordinates in 3D space
Sensor coordinates	[m, m, m]	Sensor coordinates in 3D space
Arrival time	[ms]	The time at which the sensor captures the wave
Distance to source UCS	[m] [MPa]	The distance from the sensor to the source Uniaxial compressive strength of the sample

6.2.1. Dataset handling techniques

To tackle parameters that involve both qualitative and numeric values, a division was executed, categorizing qualitative and numeric data into separate parameters. Every qualitative value was converted into a binary parameter, using values of 0 or 1 to indicate the absence or presence of the corresponding attribute. For example, the initial parameter representing cement content, which included different types and percentages within a single column, was broken down into more specific components. Distinct Boolean parameters were established for various content types, while the cement content column maintained only the percentage values. Qualitative data was substituted with 0, indicating the lack of cement content.

To address the issue of missing values in the dataset, imputation was performed utilizing the mean value of the relevant field. In instances where specific records were devoid of information on backfill strength, the absent values were replaced with the mean value obtained from other known backfill strength figures corresponding to the same curing time. For instances where a value for a 7-day cured backfill was absent, it was replaced with the mean value derived from the available 7-day cured backfill samples. The dataset contains extensive mining-related information, and redundancy in parameters was tackled to improve the stability of machine learning training. Redundant parameters were systematically sorted or eliminated. A distinct parameter labeled 'qualitative data,' which summarized details on block description, hole presence, diameter, block size, and backfill type, was removed since these parameters were already included as independent fields. The data produced in the laboratory included both numerical and textual formats. To enable the effective use of machine learning algorithms and guarantee reliable outcomes, all data formats were standardized to a uniform float type. This process included the conversion of qualitative data, such as cement content, into binary formats and the transformation of textual data, such as '272.8,' into floating-point representations (e.g., 272.8).

The preprocessed dataset underwent normalization to improve the stability of model training. This procedure entailed adjusting and normalizing inputs to establish a distribution centered around 0, with a standard deviation of 1. The average and variance of the data were calculated in advance, and Equation 9 was utilized during runtime to carry out the normalization process.

$$(input - mean)/\sqrt{var} \tag{9}$$

Following the application of the previously discussed techniques for dataset cleaning, we obtained a total of 730 records encompassing 60 distinct parameters.

6.3. Machine learning methods

This study aims to identify the location of seismic events in underground mines, a complex endeavor complicated by the ever-changing ground conditions resulting from mining activities. We present a unique three-pronged strategy that incorporates machine learning techniques for predicting velocity and determining the source location of seismic events, utilizing the simplex method. Figure 46 illustrates the solution architecture.

Deep learning demonstrates significant potential in enhancing the accuracy of microseismic event source location, owing to its capacity to uncover hidden patterns and reduce the necessity for extensive feature engineering. A range of deep learning-based approaches employing convolutional neural networks (CNN) have been suggested for tasks such as microseismic and seismic wave denoising, waveform processing, event detection, classification, and location [46, 63, 91]. Nevertheless, the uncertainty inherent in the geological model complicates the process of detecting, classifying, and locating events, which can be accomplished through either time of arrival picking or raw waveforms. Notable solutions encompass Bayesian networks and CNNs, which provide location information derived from channel impulse response [14, 59, 91].

6.4. Seismic event source location prediction

6.4.1. Velocity prediction

The initial stage of predicting the location of seismic event sources focuses on estimating the velocity of seismic waves under different conditions through the application of machine learning algorithms. In particular, Linear Regression, Artificial Neural Networks (ANN), and Decision Trees (including ensemble methods like Random Forest and Gradient Boosted Trees) were utilized to determine the most effective model. In ANN models, the Rectified Linear Unit (ReLU) activation function is utilized, and twelve distinct configurations are examined, altering the number of hidden layers and neurons within each layer. The evaluation of these models is conducted through essential metrics such as Mean Absolute Error (MAE).

6.4.2. Initial seismic event source location

The second phase entails utilizing the simplex method, a recognized optimization algorithm, for the initial identification of the seismic event sources. The simplex method serves to enhance an objective function that reflects the travel time of seismic waves, which is influenced by the anticipated velocities and the possible locations of seismic events.

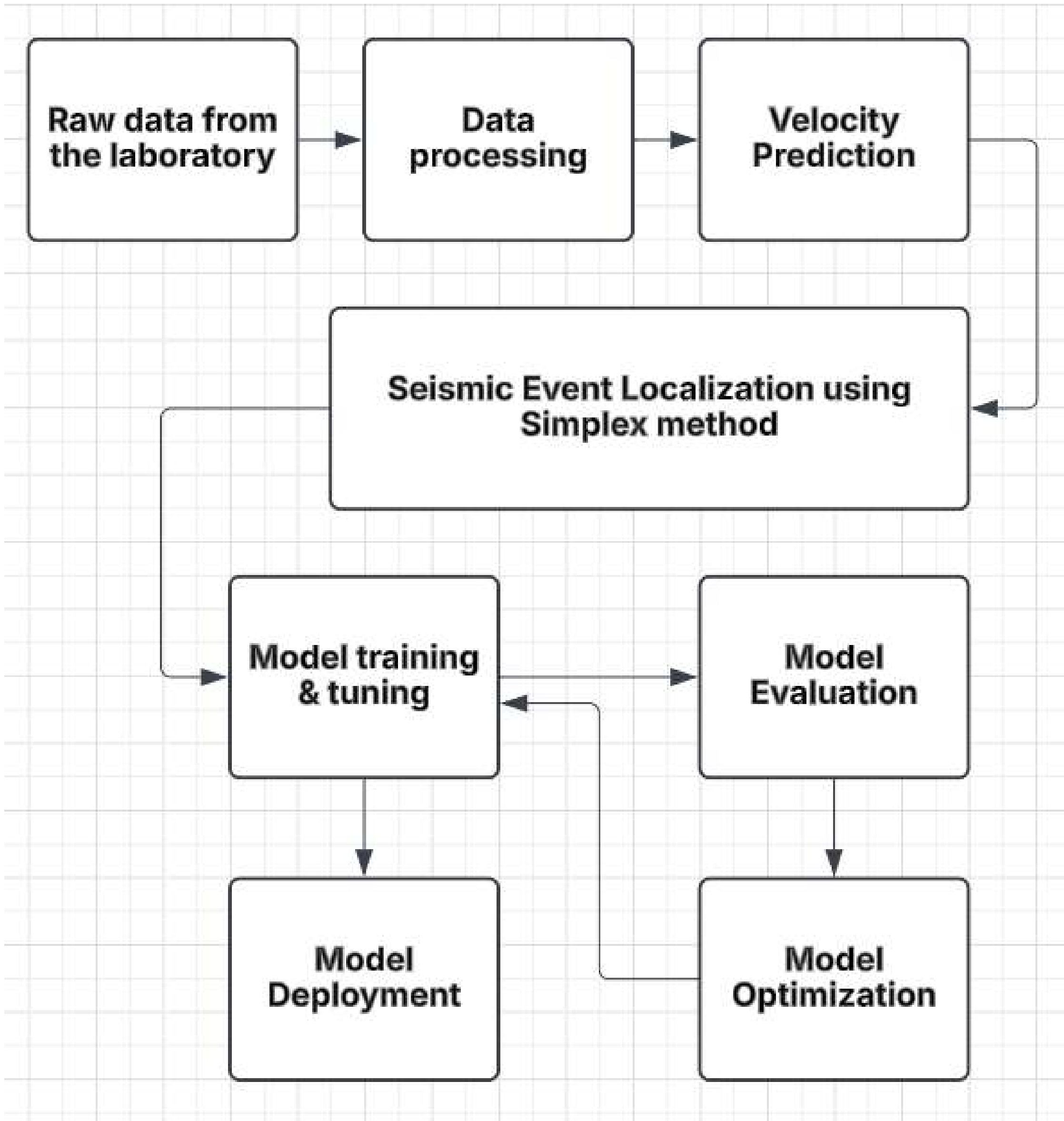

Figure 46. Solution Architecture for velocity real-time velocity prediction and improved seismic event source location determination

6.4.3. Refined seismic event source location

In response to the errors identified in the second phase, a third phase was implemented, utilizing machine learning techniques to enhance the accuracy of seismic event location. During this phase, the model is not exclusively focused on the differences between the locations obtained from the simplex method and the real seismic event locations. Both the original dataset and an augmented dataset are employed to train a machine learning model specifically designed for predicting the location of seismic events. This phase aims to enhance the precision and accuracy of predicting the source location of seismic events.

6.5. Machine learning implementation

6.5.1. Velocity prediction and simplex method

Linear Regression employs a simple model to predict the dependent variable by analyzing independent parameters, with the goal of reducing the discrepancy between predicted and actual values. The straightforward nature, clarity, and ability to expand make it appropriate for a range of uses. This study employs Linear Regression to predict velocity based on data collected from 22 concrete blocks and wave arrival times recorded by seven sensors positioned at specific locations on concrete and granite cubes.

Another alternative, Artificial Neural Networks (ANNs) (Figure 47), replicate the behavior of human neurons by transmitting signals with assigned weights, which constitute the foundation of neural networks. Deep learning, a sophisticated variant of machine learning, significantly depends on these networks, identifying complex relationships and patterns among features that might be missed by alternative approaches. This study involved testing a range of neural network architectures, each characterized by different configurations of hidden layers and neurons within those layers. The rectified linear unit (ReLU) function was utilized as the activation function, and a comprehensive evaluation of 12 distinct neural network configurations was conducted.

In our study, we utilized Decision Trees, particularly Random Forest and Gradient Boosted Decision Trees, because of their high prediction accuracy and efficiency. Decision trees mimic the processes involved in decision-making; however, they can sometimes overfit the data, leading to models that are not as generalizable. Random Forest tackles this issue by combining several decision trees, enhancing collective intelligence while sacrificing interpretability and computational efficiency. Gradient Boosted DT advances this method by building trees in a sequential manner, addressing the limitations of earlier models and reducing loss effectively.

After predicting velocity, the subsequent step is to ascertain the event source location through the application of the Simplex method. The Simplex method is extensively utilized in seismic monitoring systems, providing an efficient solution to non-linear equations. The simplex method is utilized in calculating the source location of seismic events by solving a system of equations that arise from velocity measurements and the time differences of seismic wave arrivals recorded by multiple sensors.

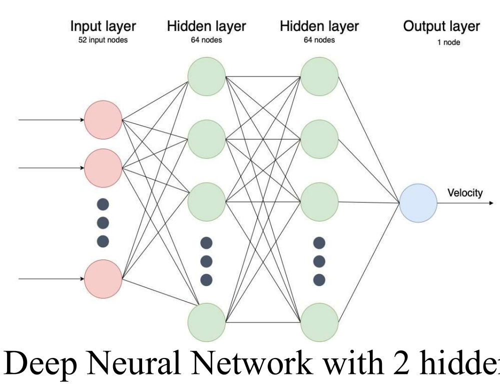

Figure 47. Deep Neural Network with 2 hidden layers

This method presents the issue as a set of nonlinear equations derived from the subsequent algebraic expression:

$$v.t + \sqrt{(X - a_1)^2 + (Y - b_1)^2 + (Z - c_1)^2} = \sqrt{(X - a_i)^2 + (Y - b_i)^2 + (Z - c_i)^2} \quad (10)$$

Where a1,b1,c1 epresent the coordinates of the nearest sensor, while ai,bi,ci denote the coordinates of the ith sensor. The variable t indicates the time difference between the sensors.v represents the velocity, while X,Y,Z denote the coordinates of the event source.

6.5.2. Direct seismic event source location

This study presents the architecture for implementing the Simplex method as follows:

- Input: The code requires the coordinates of seismic sensors, the anticipated velocities of seismic waves at the receiving sensor, and the time differences of seismic wave arrivals.
- Objective Function: The code establishes an objective function that quantifies the discrepancy between the predicted and observed time differences. This objective function quantifies the error or residual associated with estimating the location of seismic events.
- Initialization: An initial estimate for the coordinates of the seismic event is supplied to commence the optimization process. The initial estimate may be established at (0, 0, 0) or any other appropriate value.
- Iterative Optimization: The code employs the simplex method to progressively refine the seismic event coordinates and reduce the objective function. The process begins with an initial estimate and systematically refines the coordinates to minimize the discrepancy between predicted and observed time differences.
- Convergence: The optimization process persists until the objective function attains a minimum or a predetermined stopping criterion is satisfied. This guarantees that the solution aligns closely with the actual location of the seismic event.

The output provides the estimated coordinates of the seismic event, reflecting the calculated epicenter derived from the optimization using the simplex method.

The code utilizes the simplex method to calculate the location of seismic events, focusing on determining coordinates that reduce the difference between predicted and observed time differences at seismic sensors. The goal is to theoretically attain an accurate estimation of the epicenter of the seismic event. Nonetheless, real-world datasets frequently contain noise, making it impossible for some systems of equations to yield exact solutions. As a result, a method focusing on approximate solutions was adopted. In light of these endeavors, the approach continued to produce an error margin nearing 100%. Consequently, it was determined that the introduction of Direct Seismic Event location was essential.

To predict the location of the seismic event source, multioutput regression was necessary. Random Forest [33, 15], and Gradient Boosted Decision Trees [57] paired with skcikit-learn Multi Output Regressor was used to run regression.

Each model exhibited significant overfitting, primarily attributed to the limited diversity in the source location data, resulting in a prediction error of 0 cm for each coordinate. Recognizing the potential unreliability of such models in real-world scenarios, a strategic decision was made to introduce greater realism and robustness by randomly sampling a holdout dataset and incorporating noisy data.

Initially, the seismic dataset is imported into a Pandas DataFrame, encompassing information about seismic events slated for location. To fortify the robustness and accuracy of the model, the dataset is stratified into five equal segments. Within each segment, random sampling is executed, where approximately half of the data is randomly chosen as a holdout test set, while the remaining half is retained for model training and testing. The determination of the number of random samples involves dividing the segment length by 2 and rounding up to ensure a representative data subset. The resulting holdout segments are amalgamated and stored for the ultimate testing phase of trained models. Additionally, datasets are saved as CSV files, thereby ensuring reproducibility.

Iterating this process five times yields five distinct holdout and training datasets, each featuring diverse seismic events for training and testing. This iterative approach guarantees that the model undergoes training and evaluation on varied subsets of the dataset, contributing to a more robust assessment and instilling greater confidence in the model's performance. This methodology serves as a countermeasure against the pronounced overfitting tendencies observed in models.

6.5.2.1. Data Augmentation

To improve the training data and maximize the effectiveness of the direct seismic event localization model, two separate augmentation techniques—Gaussian augmentation and augmentation using Generative Adversarial Networks (GANs)—are utilized.

The initial method, Gaussian Augmentation, incorporates synthetic seismic events into the training dataset by applying Gaussian noise to the current data. This noise, originating from a Gaussian distribution, creates variations that mimic the natural variability found in seismic signals. Each row in the dataset is subjected to minor alterations to generate new data points. The incorporation of this augmented data into the training set strengthens the model's robustness against noise and enhances its capacity to generalize to previously unobserved seismic events with varied characteristics.

The second augmentation method utilizes GANs, which consist of a generator and a discriminator. The generator creates synthetic seismic events, whereas the discriminator is tasked with distinguishing between real and synthetic occurrences. By employing adversarial training, the generator enhances its capability to produce realistic synthetic seismic events that test the discriminator's skill in distinguishing them from genuine occurrences. The produced events are then integrated into the training set, offering a wider array of examples for the model to assimilate. These augmentation methods are applied in sequence to produce more resilient synthetic data for training purposes. The training dataset size is increased fourfold through data augmentation, reaching around 2500 rows.

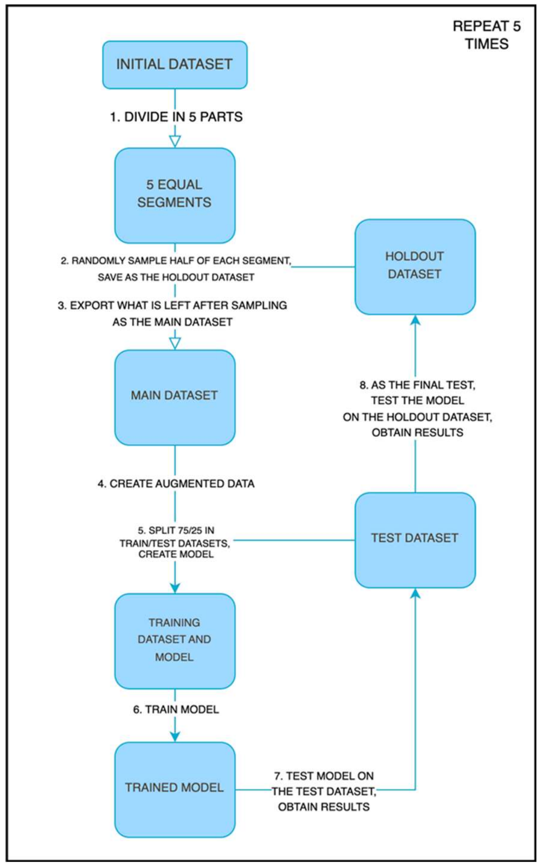

Figure 48. Data Preparation and Model training process

6.5.2.2. Building models and hyperparameter tuning

The training dataset, consisting of the remaining data after random sampling and newly generated data, is employed for model training. Following this, the training dataset is further divided into testing and training subsets, maintaining a ratio of 75/25.

XGBoost, Random Forest, and Gradient Boosted Decision Trees models are utilized to predict the source location, employing scikit-learn Multiple Output Regressor. In the first attempt, these models are executed with default parameters, leading to an average error of 7 cm on the training dataset, which is considered significant.

To minimize error, Grid Search cross-validation was employed to optimize the hyperparameters of the models. For each model, a variety of pertinent parameters are established, followed by the execution of Grid Search cross-validation. Upon completion of the tuning process, the Random Forest model demonstrates superior performance, achieving an average error of 4cm, representing a 75% reduction compared to the default parameter settings. Upon evaluation with the holdout dataset, the error measures approximately 1 cm, presenting a more realistic outcome compared to the previous prediction of 0 cm prior to data augmentation.

6.5.3. Experimental results

[47] developed innovative models for algorithms utilizing neural networks and implemented Decision Trees. Furthermore, rather than forecasting a singular velocity from aggregated sensor data, velocities were estimated separately for each individual sensor. This approach focused on improving the precision of forecasts relative to the earlier investigation, while also identifying sensors that may be unreliable.

$$MAE = \frac{\sum_{i=1}^{D} |x_i - y_i|}{n} \tag{11}$$

The Mean Absolute Error (MAE), as presented in Equation (13), was selected as the performance metric to evaluate the accuracy of our models. The optimal iteration of each algorithm was chosen, and their performances are documented in Table 13. The findings presented by [47] indicate that the peak accuracy achieved was 34.770 m/s. Nonetheless, the findings yielded significantly improved outcomes, with the peak accuracy achieving 7.146 m/s for sensor 2. After analyzing a comprehensive set of records, an average velocity of 1615.386 m/s was determined. This average acts as a pivotal value, offering a broad estimate of the velocities recorded in this scenario.

Table 13.
Model Performance

Model	Unit	#2	#3	#4	#5	#6	#7	#8
Linear Regression	[m/s]	618.25	591.09	624.4	478.43	628.08	674.04	673.1
DNN 6 128	[m/s]	22.02	20.46	29.46	42.99	26.95	27.88	21.39
GBDT	[m/s]	9.74	7.15	13.5	7.32	7.97	10.25	12.33

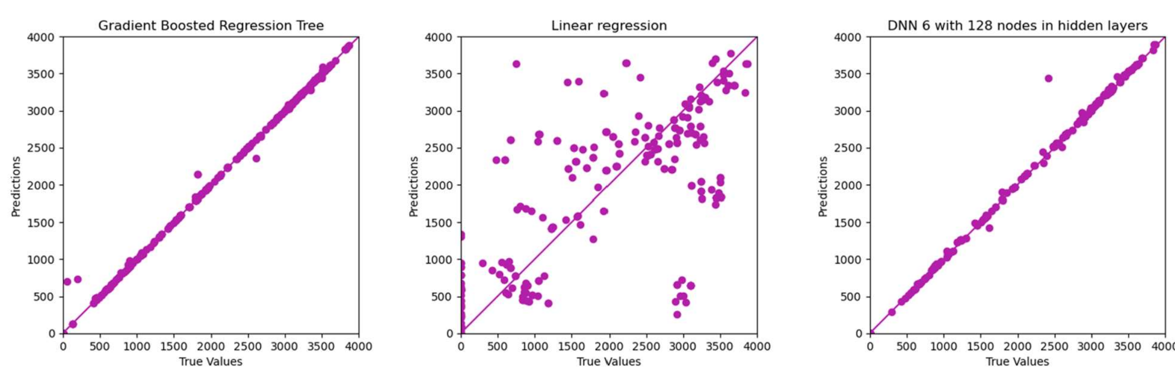

Figure 49. Training and validation losses of the models

Recognizing that one metric alone may not fully represent the entire distribution or account for potential outliers, it remains an important reference point for evaluating the model's inaccuracies. The observed discrepancies in the models, when considering the average velocity, are relatively modest, suggesting a favorable alignment with this central benchmark. As a result, these findings bolster the assertion that the models exhibit notable accuracy in predicting velocities.

Following this, the simplex method was employed for validation purposes. Nonetheless, even slight disturbances can make the system of equations impossible to solve because of fundamental inconsistencies. To address this challenge, a least squares approximation was utilized to ascertain the coordinates. Nonetheless, as shown in Table 12, the Mean Absolute Error (MAE) for each coordinate is considerable, frequently exceeding the actual values.

6.6. Summary

This chapter discusses the application of machine learning to forecast seismic wave velocities based on data produced under defined discrete block conditions. The data was utilized as input for an algorithm designed to locate seismic sources, with the objective of identifying their positions. Among the evaluated machine learning models, the Random Forest approach stood out as the most precise predictive model, demonstrating a remarkably low error margin of only 1mm. A range of machine learning models, encompassing deep learning methods, were utilized on the data produced under different block conditions to determine the most effective model. The objective of the model was to forecast a corresponding ground condition velocity based on a specified set of parameters. Among the tested ML models, the Gradient Boosted Decision Tree model stood out with an error rate of 7.15 m/s, compared to the average target velocity of 1615.39 m/s. The accuracy attained in forecasting velocity in a dynamic mining environment greatly improves the precision in pinpointing the source locations of seismic events. The study also resulted in the creation of an algorithm utilizing the simplex method. This algorithm, based on the principle of least squares approximation, determines the x, y, and z coordinates within a three-dimensional space.

7. CONCLUSIONS AND RECOMMENDATIONS

7.1. Conclusions

The objective of the thesis was to forecast the optimal velocity model in real-time for application in seismic source location computations within seismic monitoring systems. The aim was driven by the challenge of accurately forecasting the specific site of rockburst events. The literature review indicated that a major source of uncertainty impacting source location accuracy is found in the velocity model employed in the location algorithm. Creating a dependable velocity model in mining presents significant challenges, primarily due to the presence of various rock types and the ongoing fluctuations in rock mass conditions caused by the formation of voids and changes in stress. The intricacy of this situation requires an ever-evolving velocity model, which stands in stark contrast to the prevailing assumptions that rely on either a single homogeneous rock mass model or variable static constant velocity models based on layered rock formations in seismic monitoring systems for determining seismic source locations.

The study comprised three primary phases. The initial phase involved replicating the conditions of an underground mine within a regulated laboratory setting. The study utilized innovative discrete physical models as analogues to depict various stages in the mining process, encompassing aspects such as advancing mine maturity, enhanced mine extraction, and the fracturing induced by mining activities. AE tests were conducted on each discrete block under different conditions to evaluate how each condition influences seismic wave velocity. The findings indicated that in isotropic homogeneous blocks, the size effect had a minimal impact on seismic wave velocity. The impact of void and backfill on the travel time of AE signals is minimal in small 150 mm blocks. As block size and void diameter increase, along with the presence of backfill in the voids, the travel time of signals to sensors lengthens, resulting in a decrease in seismic wave velocity. The presence of a fracture resulted in signal attenuation that varied based on the sensors' positioning in relation to both the crack and the source. The RMR system developed by Bieniawski in 1973 was adjusted to accommodate laboratory samples.

The subsequent phase involved examining the responsiveness of seismic wave velocity to different variables within underground mining settings through dynamic modeling in FLAC3D. The modeling results indicated that voids affect seismic waves, demonstrating heightened attenuation with the introduction of voids. Furthermore, the velocity of seismic waves is influenced by the properties of materials, particularly variations in density and elastic characteristics. The relationship between higher material density and enhanced elastic parameters leads to an increase in seismic wave velocity, providing valuable insights for predicting occurrences such as rockbursts and fluctuations in stress within mining contexts.

The third step involved the application of machine learning to predict seismic wave velocity in real-time, tailored to different underground mine conditions for determining the locations of seismic event sources. Among the tested ML models, the Gradient

Boosted Decision Tree model stood out with an error rate of 7.15 m/s, compared to the average target velocity of 1615.39 m/s. The accuracy attained in forecasting velocity in a dynamic mining environment greatly improves the precision of pinpointing the source locations of seismic events. Furthermore, the investigation resulted in the creation of an algorithm utilizing the Simplex method, which is based on the principle of least squares approximation, to compute the x, y, and z coordinates in three-dimensional space.

The combination of numerical modeling, laboratory experiments, and advanced monitoring in a comprehensive approach improves understanding of seismic activities in mining. This thorough understanding, confirmed by a robust alignment between experimental and modeled data, not only enhances mining safety and efficiency but also highlights the importance of tackling seismic risks in intricate mining projects. The investigation establishes a comprehensive framework that takes into account stress, energy, and loading systems to predict seismic energy release in mining activities.

This thesis presents findings that offer important insights into the challenges and complexities involved in accurately determining the source locations of seismic events within dynamic underground mining environments. The creation of a continuously evolving velocity model through the use of discrete physical models as analogues marks a notable progress in overcoming the shortcomings of existing methodologies.

7.2.Recommendations

In light of the results obtained, it is highly advisable to pursue additional efforts to connect theoretical advancements with practical application. The emphasis should be on incorporating the developed velocity model into microseismic monitoring systems utilized in underground mines, facilitating real-time velocity prediction in conjunction with the simplex method. This implementation aims to assess the effectiveness of the continuously changing velocity model in practical applications and enhance the advancement of seismic monitoring techniques within the mining sector.

A crucial element that could enhance future studies, yet was neglected by the author because of time limitations, is the influence of confined stress on seismic wave velocity. The investigation was conducted based on the premise of a direct ray trajectory. Nonetheless, this aspect warrants further investigation to achieve a thorough comprehension of the wave travel path by utilizing ray tracing theory.

REFERENCES

1 Ammon, C. J., Velasco, A. A., Lay, T., & Wallace, T. C. Earth motions & seismometry // Foundations of Modern Global Seismology. 2021. URL: https://doi.org/10.1016/b978-0-12-815679-7.00011-2

2 Aster, R., Borchers, B., & Thurber, C. Parameter Estimation and Inverse Problems. 3rd ed. Elsevier, 2018.

3 Bandpey, A. K., Shahriar, K., Sharifzadeh, M., & Marefvand, P. Comparison of methods for calculating geometrical characteristics of discontinuities in a cavern of the Rudbar Lorestan power plant // Bulletin of Engineering Geology and the Environment. 2019. T. 78, № 2. C. 1073–1093. DOI: https://doi.org/10.1007/s10064-017-1145-x

4 Barton, N., Grimstad, E. Updating the Q-system for NMT // International Symposium on Sprayed Concrete. Январь 1993. C. 46–66.

5 Bieniawski, Z. T. Engineering Rock Mass Classifications. A Wiley-Interscience publication, 1989.

6 Blake, W., Leighton, F. W., & Duvall, W. Microseismic techniques for monitoring the behaviour of rock structures. U.S. Bureau of Mines, 1974.

7 C109/109M-16a, A. Standard test method for compressive strength of hydraulic cement mortars (Using 2-in. or cube specimens) // Annual Book of ASTM Standards. 2016. C. 1–10. DOI: https://doi.org/10.1520/C0109

8 Cai, M. Principles of rock support in burst-prone ground // Tunnelling and Underground Space Technology. 2013. T. 36. C. 46–56. DOI: https://doi.org/10.1016/j.tust.2013.02.003

9 Cai, M. Prediction and prevention of rockburst in metal mines - A case study of Sanshandao gold mine // Journal of Rock Mechanics and Geotechnical Engineering. 2016. T. 8, № 2. C. 204–211. DOI: https://doi.org/10.1016/j.jrmge.2015.11.002

10 Cai, W., Dou, L., Cao, A., Gong, S., & Li, Z. Application of seismic velocity tomography in underground coal mines: A case study of Yima mining area, Henan, China // Journal of Applied Geophysics. 2014. T. 109. C. 140–149. DOI: https://doi.org/10.1016/j.jappgeo.2014.07.021

11 Cai, W., Dou, L., Gong, S., Li, Z., & Yuan, S. Quantitative analysis of seismic velocity tomography in rock burst hazard assessment // Natural Hazards. 2015. T. 75, № 3. C. 2453–2465. DOI: https://doi.org/10.1007/s11069-014-1443-6

12 Cai, W., Dou, L.-M., Li, Z.-L., Liu, J., Gong, S.-Y., & He, J. Microseismic multidimensional information identification and spatio-temporal forecasting of rock burst: A case study of Yima Yuejin coal mine, Henan, China // Acta Geophysica Sinica. 2014. T. 57, № 8. C. 2687–2700. DOI: https://doi.org/10.6038/cjg20140827

13 CAMIRO. Canadian Rockbursts Handbook. Volume 6. Mining Research Directory, 1996.

14 Cao, R., Earp, S., De Ridder, S. A. L., Curtis, A., & Galetti, E. Near-real-time near-surface 3D seismic velocity and uncertainty models by wavefield gradiometry and

neural network inversion of ambient seismic noise // Geophysics. 2020. T. 85, № 1. C. KS13–KS27. DOI: https://doi.org/10.1190/geo2018-0562.1

15 Chen, T., & Guestrin, C. A Scalable Tree Boosting System // The 22nd ACM SIGKDD International Conference on Knowledge Discovery and Data Mining. 2016. C. 785–794.

16 Deere, D. U., & Deere, D. W. The Rock Quality Designation // 1988. C. 91–101.

17 Deere, D. U., & Miller, R. P. Engineering Classification and Index Properties for Intact Rock. University of Illinois Urbana-Champaign, 1966.

18 Di Benedetti, M., Loreto, G., Matta, F., & Nanni, A. Acoustic Emission Historic Index and Frequency Spectrum of Reinforced Concrete under Accelerated Corrosion // Journal of Materials in Civil Engineering. 2014. T. 26, № 9. DOI: https://doi.org/10.1061/(asce)mt.1943-5533.0000954

19 Dong, L., & Li, X. A microseismic/acoustic emission source location method using arrival times of PS waves for unknown velocity system // International Journal of Distributed Sensor Networks. 2013. DOI: https://doi.org/10.1155/2013/307489

20 Dong, L., Sun, D., Li, X., & Du, K. Theoretical and Experimental Studies of Localization Methodology for AE and Microseismic Sources Without Pre-Measured Wave Velocity in Mines // IEEE Access. 2017. T. 5. C. 16818–16828. DOI: https://doi.org/10.1109/ACCESS.2017.2743115

21 Fall, M., Célestin, J. C., Pokharel, M., & Touré, M. A contribution to understanding the effects of curing temperature on the mechanical properties of mine cemented tailings backfill // Engineering Geology. 2010. T. 114, № 3–4. C. 397–413. DOI: https://doi.org/10.1016/j.enggeo.2010.05.016

22 Feng, X. T., Yu, Y., Feng, G. L., Xiao, Y. X., Chen, B.-R., & Jiang, Q. Fractal behaviour of the microseismic energy associated with immediate rockbursts in deep, hard rock tunnels // Tunnelling and Underground Space Technology. 2016. T. 51. C. 98–107. DOI: https://doi.org/10.1016/j.tust.2015.10.002

23 Feng, X., Xiao, Y., Feng, G., Yao, Z., Chen, B., Yang, C., & Su, G. Study on the development process of rockbursts // Yanshilixue Yu Gongcheng Xuebao/Chinese Journal of Rock Mechanics and Engineering. 2019. T. 38, № 4. C. 649–673. DOI: https://doi.org/10.13722/j.cnki.jrme.2019.0103

24 Gao, F., Kaiser, P. K., Stead, D., Eberhardt, E., & Elmo, D. Numerical simulation of strainbursts using a novel initiation method // Computers and Geotechnics. 2019. T. 106 (Июль 2018). C. 117–127. DOI: https://doi.org/10.1016/j.compgeo.2018.10.018

25 Grenon, M., & Hadjigeorgiou, J. Evaluating discontinuity network characterization tools through mining case studies // Soil Rock America. 2003. T. 1. C. 137–142.

26 Grosse, C. U., Ohtsu Masayasu, Aggelis, D. G., & Shiotani, T. Acoustic Emission Testing Basics for Research – Applications in Engineering. 2nd ed. Springer, 2022. URL: http://www.springer.com/series/15088

27 Hauquin, T., Gunzburger, Y., & Deck, O. Predicting pillar burst by an explicit modelling of kinetic energy // International Journal of Rock Mechanics and Mining Sciences. 2018. T. 107 (Ноябрь 2017). C. 159–171. DOI: https://doi.org/10.1016/j.ijrmms.2018.05.004

28 Hedley, D. Rockburst handbook for Ontario hardrock mines. Volume 92. Canmet, 1992.

29 Huo, X., Wu, Q., Tang, H., Meng, Z., Wang, D., Liu, Y., & Li, S. A new approach for estimating rock discontinuity trace intensity based on rectangular sampling windows // Advances in Civil Engineering. 2020. DOI: https://doi.org/10.1155/2020/8834861

30 ITASCA. Itasca's FLAC3D Documentation, 2022a.

31 ITASCA. Itasca's FLAC3D Documentation, 2022b.

32 Jiang, Q., Feng, X. T., Xiang, T. B., & Su, G. S. Rockburst characteristics and numerical simulation based on a new energy index: A case study of a tunnel at 2,500 m depth // Bulletin of Engineering Geology and the Environment. 2010. T. 69, № 3. C. 381–388. DOI: https://doi.org/10.1007/s10064-010-0275-1

33 Jin, Z., Shang, J., Zhu, Q., Ling, C., Xie, W., & Qiang, B. RFRSF: Employee Turnover Prediction Based on Random Forests and Survival Analysis // Lecture Notes in Computer Science (Including Subseries Lecture Notes in Artificial Intelligence and Lecture Notes in Bioinformatics). 2020. T. 12343 LNCS. C. 503–515. DOI: https://doi.org/10.1007/978-3-030-62008-0_35

34 Jing, L. A review of techniques, advances and outstanding issues in numerical modelling for rock mechanics and rock engineering // International Journal of Rock Mechanics and Mining Sciences. 2003. T. 40, № 3. C. 283–353. DOI: https://doi.org/10.1016/S1365-1609(03)00013-3

35 Jing, L., & Hudson, J. A. Numerical methods in rock mechanics // International Journal of Rock Mechanics and Mining Sciences. 2002. T. 39, № 4. C. 409–427. DOI: https://doi.org/10.1016/S1365-1609(02)00065-5

36 Jooshaki, M., Nad, A., & Michaux, S. A systematic review on the application of machine learning in exploiting mineralogical data in mining and mineral industry // Minerals. 2021. T. 11, № 8. C. 816. DOI: https://doi.org/10.3390/min11080816

37 Kaiser, P. K., & Cai, M. Design of rock support system under rockburst condition // Journal of Rock Mechanics and Geotechnical Engineering. 2012. T. 4, № 3. C. 215–227. DOI: https://doi.org/10.3724/sp.j.1235.2012.00215

38 Kaiser, P. K., McCreath, D. R., & Tannant, D. D. Canadian Rockburst Support Handbook. January, 314. 1996.

39 Kennett, B. L. N., Marson-Pidgeon, K., & Sambridge, M. S. Geophysical Research Letters. 2000.

40 KSGidro. No Title. 2022. URL: https://ksgidro.ru/katalog/materialyi/smesi-dlya-razrusheniya-betona/nevzryivchataya-smes-nrs-1.html

41 Kuhlemeyer, R. L., & Lysmer, J. Finite Element Method Accuracy for Wave Propagation Problems // Journal of the Soil Dynamics Division. 1973. T. 99. C. 421–427.

42 Kulatilake, P. H. S. W., & Wu, T. H. Sampling bias on orientation of discontinuities // Rock Mechanics and Rock Engineering. 1984. T. 17. C. 243–253. DOI: https://doi.org/10.1007/BF01032337

43 Lemy, F., & Hadjigeorgiou, J. A digital face mapping case study in an underground hard rock mine // Canadian Geotechnical Journal. 2004. T. 41, № 6. C. 1011–1025. DOI: https://doi.org/10.1139/t04-046

44 Li, Z., He, S., Song, D., He, X., Dou, L., Chen, J., Liu, X., & Feng, P. Microseismic temporal-spatial precursory characteristics and early warning method of rockburst in steeply inclined and extremely thick coal seam // Energies. 2021. T. 14, № 4. DOI: https://doi.org/10.3390/en14041186

45 Liang, Z., Xue, R., Xu, N., & Li, W. Characterizing rockbursts and analysis on frequency-spectrum evolutionary law of rockburst precursor based on microseismic monitoring // Tunnelling and Underground Space Technology. 2020. T. 105 (Ноябрь 2019). C. 103564. DOI: https://doi.org/10.1016/j.tust.2020.103564

46 Ma, Y., Cao, S., Rector, J. W., & Zhang, Z. Automatic first arrival picking for borehole seismic data using a pixel-level network // SEG Technical Program Expanded Abstracts. 2019. C. 2463–2467. DOI: https://doi.org/10.1190/segam2019-3216775.1

47 Maksut, Z., Meiramov, R., Yazici, A., & Suorineni, F. A Machine Learning-based Microseismic Event Location and Wave Velocity Prediction // 56th U.S. Rock Mechanics/Geomechanics Symposium. 2022. DOI: https://doi.org/10.56952/arma-2022-0166

48 Malek, F., Espley, S., Yao, M., Trifu, C., & Suorineni, F. Management of High Stress and Seismicity at Vale Inco Creighton Mine // The 42nd U.S. Rock Mechanics Symposium (USRMS), 29 June-2 July, 2008. C. 8.

49 Manouchehrian, A., & Cai, M. Analysis of rockburst in tunnels subjected to static and dynamic loads // Journal of Rock Mechanics and Geotechnical Engineering. 2017. T. 9, № 6. C. 1031–1040. DOI: https://doi.org/10.1016/j.jrmge.2017.07.001

50 Manouchehrian, A., & Cai, M. Numerical modeling of rockburst near fault zones in deep tunnels // Tunnelling and Underground Space Technology. 2018. T. 80 (Июнь). C. 164–180. DOI: https://doi.org/10.1016/j.tust.2018.06.015

51 Medinac, F. Advances in Pit Wall Mapping and Slope Assessment using Unmanned Aerial Vehicle Technology // University of Toronto. 2019.

52 Milne, D., Hadjigeorgiou, J., & Pakalnis, R. Rock mass characterization for underground hard rock mines // Tunnelling and Underground Space Technology. 1998. T. 13, № 4. C. 383–391. DOI: https://doi.org/10.1016/S0886-7798(98)00081-9

53 Mohsin, A., Alsmadi, Y., Arshad Uppal, A., & Gulfam, S. M. A modified simplex based direct search optimization algorithm for adaptive transversal FIR filters

// Science Progress. 2021. T. 104, № 2. C. 1–19. DOI: https://doi.org/10.1177/00368504211025409

54 Mondal, D., & Roy, P. N. S. Fractal and seismic b-value study during dynamic roof displacements (roof fall and surface blasting) for enhancing safety in the longwall coal mines // Engineering Geology. 2019. T. 253 (Март). C. 184–204. DOI: https://doi.org/10.1016/j.enggeo.2019.03.018

55 Morkel, I., Wesseloo, J., & Potvin, Y. Seismic event location uncertainty in mining with reference to caving // 2015. C. 445–460. DOI: https://doi.org/10.36487/acg_repo/2205_30

56 Munfakh, G., Wylie, D., & CW, M. Training Course in Geotechnical // Issue 13235. 1998.

57 Natekin, A., & Knoll, A. Gradient boosting machines, a tutorial // Frontiers in Neurorobotics. 2013. T. 7 (DEC). DOI: https://doi.org/10.3389/fnbot.2013.00021

58 Nelder, J. A., & Mead, R. A Simplex Method for Function Minimization // The Computer Journal. 1965. T. 7, № 4. C. 308–313. DOI: https://doi.org/10.1093/comjnl/7.4.308

59 Niitsoo, A., Edelhäußer, T., & Mutschler, C. Convolutional Neural Networks for Position Estimation in TDoA-Based Locating Systems // IPIN 2018 - 9th International Conference on Indoor Positioning and Indoor Navigation. 2018. C. 24–27. DOI: https://doi.org/10.1109/IPIN.2018.8533766

60 Palei, S. K., & Das, S. K. Logistic regression model for prediction of roof fall risks in bord and pillar workings in coal mines: An approach // Safety Science. 2009. T. 47, № 1. C. 88–96. DOI: https://doi.org/10.1016/j.ssci.2008.01.002

61 Palmstrom, A. The Volumetric Joint Count—A Useful and Simple Measure of the Degree of Rock Jointing // Proceedings of 4th International Association of Engineering Geology. 1982. C. 221–228.

62 Palmstrom, A. Measurements of and correlations between block size and rock quality designation (RQD) // Tunnelling and Underground Space Technology. 2005. T. 20, № 4. C. 362–377. DOI: https://doi.org/10.1016/j.tust.2005.01.005

63 Pham, N., Merzlikin, D., Fomel, S., & Chen, Y. Passive Seismic Signal Denoising Using Convolutional Neural Network // SEG Technical Program Expanded Abstracts. 2020.

64 Qian, Q. H. Definition, mechanism, classification and quantitative forecast model for rockburst and pressure bump // Yantu Lixue/Rock and Soil Mechanics. 2014. T. 35, № 1. C. 1–6.

65 Qin, Z., Li, T., Li, Q., Chen, G., & Cao, B. Combined Early Warning Method for Rock Burst and Its Engineering Application // Advances in Civil Engineering. 2019. C. 1–8. DOI: https://doi.org/10.1155/2019/1269537

66 Ranjith, P. G., Zhao, J., Ju, M., De Silva, R. V. S., Rathnaweera, T. D., & Bandara, A. K. M. S. Opportunities and Challenges in Deep Mining: A Brief Review //

Engineering. 2017. T. 3, № 4. C. 546–551. DOI: https://doi.org/10.1016/J.ENG.2017.04.024

67 Salamon, A., & Kazár, G. Epidemiology of hand injuries in Vas County based on a survey // Magyar Traumatológia, Ortopédia, Kézsebészet, Plasztikai Sebészet. 1993. T. 36, № 3. C. 297–300.

68 Shi, X., Jing, H., Yin, Q., Zhao, Z., Han, G., & Gao, Y. Investigation on physical and mechanical properties of bedded sandstone after high-temperature exposure // Bulletin of Engineering Geology and the Environment. 2020. T. 79, № 5. C. 2591–2606. DOI: https://doi.org/10.1007/s10064-020-01729-7

69 Sirois, F., & Grilli, F. Potential and limits of numerical modelling for supporting the development of HTS devices // Superconductor Science and Technology. 2015. T. 28, № 4. C. 43002. DOI: https://doi.org/10.1088/0953-2048/28/4/043002

70 Spall, J. C. Introduction to Stochastic Search and Optimization: Estimation, Simulation, and Control. DOI: https://doi.org/10.1002/0471722138

71 Song, Y., Zhao, Y., Zhang, Y., Deng, W., & Lu, C. Research on microseismic localization algorithm with global search and local optimization // Heliyon. 2023. T. 9, № 9. e19251. DOI: https://doi.org/10.1016/j.heliyon.2023.e19251

72 Trifu, C. I., & Shumila, V. Geometrical and inhomogeneous raypath effects on the characterization of open-pit seismicity // 44th US Rock Mechanics Symposium - 5th US/Canada Rock Mechanics Symposium. 2010.

73 Trifu, C. I., & Suorineni, F. T. Use of Microseismic Monitoring for Rockburst Management At Vale Inco Mines // Controlling Seismic Hazard And Sustainable Development Of Deep Mines: 7th International Symposium on Rockburst And Seismicity In Mines. 2009. C. 1105–1114.

74 Umili, G., Ferrero, A., & Einstein, H. H. A new method for automatic discontinuity traces sampling on rock mass 3D model // Computers and Geosciences. 2013. T. 51. C. 182–192. DOI: https://doi.org/10.1016/j.cageo.2012.07.026

75 Wang, G., Gong, S., Dou, L., Wang, H., Cai, W., & Cao, A. (2018). Rockburst characteristics in syncline regions and microseismic precursors based on energy density clouds. Tunnelling and Underground Space Technology, 81(April), 83–93. https://doi.org/10.1016/j.tust.2018.06.026

76 Wang, J., Apel, D. B., Pu, Y., Hall, R., Wei, C., & Sepehri, M. (2021). Numerical modeling for rockbursts: A state-of-the-art review. Journal of Rock Mechanics and Geotechnical Engineering, 13(2), 457–478. https://doi.org/10.1016/j.jrmge.2020.09.011

77 Wu, Q., Kulatilake, P. H. S. W., & Tang, H. ming. (2011). Comparison of rock discontinuity mean trace length and density estimation methods using discontinuity data from an outcrop in Wenchuan area, China. Computers and Geotechnics, 38(2), 258–268. https://doi.org/10.1016/j.compgeo.2010.12.003

78 Wylie, D. C. (1999). Foundations on Rock: Engineering Practice (second). E&FN Spon.

79 Xie, H., Gao, F., & Ju, Y. (2015). Research and development of rock mechanics in deep ground engineering. Yanshilixue Yu Gongcheng Xuebao/Chinese Journal of Rock Mechanics and Engineering, 34(11), 2161–2178. https://doi.org/10.13722/j.cnki.jrme.2015.1369

80 Xu, S., Liang, R., Suorineni, F. T., & Li, Y. (2021). Evaluation of the use of sublevel open stoping in the mining of moderately dipping medium-thick orebodies. International Journal of Mining Science and Technology, 31(2), 333–346. https://doi.org/10.1016/j.ijmst.2020.12.002

81 Xu, S., Hou, P., Li, R., & Suorineni, F. T. (2022). An improved outer pipe method for expansive pressure measurement of static cracking agents. International Journal of Mining Science and Technology, 32(1), 27–39. https://doi.org/10.1016/j.ijmst.2021.11.011

82 Xue, R., Liang, Z., Xu, N., & Dong, L. (2020). Rockburst prediction and stability analysis of the access tunnel in the main powerhouse of a hydropower station based on microseismic monitoring. International Journal of Rock Mechanics and Mining Sciences, 126(March 2019), 104174. https://doi.org/10.1016/j.ijrmms.2019.104174

83 Xue, Y., Song, D., Chen, J., Li, Z., He, X., Wang, H., Zhou, C., & Sobolev, A. (2023). Integrated rockburst hazard estimation methodology based on spatially smoothed seismicity model and Mann-Kendall trend test. International Journal of Rock Mechanics and Mining Sciences, 163 (май 2022), 105329. https://doi.org/10.1016/j.ijrmms.2023.105329

84 Yu, Q., Zhao, D., Xia, Y., Jin, S., Zheng, J., Meng, Q., Mu, C., & Zhao, J. (2022). Multivariate Early Warning Method for Rockburst Monitoring Based on Microseismic Activity Characteristics. Frontiers in Earth Science, 10 (январь), 1–15. https://doi.org/10.3389/feart.2022.837333

85 Yuyama, S., Yokoyama, K., Niitani, K., Ohtsu, M., & Uomoto, T. (2007). Detection and evaluation of failures in high-strength tendon of prestressed concrete bridges by acoustic emission. Construction and Building Materials, 21 (3), 491–500. https://doi.org/10.1016/j.conbuildmat.2006.04.010

86 Zhang, C., Feng, X. T., Zhou, H., Qiu, S., & Wu, W. (2012). Case histories of four extremely intense rockbursts in deep tunnels. Rock Mechanics and Rock Engineering, 45 (3), 275–288. https://doi.org/10.1007/s00603-011-0218-6

87 Zhang, C., Jin, G., Liu, C., Li, S., Xue, J., Cheng, R., Wang, X., & Zeng, X. (2021). Prediction of rockbursts in a typical island working face of a coal mine through microseismic monitoring technology. Tunnelling and Underground Space Technology, 113 (февраль), 103972. https://doi.org/10.1016/j.tust.2021.103972

88 Zhang, L., & Einstein, H. H. (2000). Estimating the intensity of rock discontinuities. International Journal of Rock Mechanics and Mining Sciences, 37 (5), 819–837. https://doi.org/10.1016/s1365-1609(00)00022-8

89 Zhang, H., & Guo, W. (2022). Acoustic Emission Waveform Characteristics of Red Sandstone Failure under Uniaxial Compression after Thermal Damage. Sustainability (Switzerland), 14 (20). https://doi.org/10.3390/su142013285

90 Zhou, J., Li, X., & Mitri, H. S. (2018). Evaluation method of rockburst: State-of-the-art literature review. Tunnelling and Underground Space Technology, 81 (октябрь 2017), 632–659. https://doi.org/10.1016/j.tust.2018.08.029

91 Zhu, W., & Beroza, G. C. (2019). PhaseNet: A deep-neural-network-based seismic arrival-time picking method. Geophysical Journal International, 216 (1), 261–273. https://doi.org/10.1093/gji/ggy423

92 Zhu, W., Mousavi, S. M., & Beroza, G. C. (2019). Seismic Signal Denoising and Decomposition Using Deep Neural Networks. IEEE Transactions on Geoscience and Remote Sensing, 57 (11), 9476–9488. https://doi.org/10.1109/TGRS.2019.2926772